The Far-Field Angular Distribution of High-Order Harmonics Produced in Light Scattering from a Thin Low-Density Gas Target

by

Justin Bruce Peatross

Submitted in Partial Fulfillment
of the
Requirements for the Degree
Doctor of Philosophy

Supervised by
David D. Meyerhofer
and
Joseph H. Eberly

Department of Physics and Astronomy
College of Arts and Science

University of Rochester
Rochester, New York
1993

CURRICULUM VITAE

The author was born in Portland, Oregon on April 26, 1965. He attended Brigham Young University from 1983 to 1988, and graduated Cum Laude with a Bachelor of Science degree in Physics. He came to the University of Rochester in the fall of 1988 and began graduate studies in the Department of Physics and Astronomy. His research work was performed under the direction of Professor David D. Meyerhofer at the Laboratory for Laser Energetics.

PUBLICATIONS

"The Angular Distribution of High-Order Harmonics Emitted from Rare Gases at Low Density," J. Peatross and D. D. Meyerhofer, Phys. Rev. Lett., submitted, (1993).

"Novel Gas Target For Use in Laser Harmonic Generation," J. Peatross and D. D. Meyerhofer, Rev. Sci. Instrum., to be published, (1993).

"Sequential Ionization in ^{3}He with a 1.5ps, 1μm Laser Pulse," J. Peatross, B. Buerke, and D. D. Meyerhofer, Phys. Rev. A **47**, 1517-1519 (1993).

"Laser Temporal and Spatial Effects on Ionization Suppression," J. Peatross, M. V. Fedorov, and D. D. Meyerhofer, J. Opt. Soc. Am. B. **9**, 1234-1239 (1992).

"Suppression of the Pedestal in a Chirped-Pulse-Amplification Laser," Y.-H. Chuang, D. D. Meyerhofer, S. Augst, H. Chen, J. Peatross, and S. Uchida, J. Opt. Soc. Am. B **8**, 1226–1235 (1991).

Conference Publications:

"Angular Distribution of High order Harmonics From Low-Density Targets," D. D. Meyerhofer and J. Peatross, to be published in proceedings of the 6th International Conference on Multiphoton Processes, (Quebec, Canada, June 1993).

“Measurement of the Angular Distribution of High-Order Harmonics Emitted from Rare Gases,” J. Peatross and D. D. Meyerhofer, to be published in proceedings of Short Wavelength V: Physics with Intense Laser Pulses, (OSA, San Diego, CA, 29–31 March 1993).

"Angular Distribution of High-Order Harmonics," D. D. Meyerhofer and J. Peatross, to be published in the proceedings of the 3rd Conference on Super Intense Laser-Atom Physics, (NATO, Han-sur-Lesse, Belgium, January 1993).

"Spatial Distribution of High-Order Harmonics Generated in the Tunneling Regime," Augst, C. I. Moore, J. Peatross, and D. D. Meyerhofer, in *Short Wavelength Coherent Radiation: Generation and Applications*, edited by P. H. Bucksbaum and N. M. Ceglio, (OSA, Monterey, CA, 1991), Vol. 11, pp. 23-27.

"Barrier Suppression Ionization and High-Order Harmonic Generation in Noble Gases at Laser Intensities of 1 Atomic Unit and Above," D. D. Meyerhofer, S. Augst, C. Moore, J. Peatross, J. H. Eberly, and S. L. Chin, in *Multiphoton Processes*, edited by G. Mainfray and P. Agostini, (CEA, Paris, 1990), pp. 317-323.

ACKNOWLEDGMENTS

I am grateful to Dr. David Meyerhofer for the excellent supervision throughout the course of my research at the Laboratory for Laser Energetics. I appreciated his skillful blend of direction and autonomy. I also wish to thank Dr. Joseph Eberly, my advisor within the Department of Physics and Astronomy, for his thoughtful critiques and suggestions, especially in regards to this thesis.

I would like to thank a number of my fellow graduate students from whom I learned many important experimental skills. I thank Yung-Ho Chuang who taught me much about the laser system, and Steve Augst who instructed me on the techniques used in our atomic physics measurements. I thank Brian Buerke for many insightful conversations, Benedikt Soom for his much assistance with the laser system, and Yoram Fisher for setting up the CCD camera.

The support staff of the Laboratory for Laser Energetics has been very helpful in providing resources and expert advice. In particular, I wish to single out Dick Fellows for teaching me machining skills and for welding together many components of the vacuum chamber.

This work was supported by the National Science Foundation under contract PHY-9200542 Additional support was provided by the U.S. Department of Energy Office of Inertial Confinement Fusion under Cooperative Agreement No. DE-FC03-92SF19460 and the University of Rochester.

ABSTRACT

The far-field angular distributions of high-order optical harmonics have been measured. Harmonics up to the 41st order were observed in the light scattered from noble gas targets subjected to very intense pulses of laser radiation with wavelength 1053nm. The experimental conditions minimized collective effects such as phase-mismatch due to propagation or refractive index effects caused, for example, by free electrons arising in the ionization of the target Ar, Kr, or Xe atoms.

The angular distributions of many harmonic orders, ranging from the low teens to the upper thirties, all of which emerge collinear to the laser beam, could be distinguished and recorded simultaneously. Gaussian laser pulses, 1.25-times-diffraction-limited and 1.4ps duration, were focused to intensities ranging from 1×10^{13} W/cm^2 to 5×10^{14} W/cm^2 using f/70 optics. A novel gas target localized the gas distribution to a thickness of about 1mm, less than one tenth of the laser confocal parameter, at pressures of 1 Torr and less. The narrow and low-density gas distribution employed in these experiments allows the harmonics to be thought of as emerging from atoms lying in a single plane in the interaction region. This is in contrast with previously reported harmonic generation experiments in which propagation effects played strong roles. At these pressures, an order of magnitude below pressures used in other experiments, free electrons created by ionization of target atoms had a negligible effect on the far-field harmonic profiles.

We have found that the far-field distributions of nearly all of the harmonics exhibit a narrow central peak surrounded by broad wings of about the same width as the emerging laser beam. The relative widths and strengths of the wings have been found to vary with harmonic order, laser intensity, and atomic species. Since the intensity varies radially across the laser beam in the atomic source plane, an intensity-

dependent phase variation among the dipole moments of the individual atoms can give rise to constructive and destructive interferences in the scattered light. This appears to be the fundamental cause of the broad wings observed.

TABLE OF CONTENTS

CHAPTER 1: INTRODUCTION 1

- 1.1 HIGH-ORDER HARMONIC GENERATION 3
- 1.2 MEASUREMENT OF THE HARMONIC FAR-FIELD PATTERN 9
- 1.3 OUTLINE 12
- REFERENCES 15

CHAPTER 2: EXPERIMENTAL CONDITIONS 20

- 2.1 EXPERIMENTAL EQUIPMENT 21
  - A Experimental Chamber 21
  - B Spectrometer Design and Alignment 28
  - C Spectrometer Resolution 29
  - D Detector Dynamic Range 33
  - E Tradeoffs in the Detector Configuration 34
- 2.2 LASER CHARACTERISTICS 37
  - A Laser System 38
  - B Focusing Characterization 41
- 2.3 REFRACTION OF THE LASER BY FREE ELECTRONS 45
- REFERENCES 51

CHAPTER 3: GAS TARGET 54

- 3.1 GAS TARGET DESIGN 55
  - A Gas Target Dimensions 58
  - B Molecular Flow Range 58

3.2 CALCULATION OF TRAJECTORIES IN A MONTE-CARLO SIMULATION 59
  - A Calculation of Gas Density within the Target 62
  - B Gas Flow Rate 66
  - C Sensitivity of Gas Flow and Density to the Nature of the Surfaces 68

3.3 EXPERIMENTAL MEASUREMENT OF GAS DENSITY 68

REFERENCES 76

CHAPTER 4 EXPERIMENTAL RESULTS 77

4.1 FAR-FIELD ANGULAR DISTRIBUTION 77

4.2 DEPENDENCE ON GAS TARGET PARAMETERS 79
  - A Dependence on Target Position 81
  - B Dependence on Target Thickness 81
  - C Dependence on Pressure 82

4.3 DEPENDENCE ON LASER PARAMETERS 83
  - A Dependence on Laser Intensity 88
  - B Highest Harmonics Observed 94
  - C Dependence on Beam Polarization 94
  - D Harmonics of Green Light 95

4.4 ATOMIC SPECIES DEPENDENCE 99

4.5 FLUCTUATIONS AND ERRORS 101

REFERENCES 108

CHAPTER 5: RADIATION BY A COLLECTION OF DIPOLES 110

5.1 RADIATION FROM A TWO-DIPOLE SYSTEM 110

5.2 HARMONIC GENERATION IN A MANY DIPOLE SYSTEM 117

5.3 HARMONIC EMISSION INDUCED BY AN APPLIED FIELD 118

5.4 APPLICATION OF THE PHASE-MATCHING INTEGRAL 126

A Harmonic Generation by a Plane Wave Incident on a Cylindrical Medium 126

B Harmonic Generation by a Focused Laser in a Thin Medium 130

5.5 EXPLANATION OF THE FAR-FIELD WINGS 132

REFERENCES 135

CHAPTER 6: INTENSITY DEPENDENCE OF THE DIPOLE PHASE: A CAUSE OF BROAD WINGS IN THE FAR-FIELD PROFILE 136

6.1 HARMONIC EMISSION FROM A CLASSICAL ANHARMONIC OSCILLATOR 136

A Parameterization of an Anharmonic Oscillator Model 137

B Far Field Patterns 142

6.2 POSSIBLE ORIGINS OF THE INTENSITY-DEPENDENT PHASE 145

REFERENCES 147

CHAPTER 7: CONCLUSION 149

APPENDIX A: GAS TARGET COMPUTER PROGRAM 150

APPENDIX B: HARMONIC EMISSION FROM A FOCUSED LASER CALCULATED FROM A SIMPLE POWER LAW 160

REFERENCES 172

APPENDIX C: THE EFFECT OF IONIZATION ON THE HARMONIC FAR-FIELD ANGULAR PATTERN 173

APPENDIX D: ANALYSIS OF AN ANHARMONIC OSCILLATOR 178

REFERENCES 186

LIST OF TABLES

5.1 The phase mismatch associated with propagating though 1mm of neutral Xe and a fully ionized gas (1 electron per atom). The values are calculated at 1 Torr and 300°K, and the fundamental wave length is 1054nm. 125

LIST OF FIGURES

1.1 A schematic of (a) the harmonic production as a function of harmonic order in the perturbative regime , and (b) the 3rd and 5th harmonic production as a function of laser intensity. Both plots are done with a log-log scale. 2

1.2 The harmonic emission from a 15 Torr, 1mm distribution of Xe observed by L'Huillier et al. The 1064nm, 36ps laser pulse was focused to a 4mm confocal parameter. The peak laser intensities for each curve from top to bottom are 3×10^{13}, 1.3×10^{13}, 9×10^{12}, 7×10^{12}, and 5×10^{12} W/cm^2. [reproduced from Ref. 21, Fig. 1] 5

1.3 The emission for the 5th and 17th harmonics generated in Xe as a function of laser intensity observed by L'Huillier et al. [reproduced from Ref. 21, Fig. 2] 6

1.4 The far-field patterns of the 13th, 15th and 17th harmonics emitted from Xe (thick), Kr (thin), and Ar (dashed). Each curve is a four shot average. The grey line depicts the laser profile. The 1.5ps, 1054nm laser pulse was focused with a 1.2cm confocal parameter into 1mm gas distributions of pressures 0.5 Torr, 1.2 Torr, and 2 Torr respectively. The peak laser intensities were 9×10^{13}, 1.2×10^{14} and 2.1×10^{14} W/cm^2 respectively. 11

2.1 A top-view schematic of the vacuum chamber. The distance from the lens to the focus is approximately 1.5 m. 22

2.2 The gas target operating system from the side view of the vacuum chamber. 23

2.3 Convectron gauge calibration curve for Xe. The two lines visible were produced from separate gauges which operated in different pressure ranges. 25

2.4 Schematic of the experimental setup, including the gas target and the angularly resolved spectrometer. 26

2.5 High harmonics generated in Xe as captured by the CCD camera on the detector screen. Twenty images were averaged together to produce this picture. 27

2.6 Electron micrograph of the 0.2μm-period, 0.5mm-thick free standing gold grating. The perpendicular 4μm grating substructure is apparent. [Ref. 3] 32

2.7 An average of five harmonic images produced in 0.5 Torr Xe at 9×10^{13} W/cm^2. The spectrometer used a 500μm slit and a 1μm grating. 36

2.8 Schematic of the chirped-pulse-amplification laser system. 37

2.9 Schematic of the 9mm amplification system. The pulse enters the system by reflecting off the first polarizer and transmitting through the second one, the polarization being rotated by the Pockel cell. Before the pulse returns to the Pockel cell, the voltage on the cell goes to zero so that it has no effect. The pulse is spatial filtered between the second and the final pass through the amplifier. 40

2.10 The laser distribution for various positions in front and behind the focus. The pictures were taken by imaging the laser focus with a magnification of 4 into a CCD camera. 43

2.11 Plot of the measured laser beam waist as a function of axial position along the focus, showing that the beam is 1.25 times diffraction limited with f/70 optics. The solid line shows the theoretical diffraction limit. 44

2.12 A schematic depicting the imaging technique used to study defocusing from free electrons. The imaged spot gets smaller.when the beam undergoes refraction at the origin. 46

2.13 The imaged laser focus as a function of intensity and gas target pressure. The first row shows images with 0.6 Torr of Xe in the target, and the second row shows the same scan for approximately 3 Torr. The gas target is positioned at the laser focus. 47

2.14 A scan of the imaged laser focal spot radius for several gas pressures and intensities. The horizontal axis refers to the position along the beam axis of the camera relative to the imaged focus. Refraction from free electrons causes the imaged focus to grow smaller and to shift toward the imaging lens. The gas target is positioned at the laser focus. 48

3.1(a) A cutaway view of the two cylindrical gas target pieces that are glued together at their outer rims. Gas is fed into the outer ring-shaped pocket. 56

3.1(b) An inside view of a single gas target piece that shows the ring-shaped pocket from which the gas flows across the thin plate toward the center hole. 56

3.1(c) A photograph of two gas targets. One has been glued together and the other is unassembled. The scale shown is in centimeters. 57

3.2(a) The density of the gas as a function of z (the cylindrical axis) for five different radii uniformly spaced inside of the target hole. The origin is at the target center. The density is relative to the density of gas backing the device. 64

3.2(b) The distribution of gas particles in the target as a function of radius (z = 0) from the target center out to the inside edge of the gas pocket (r = 4 mm), where the density is assigned a value of 1. The target hole's cylindrical wall is at r=0.25mm. 65

3.3 The experimental setup for measuring the gas density just inside the target opening and outward along the z-axis. 71

3.4 The calculated density of the gas as a function of z along the cylindrical axis [see Fig. 3.2(a)] compared with its convolution with the detector resolution. 72

3.5 A comparison between the predicted and measured gas density profiles for a backing pressure of 1.7 Torr. The triangles are the predicted values, and the squares are the measured ones. The third square shows a typical error bar from the experimental fluctuations. 73

3.6 The measured density of the gas as a function of z (the cylindrical axis) for ten different backing pressures: 0.6, 0.8, 1.2, 1.7, 2.5, 4, 6, 8, 12, and 17 Torr. The recombination light measured by the photo-multiplier tube is proportional to the square of the gas density. 74

3.7 The measured density in the target opening plotted against the backing pressure. The solid line, which is shown for comparison, has a slope of 1. The recombination light measured by the photo-multiplier tube is proportional to the square of the gas density. 75

4.1 The far-field angular profiles of the 11th through 21st harmonics produced in 0.3 Torr Xe at an intensity of 8×10^{13} W/cm^2. The profiles were obtained from a single shot. 78

4.2 The far-field angular profiles of the 11th through the 21st harmonics produced with 0.5 Torr Xe and 8×10^{13} W/cm^2 (at focus) for shots at three target positions: $z=-1.7z_0$, $z=0$, and $z=+1.7z_0$. 80

4.3 The total harmonic energy plotted as a function of target pressure. Each point is a 20-shot average taken in Xe at 5.3×10^{13} W/cm^2. 84

4.4 The relative harmonic energy for the 11th through 27th harmonics in Xe as a function of laser intensity. The pressure has been varied to keep the detector from saturating, and the measured signal was adjusted by the square of the pressure. Each point is an average of approximately 20 shots (typical fluctuation 25%). The uncertainty in the absolute laser intensity is 35%. 85

4.5 (a) Images of the angular distributions of harmonics generated in Xe as a function of laser intensity at 0.85 Torr. (b) A similar intensity scan for Xe as in (a), but the pressure is varied so that the detector signal remains roughly constant. Each image is an average of 20 shots. 86-87

4.6 The harmonic energies as a function of harmonic order for various laser intensities in Xe. The gas pressure was varied for the different data points to avoid detector saturation, and the measured signal was adjusted by the square of the pressure. Each point is an average of approximately 20 shots (typical fluctuation 25%). The uncertainty in the absolute laser intensity is 35%. 90

4.7 (a) Images of the angular distributions of harmonics generated in Kr as a function of laser intensity at 2 Torr. (b) A similar intensity scan for Kr as in (a), but the pressure is varied so that the detector signal remains roughly constant. Each image is an average of 20 shots. 91-92

4.8 Images showing the highest-order harmonics observed in Xe, Kr, and Ar respectively. The gas pressures were 1 Torr, 2 Torr, and 4 Torr respectively. Except for the highest harmonics, the central peaks on the harmonics are well saturated. Each image is an average of about 4 shots. 93

4.9 Harmonic production at $7\text{x}10^{13}$ W/cm^{2} laser intensity as a function of laser ellipticity for Xe (a) and Kr (b). 96

4.10 (a) Far-field images of the harmonics of green light (527nm) produced in 1.5 Torr Xe as a function of laser intensity. (b) Far-field images of the harmonics of green light produced at $1\text{x}10^{14}$ W/cm^{2} for different gas pressures. Each image is an average of approximately 10 shots. 97-98

4.11 The far-field patterns of the 11th-21st harmonics emitted from Xe (thick line), Kr (thin line), and Ar (dashed line). Each curve represents a single shot. The gas pressures were 0.5 Torr, 1.2 Torr, and 2 Torr, and the peak laser intensities were $9\text{x}10^{13}$ W/cm^{2}, $1.2\text{x}10^{14}$ W/cm^{2}, and $2.1\text{x}10^{14}$ W/cm^{2} respectively. 100

4.12 The angular profile of the 13th harmonic obtained from a single shot in Xe at 0.3 Torr and 7×10^{13} W/cm^{2}. The laser profile is depicted for comparison. 103

4.13 A superposition of harmonic profiles from 5 different shots for the same conditions as in Fig. 4.12. Each curve is for the 13th harmonic. 104

4.14 The 13th harmonic profile obtained from an average of approximately 20 images for the same conditions as in Fig. 4.12. The laser profile is depicted for comparison. 105

4.15 A sampling of the noise in between the 13th and 15th harmonic lines for the same 20-shot averaged image used to generate Fig. 4.14. 106

4.16 The curve of Fig. 4.14 superimposed with a reflected version of itself. 107

5.1 Two identical dipole radiators positioned side by side shown with the coordinate system used. 112

5.2 The average power radiated from a two dipole system as a function of dipole separation for five different relative phases. The power is expressed in units of the power radiated from a single dipole. 113

5.3 A collection of dipole emitters which radiate into the surrounding space shown with the coordinate system used. 116

5.4 A schematic depicting the propagation of laser harmonics into the far field. 123

5.5 A schematic of a plane wave laser field incident on a cylindrical harmonic generation medium. 128

5.6 The far-field patterns for harmonic generation by a plane wave in a uniform cylindrical medium. The thickness of the medium ℓ is 1/4 (thick solid), 1/2 (dashed), 1 (dotted), 2 (dash-dot), and 4 (thin solid) times $2k_q\rho_o^2$. The left plot shows the case $\Delta k=0$, and the right plot shows the case $\Delta k = 1/2k_q\rho_o^2$. 129

5.7 The far-field pattern for q=13, and p=13, where (a) the phase of the harmonic emission does not change with laser intensity, and (b) the phase changed by π when the laser intensity goes above 90% of its peak value. The far-field pattern shows the cumulative energy over time. No ionization is included in this calculation. 134

6.1 The conversion efficiency of the laser into the third harmonic for Ar, Kr, and Xe as a function of laser intensity. The gas target thickness is 1mm and the 1.3-times diffraction limited beam is focused with f/70 optics. 138

6.2 The harmonic emission curves for different harmonic orders given by an anharmonic oscillator model parameterized to Xe. 141

6.3 The far-field harmonic angular profiles calculated with an anharmonic oscillator model for Xe. The phase-matching parameters are those used in experiments. 143

6.4 The far-field harmonic angular profiles calculated for the identical conditions as Fig. 6.3 except that the phase of the emitted harmonics is held constant. 144

B.1 The far-field profile (square modulus of the integral in Eq. (B.7)) for a thin target, ℓ=b/10, for several target positions (solid line). The dashed line is the laser profile, the dotted line is the laser profile to the p^th^ power, and the dot-dashed line is the laser profile to the p^2/q power. For all figures, q=25, p=5, and Δk=0. 165

B.2 The far-field profile (square modulus of the integral in Eq. (B.7)) for a thin target, ℓ=b/10, for several values of q (solid line). The dashed line is the laser profile, the dotted line is the laser profile to the p^2/q power. For all figures p=5 and $\Delta k=0$, and the target is positioned at the origin z=0. The cases for q=63 and q=125 are shown twice using different scales so that the structure is more apparent. 166

B.3 The far-field profile (square modulus of the integral in Eq. (B.7)), for several target thicknesses (solid line). The dashed line is the laser profile, the dotted line is the laser profile to the $p^{\underline{th}}$ power, and the dot-dashed line is the laser profile to the p^2/q power. For all figures q=31, p=5 and $\Delta k=0$, and the target is positioned at the origin z=0. 167

B.4 The modulus of the harmonic electric field distribution in the laser focus for various values of q and p: (a) q=7, p=5, (b) q=13, p=5, (c) q=21, p=5, (d) q=13, p=2, (e) q=13, p=8, (f) q=13, p=5, $\Delta k z_0 \cong 2$. The dipole medium is centered at the laser focus and has a thickness $\ell \equiv b/2$. [reproduced from Ref. 3, Fig. 12] 169

B.5 The far-field profile (square modulus of the integral in Eq. (B.7)) for the same conditions as used to generate Fig. B.4 (ℓ=b/2). The dashed line is the laser profile. 170

B.6 The far-field profile (square modulus of the integral in Eq. (B.7)) for the same conditions as were used to generate Fig. B.4 except that the gas distribution is taken as ℓ=b/10, the thickness used for the experiments in this thesis. The dashed line is the laser profile. 171

C.1 The far-field pattern calculated by Eqs. (C.7) and (C.8) for peak laser intensities below and above the ionization saturation intensity I_S. For this calculation, q=25, p=5 and w=b/10. The gas density was taken at 1 Torr. The far-field pattern shows the cumulative energy over time which includes the effects of the evolution of the ionization. 177

D.1 (a) The absolute value of the harmonic components of motion for an anharmonic oscillator as a function of the driving field [see Eqs. (D.1), (D.3), and (D.8)]. For this log-log plot, ω_0/ω_L=10, and Γ/ω_L=0.01. (b) The real part of the harmonic component plotted on a linear scale. 184-185

CHAPTER 1

INTRODUCTION

Laser light can be made sufficiently intense such that it can modify the physical properties of any material. When this occurs, the interaction between the light and the material becomes nonlinear. One such interaction in a material is the conversion of light into harmonics of the applied frequency. Laser harmonic generation was first discovered by Franken et al.[1] in 1961 when the second harmonic of a Ruby laser was created in a solid. Since then, harmonic generation has been an important topic in the field of nonlinear optics.

Experimental harmonic generation was well described for many years within a perturbative framework; each successive harmonic order generated by an applied field was much less intense and had no impact on the harmonics of lower order. Each harmonic depended only on harmonics of a lesser order and on the laser field. According to lowest-order perturbation theory, the strength of the harmonic emission depends on the strength of the applied field raised to the power of the harmonic order. For example, the intensity of the third harmonic is proportional to the third power of the laser intensity. The traditional formulation of nonlinear susceptibility implies this kind of behavior. That is, the component of the polarization within the medium which oscillates with the harmonic frequency is written as $P_q = \chi_q(\omega)E^q$, where E is the amplitude of the laser field, q is the harmonic order, and χ_q is the nonlinear susceptibility. χ_q is generally considered to be independent of the field strength. For a review of this topic, consult almost any nonlinear optics textbook.[2-5] Fig. 1.1 shows the general behavior of harmonic production in the perturbative regime.

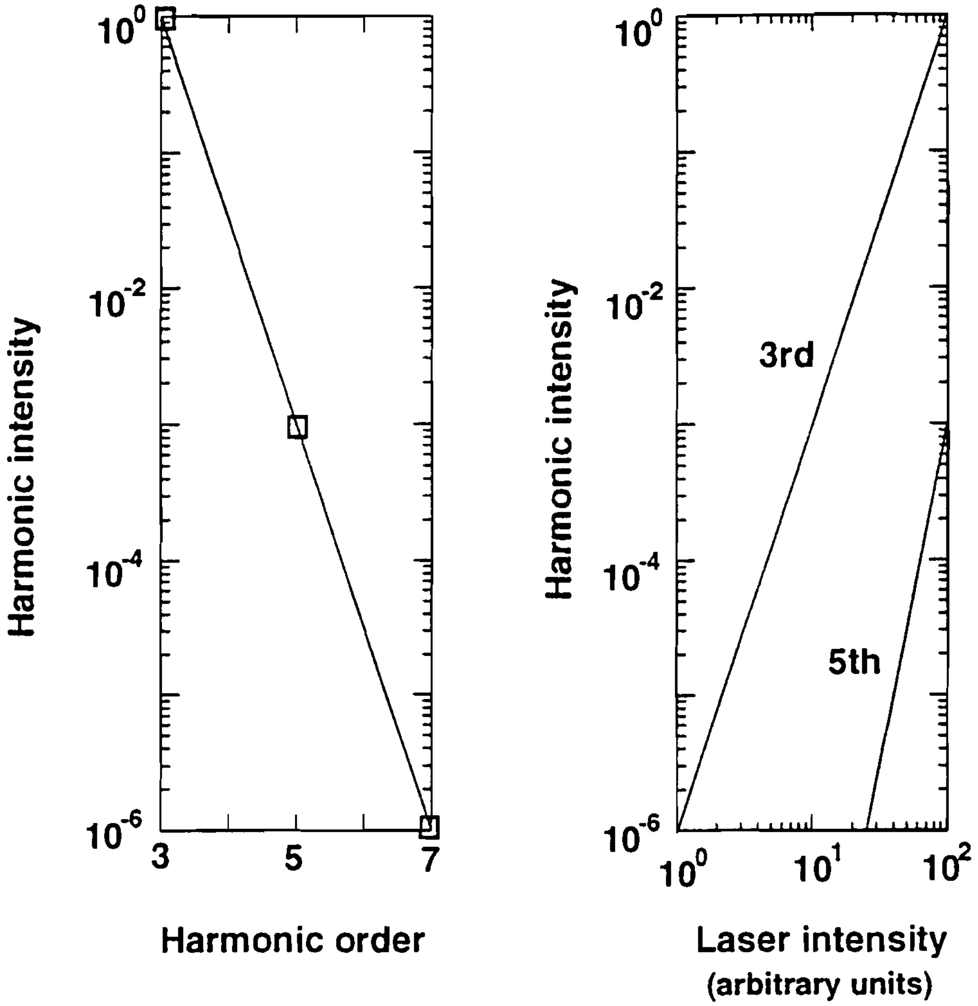

Fig. 1.1 A schematic of (a) the harmonic production as a function of harmonic order in the perturbative regime , and (b) the 3rd and 5th harmonic production as a function of laser intensity. Both plots are done with a log-log scale.

Harmonic generation depends as much on the macroscopic arrangement of the atoms as it does on the individual atomic response to the laser field. To achieve the high laser intensities necessary to induce harmonic generation, the laser often must be focused into the medium. In the neighborhood of the focus, the laser beam wavefront experiences strong phase variations as the beam undergoes diffraction. In addition, the laser wavelength usually has a different refractive index in the medium than the harmonic wavelengths. These two effects contribute to phase mismatches between the laser field and the harmonic fields which can strongly influence the efficiency of the interaction. These phase effects, first studied by D. A. Kleinman in 1962, are well understood within the framework of perturbation theory.[6-11]

1.1 HIGH-ORDER HARMONIC GENERATION

Until the late 1980's, the highest harmonic orders generated and observed in materials were not much past the 5th, and the shortest resulting wavelengths were about 100nm.[11] In 1987, McPherson et al.[12] observed surprisingly intense generation of up to the 17th harmonic of a 248nm KrF laser focused into neon vapor. This produced coherent radiation at a wavelength of 15nm, which is far into the ultra-violet. Soon after, Ferray et al.[13] reported the similarly striking generation of harmonic orders up to the 33rd by a 1064nm laser focused into argon vapor. Though the conversion efficiencies for these very high-order harmonics are several orders of magnitude less than the conversion efficiencies of lower-order harmonics generated in solids or metal vapors, they are surprising in the sense that they depart markedly from the perturbative trend illustrated in Fig. 1.1 (a). Typical data shown in Fig. 1.2 illustrates the new phenomenon, a "plateau" of harmonics that is almost flat for several or many orders as the laser intensity is increased. The very high-order harmonic production is made possible by laser fields which are able to influence strongly the tightly bound electrons in atoms such as the noble gases. The required intensities, on the order of 10^{14} W/cm^2, have become readily available only in the last decade. Since those initial observations,[12,13] a number of groups have been studying the phenomenon of high-order harmonic generation. High harmonics are seen in many of the noble gases. With the KrF laser, harmonics up to the 25th order have been observed.[14,15] Harmonics up to the 135th have been generated in He and Ne by a 1054nm, 1ps laser.[16] These harmonics have photon energies in excess of 100eV, far above the ionization potentials of the atom. High harmonics with similar photon energies have been reported by groups using the same or other laser wavelengths.[15-20]

The experimental data in Fig. 1.2 was taken by L'Huillier and co-workers, who have been very active in researching high-harmonic generation [Ref. 21, Fig. 1]. The figure shows harmonics of a 1064nm, 36ps laser pulse which was focused to peak intensities around 10^{13} W/cm^2 in a 1mm thick distribution of Xe at a pressure of 15 Torr. As the laser intensity increases, the plateau is evident. At the higher intensities, the higher-order harmonics are almost as strong as the lower-order ones. The plateau is strikingly inconsistent with lowest-order perturbation theory, which assumes that each harmonic order is much weaker than the previous ones [recall Fig. 1.1 (a)]. At the lowest laser intensities shown, the strength of the harmonics falls off more rapidly with increasing order. If even lower intensities were shown in Fig. 1.2, the harmonics would diminish very quickly with increasing order, a behavior consistent with lowest-order perturbation theory. Thus, lowest-order perturbation theory is able to describe harmonic generation up to a certain point. If the laser intensity becomes too strong, the description is no longer sufficient to explain the results. A simple way to understand why this is so is the following: if each harmonic of higher order depends on the laser intensity raised to an increasingly higher power, then there must exist an intensity at which the steeper higher-order curves catch up to the lower-order curves. At this point, the assumptions from which the power laws were derived are violated.

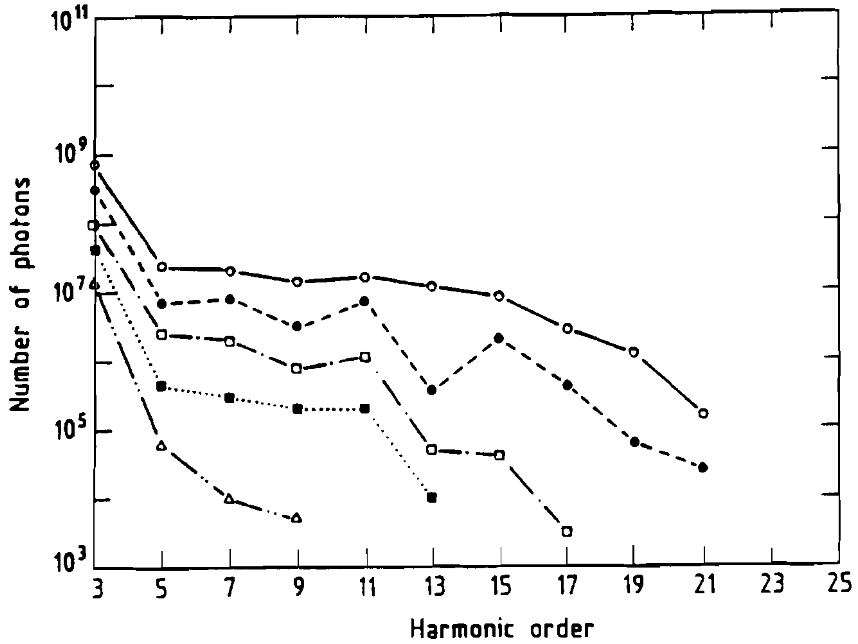

Fig. 1.2 The harmonic emission from a 15 Torr, 1mm distribution of Xe observed by L'Huillier et al. The 1064nm, 36ps laser pulse was focused to a 4mm confocal parameter. The peak laser intensities for each curve from top to bottom are $3\text{x}10^{13}$, $1.3\text{x}10^{13}$, $9\text{x}10^{12}$, $7\text{x}10^{12}$, and $5\text{x}10^{12}$ W/cm^2. [reproduced from Ref. 21, Fig. 1]

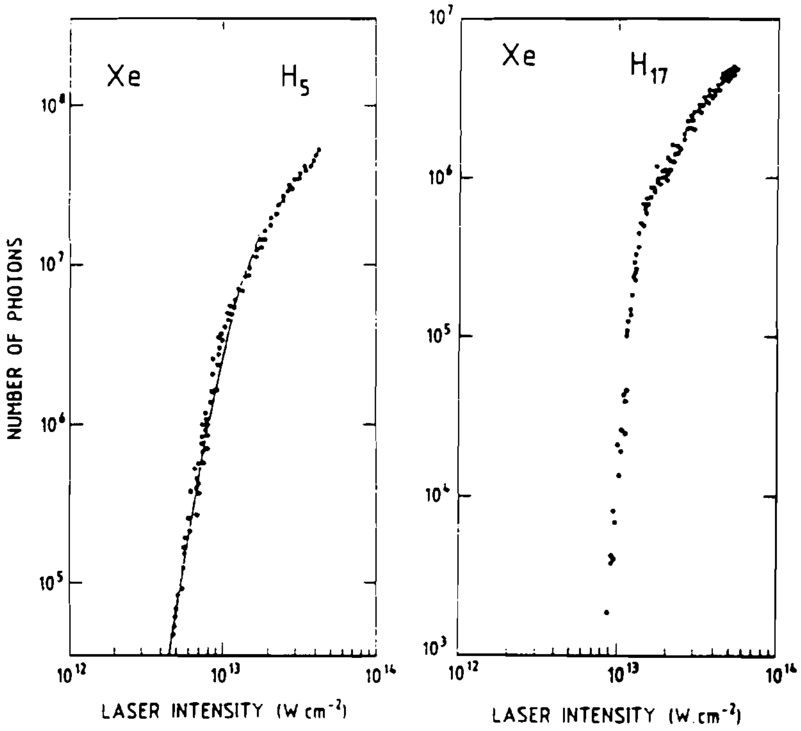

Fig. 1.3 The emission for the 5th and 17th harmonics generated in Xe as a function of laser intensity observed by L'Huillier et al. [reproduced from Ref. 21, Fig. 2]

Fig. 1.3 shows the amount of emission for the 5th and 17th harmonics generated in Xe as a function of laser intensity [Ref. 21, Fig. 2]. Again this data was taken by L'Huillier and co-workers under the same conditions as described above. The rapidly-increasing portion of the curves is consistent with the intensity-to-the-qth-order power law described by perturbation theory. In the intensity region where the plateau occurs, the harmonic energies discontinue their rapid increase. Such a sharp deviation from the power law as seen at the top of the curves is another illustration of the failure of perturbation theory. Curves similar to those shown in Figs. 1.2 and 1.3 have been generated for many of the noble gases.[12-16,19-30]

This thesis presents a study of high order ($q \geq 11$) harmonics of 1054nm light generated in thin samples of Xe, Kr, and Ar vapors. The rare gases are of interest specifically because they exist as single atoms. The primary goal of this work is to study high-field atomic physics. The physics of atoms in strong light fields is a topic of considerable research activity.[31,32] An investigation of harmonic generation by single atoms can help provide an understanding of how an atom interacts with the light. The work presented in this thesis minimized complicated propagation effects common to most harmonic generation experiments. This made the single-atom response to the laser more accessible to interpretation. A secondary goal of this work is to better characterize high-harmonic generation since the harmonics might prove to be a useful source of coherent vacuum ultraviolet radiation.

High-order harmonic generation is the strongest at laser field intensities where ionization readily occurs. For this reason, gases are the most suitable medium for high-harmonic generation. At these intensities solid materials would be damaged beyond use but a gas is self-healing. In addition, gases tend to have the deepest electron binding potentials, and there is evidence that this is associated with the creation of higher harmonic orders. Because single-atom potentials are centrosymmetric, they create only the odd harmonics, as opposed to solids which in general have noncentrosymmetric potentials and can create both even and odd harmonics. This may be understood through classical arguments or through quantum-mechanical angular-momentum selection rules.

Given the relatively high gas pressure required to observe high-order harmonic emission, it was initially considered to be a collective many-atom phenomenon. However, in 1989 Kulander and Shore[33,34] and Eberly, et al.[35-37], showed that plateau formation and the generally non-perturbative behavior of the harmonic emission similar to the earliest experimental reports are strictly a consequence of single-atom dipole response. Their analysis used the atomic wave function (obtained exactly numerically for a one-electron atom) to calculate the dipole moment and its spectrum. Subsequent refinements of the atomic model and the incorporation of propagation effects, by a Saclay-Livermore collaboration, have led to good quantitative agreement between theory and experiment in several respects.[22,29] Many other more simplified models have also shown at least qualitative agreement with experiment.[38-40]

Recently, a mostly classical picture put forward by K. Kulander, K. Schafer, P. Corkum and others provides physical insight into the mechanism that gives rise to the harmonics with energies far above the binding energy of the atom.[41-43] They suggest that the electron can be ionized and pulled away from the atom by the laser field. When the oscillating laser field reverses direction, the electron is pushed back toward the atom where it can collide, releasing a photon with energy up to the ionization potential V_0 plus about three times the ponderomotive potential U ($U \equiv e^2E^2/4m\omega^2$). The ponderomotive potential is the average kinetic energy of oscillation that a free electron has in the laser field. The number of harmonics contained in the plateau for given laser parameters and atomic species appears to agree well with the V_0+3U rule.[16,17,19,43]

1.2 MEASUREMENT OF THE HARMONIC FAR-FIELD PATTERN

Until recently, experiments have measured the total harmonic emission, temporally and angularly integrated. The temporal and angular structure can provide additional information about the harmonic emission process. Recent work by Faldon, et al., explored the effects of ionization on the temporal structure of the high order harmonics with a 50ps laser pulse.[44] Smith, et al., have recently observed the angular distributions of high-order harmonics in He near the end of the plateau.[21] Augst, et al., who explored harmonics produced in Xe and Kr, were the first to observe the far-field angular distributions of high-order harmonics.[45] In these, and in all other high harmonic experiments known to the author, the gas target pressure was at least a few Torr and, typically, much higher. At these pressures the effects of phase-mismatches caused by ionized electrons cannot be ignored. It seems likely that the broad featureless far-field patterns first observed by Augst, et al.[45], were dominated by effects of free electrons and tight focusing geometry. In contrast, this thesis presents observations of the far-field angular patterns of individual harmonics produced in gases with pressures less than 1 Torr. For these experiments, a very weak focusing geometry was employed. Under these conditions, propagation effects inside the medium are unimportant, and the harmonic far-field patterns are dominated by the atomic dipole response to the laser in the plane of the focus. The far-field angular distributions of harmonics produced in Xe, Kr, and Ar were studied at laser intensities both above and below where ionization readily occurs.

To investigate the atomic response of the medium, it is essential to characterize the propagation effects so that they can be separated out. When harmonics emitted from different locations of the interaction region have mismatched phases, the destructive interference not only affects the overall signal, but can influence the angular distribution of the emission. This is especially true if the laser intensity is high enough to ionize the medium. If the density of the ionized electrons becomes too high, the laser beam intensity profile becomes significantly modified by refraction while still in the interaction region, violating the usual approximations made in phase-matching calculations. The work presented in this thesis approaches the problem of isolating the atomic response by experimentally minimizing the propagation effects. This work constitutes the first observations of high-order harmonic generation under conditions where the propagation effects are clearly unimportant, even under conditions of strong ionization. The far-field harmonic patterns measured under these conditions reveal that the phase of the individual atomic harmonic emission varies strongly with the laser intensity.

In these experiments, the highest observed harmonics from Ar, Kr, and Xe were respectively the 41st, 35th, and 29th. Nearly all of the harmonics show an angularly narrow peak in the forward direction. The width of the peak is typically less than one third the width of the laser profile. Many harmonics show additional broad wings with about the same widths as the laser profile. Fig. 1.4 shows the measured far-field angular distribution of several harmonics generated in Xe, Kr and Ar. The laser intensity profile, which has a diameter of 14 mrad (measured from the $1/e^2$ intensity level) is depicted in the last frame for comparison. The broad wings appear differently on the various harmonics, depending on the atomic species. The appearance of the wings is a marked departure from what would be expected from lowest-order perturbation theory. The wings come about from an intensity-dependent phase of the atomic dipole. This intensity dependence implies a radial variation of the dipole phase in the interaction region because the laser intensity varies radially. Such phase variations can cause the harmonic light to interfere in the far-field, leading to the broad wings in the angular profile.

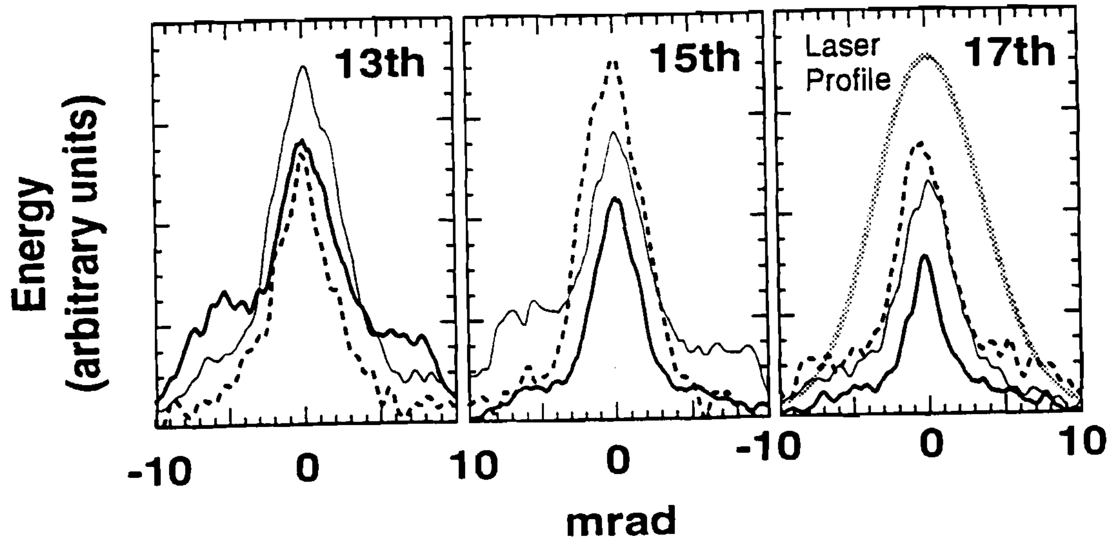

Fig. 1.4 The far-field patterns of the 13th, 15th and 17th harmonics emitted from Xe (thick), Kr (thin), and Ar (dashed). Each curve is a four shot average. The grey line depicts the laser profile. The 1.5ps, 1054nm laser pulse was focused with a 1.2cm confocal parameter into 1mm gas distributions of pressures 0.5 Torr, 1.2 Torr, and 2 Torr respectively. The peak laser intensities were 9×10^{13}, 1.2×10^{14} and 2.1×10^{14} W/cm^2 respectively.

1.3 OUTLINE

Chapter 2 explains the experimental equipment used in the production and measurement of the far-field angular distribution of the harmonics. The experimental equipment was designed to minimize phase mismatches in the interaction region. This accomplishes the goal of making the individual atomic behavior more accessible when interpreting the results. The laser is discussed, and recent improvements to the laser system are described. Limitations in the dynamic range and resolution of the harmonic spectrometer are also explained.

Chapter 3 describes the novel gas target developed specifically for these experiments. The gas target provides a well-characterized, thin (~1mm) and low-density (≤1Torr) gas distribution for the laser harmonic interaction. The low density is necessary to ensure that phase mismatches do not effect the far-field angular profile of the harmonics in a complicated way. The localization of the gas to a thin region is necessary to minimize geometric propagation effects which can also complicate the far-field angular profile of the harmonics.

Chapter 4 presents the experimental measurements of the far-field harmonic profiles. The dependence of the harmonic production on parameters such as gas density, gas distribution thickness, and target position relative to the focus shows that the experiments are indeed done in a regime where propagation effects inside the interaction region are minimal. Thus, the harmonics can be thought of as emerging from atoms lying in a single plane in the interaction region.

Chapter 5 provides an overview of the issues involved when considering radiation from a collection of dipoles. The phase-matching integral is formulated, and it provides the bridge between individual atomic responses and the observed collective emission when a gas is illuminated by a laser. The chapter gives a basis for understanding how the various macroscopic experimental parameters can influence the production of harmonics. This is important since the goal of this work is to increase our understanding of individual atomic behavior by separating out collective effects. The derivations in Chapter 5 deviate from traditional derivations in that they are not done using the language of nonlinear susceptibilities. Rather, everything is expressed in terms of the atomic dipole oscillation. The reason for this choice is that the language of nonlinear susceptibilities is built around the power laws of lowest-order perturbation theory, while we are interested in the regime where perturbation theory breaks down. The chapter explains our conclusion that the broad wings in the harmonic far-field patterns result from an intensity-dependent phase of the atomic harmonic emission. It is explained that for our conditions the wings cannot be the result of propagation effects in the focus nor the result of diffraction due to ionization.

Chapter 6 discusses the possible origins of the intensity-dependent phase which appears to cause the wings observed in the harmonic far-field profiles. A classical anharmonic oscillator, a simple model which has been successful in describing harmonic emission from atoms in weak fields, is used to describe harmonic emission in the strong-field regime of the plateau. The model is incorporated into phase-matching calculations to produce harmonic far-field profiles. The simple model illustrates the point that the broad wings arise from dipole phase variations across the source plane, and these originate in the radial intensity dependence of the laser.

Appendix A is a printout of the computer code used to calculate the gas density and flow rate in the gas target. Appendices B and C make specific application of formulas derived in Chapter 5 to conditions appropriate to harmonic generation experiments. Appendix B investigates the geometric phase-matching effects associated with the relatively flat intensity dependence of the plateau regime for harmonics produced in a focused laser. Appendix C investigates the effects of ionization on the harmonic far-field profiles. The calculations show that for our conditions the broad wings observed in the harmonic far-field profiles cannot be attributed to these effects. Appendix D provides a simplified approximation to the motion of a driven anharmonic oscillator.

REFERENCES

1. P. A. Franken, A. E. Hill, C. W. Peters, and G. Weinreich, "Generation of Optical Harmonics," Phys. Rev. Lett. **7**, 118-119 (1961).
2. R. W. Boyd, *Nonlinear Optics* (Academic Press., San Diego, 1992).
3. P. W. Milonni and J. H. Eberly, *Lasers* (Wiley, New York, 1988).
4. N. Bloembergen, *Nonlinear Optics*, 2nd ed. (Benjamin, Reading, Massachusetts, 1977).
5. N. B. Delone and V. P. Krainov, *Fundamentals of Nonlinear Optics of Atomic Gases*, (Wiley, New York, 1988).
6. D. A. Kleinman, "Theory of Second Harmonic Generation of Light," Phys. Rev. **128**, 1761-1775 (1962).
7. G. D. Boyd and D. A. Kleinman, "Parametric Interaction of Focused Gaussian Light Beams," J. of Appl. Phys. **39**, 3597-3639 (1968).
8. J. F. Ward and G. H. C. New, "Optical Third Harmonic Generation in Gases by a Focused Laser Beam," Phys. Rev. **185**, 57-72 (1969).
9. R. B. Miles and S. E. Harris, "Optical Third-Harmonic Generation in Alkali Metal Vapors," IEEE J. Quantum Electron. **QE-7**, 470-484 (1973).
10. G. C. Bjorklund, "Effects of Focusing on Third-Order Nonlinear Processes in Isotropic Media," IEEE J. Quantum Electron. **QE-11**, 287-296 (1975).
11. J. F. Reintjes, *Nonlinear Optical Parametric Processes in Liquids and Gases*, (Academic Press, Orlando, 1984).
12. A. McPherson, G. Gibson, H. Jara, U. Johann, T. S. Luk, I. A. McIntyre, K. Boyer, and C. K. Rhodes, "Studies of Multiphoton Production of Vacuum-Ultraviolet Radiation in the Rare Gases," J. Opt. Soc. Am. B **4**, 595-601 (1987).

13. M. Ferray, A. L'Huillier, X. F. Li, L. A. Lompre, G. Mainfray, and C. Manus, "Multiple-Harmonic Conversion of 1064nm Radiation in Rare Gases," J. Phys. B 21, L31-L35 (1988).

14. N. Sarukura, K.Hata, T. Adachi, and R. Nodomi, "Coherent Soft X-Ray Generation by the Harmonics of an Ultra-High Power KrF Laser," Phys. Rev. A **43**, 1669-1672 (1991).

15. K. Kondo, N. Sarukura, K. Sajiki, and S. Watanabe, "High-Order Harmonic Generation by Ultrashort KrF and Ti:Sapphire Lasers," Phys. Rev. A **47**, R2480-R2483 (1993).

16. A. L'Huillier and Ph. Balcou, "High-Order Harmonic Generation in Rare Gases with a 1-ps 1053-nm Laser," Phys. Rev. Lett. **70**, 774-777 (1993).

17. M. Lewenstein, P. Salieres, Ph. Balcou, A. L'Huillier, M.Yu. Ivanov, J. Larsson, and C.G. Wahlstrom, "Where is the Harmonic Generation Cutoff?," Phys. Rev. Lett., submitted, (1993).

18. R.A. Smith, J.W.G. Tisch, M. Ciarrocca, S. Augst, and M.H.R. Hutchinson, "Recent Ultra-high Harmonic Generation Experiments with Picosecond Laser Pulses," to be published in the proceedings of the 3rd Conference on Super Intense Laser-Atom Physics, (NATO, Han-sur-Lesse, Belgium, 1993).

19. J.J. Macklin, J.D. Kmetec, and C.L. Gordon III, "High-Order Harmonic Generation Using Intense Femtosecond Pulses," Phys. Rev. Lett. **70**, 766-769 (1993).

20 J. K. Crane, M. D. Perry, S. Herman, and R. W. Falcone, "High-Field Harmonic Generation in Helium," Opt. Lett. **17**, 1256-1258 (1992).

21. A. L'Huillier, L. A. Lompre, G. Mainfray and C. Manus, "Multiple Harmonic Conversion in Rare Gases in Strong Laser Fields," in *Multiphoton Processes*, edited by G. Mainfray and P. Agostini, (CEA, Paris, 1990), pp. 45-55.

22. A. L'Huillier, K. J. Schafer, and K. C. Kulander, "Theoretical Aspects of Intense Field Harmonic Generation," J. Phys. B **24**, 3315-3341 (1991).

23 J. K. Crane, S. W. Allendorf, K. S. Budil, and M. D. Perry, "Resonantly Enhanced Harmonic Generation and Above-Threshold Ionization in Krypton," in *Short Wavelength Coherent Radiation: Generation and Applications*, edited by P. H. Bucksbaum and N. M. Ceglio, (OSA, Monterey, CA, 1991), Vol. 11, pp. 28-32.

24. X. F. Li, A. L'Huillier, M. Ferray, L. A. Lompre, and G. Mainfray, "Multiple-Harmonic Generation in Rare Gases at High Laser Intensity," Phys. Rev. A **39**, 5751-5761 (1989).

25. A. L'Huillier, X. F. Li, and L. A. Lompre, "Propagation Effects in High-Order Harmonic Generation in Rare Gases, "J. Opt. Soc. Am. B **7**, 527-536 (1990).

26. L. A. Lompre, A. L'Huillier, M. Ferray, P. Monot, G. Mainfray, and C. Manus, "High-Order Harmonic Generation in Xenon: Intensity and Propagation Effects," J. Opt. Soc. Am. B **7**, 754-761 (1990).

27. A. L'Huillier, K. J. Schafer, and K. C. Kulander, "High-Order Harmonic Generation in Xenon at 1064nm: The Role of Phase Matching," Phys. Rev. Lett. **66**, 2200-2203 (1991).

28. A. L'Huillier, Ph. Balcou, and L. A. Lompre, "Coherence and Resonance Effects in High-Order Harmonic Generation," Phys. Rev. Lett. **68**, 166-169 (1992).

29. A. L'Huillier, Ph. Balcou, S. Candel, K. J. Schafer, and K. C. Kulander, "Calculations of High-Order Harmonic-Generation Processes in Xenon at 1064 nm," Phys. Rev. A **46**, 2778-2790 (1992).

30. Ph. Balcou and A. L'Huillier, "Phase-Matching Effects in Strong-Field Harmonic Generation," Phys. Rev. A **47**, 1447-1459 (1993).

31. *Multiphoton Processes*, edited by G. Mainfray and P. Agostini, (CEA, Paris, 1990).
32. *Atoms in Intense Laser Fields*, edited by M. Gavrila, (Academic Press, San Diego, CA, 1992).
33. K. C. Kulander and B. W. Shore, "Calcualtions of Multiple-Harmonic Conversion of 1064nm Radiation in Xe," Phys. Rev. Lett. **62**, 524-526 (1989).
34. K. C. Kulander and B. W. Shore, "Generation of Optical Harmonics by Intense Pulses of Laser Radiation. II. Single-Atom Spectrum for Xenon," J. Opt. Soc. Am. B **7**, 502-508 (1990).
35. J. H. Eberly, Q. Su, and J. Javanainen, "Nonlinear Light Scattering Accompanying Multiphoton Ionization," Phys. Rev. Lett. **62**, 881-884 (1989).
36 J. H. Eberly, Q. Su, and J. Javanainen, "High-Order Harmonic Production in Multiphoton Ionization," J. Opt. Soc. Am. B **6**, 1289-1298 (1989).
37. J. H. Eberly, Q. Su, J. Javavainen, K. C. Kulander, B. W. Shore, and L. Roso-Franco, "High-Order Harmonic Generation During Multiphoton Ionization of Gases," J. Mod. Opt. **36**, 829-855 (1989).
38. W. Becker, S. Long, and J. K. McIver, "Higher-Harmonic Production in a Model Atom with Short-Range Potential," Phys. Rev. A **41**, 4112-4115 (1990).
39. B. Sundaram and P. W. Milonni, "High-Order Harmonic Generation: Simplified Model and Relevance of Single-Atom Theories to Experiment," Phys. Rev. A **41**, 6571-6573 (1990).
40. L. Plaja and L. Roso-Franco, "Adiabatic Theory for High-Order Harmonic Generation in a Two-Level Atom," J. Opt. Soc. Am. B **9**, 2210-2213 (1992).

41. J. L. Krause, K. J. Schafer, and K. C. Kulander, "High-Order Harmonic Generation from Atoms and Ions in the High Intensity Regime," Phys. Rev. Lett. **68**, 3535-3538 (1992).

42. K. C. Kulander, K. J. Schafer, and J. L. Krause, "Dynamics of Short-Pulse Excitation, Ionization and Harmonic Conversion," to be published in the proceedings of the 3rd Conference on Super Intense Laser-atom physics, (NATO, Han-sur-Lesse, Belgium, 1993).

43. P. Dietrich, N. H. Burnett, M. Ivanov, and P. B. Corkum, "High Harmonic Generation and Two Electron Ionization with Elliptically Polarized Light," Phys. Rev. Lett., submitted, (1993).

44. M.E. Faldon, M.H.R. Hutchinson, J. P. Marangos, J. E. Muffett, R. A. Smith, J. W. G. Tisch, and C. G. Wahlstrom, "Studies of Time-Resolved Harmonic Generation in Intense Laser Fields in Xenon," J. Opt. Soc. B **9**, 2094-2099 (1992).

45. S. Augst, C. I. Moore, J. Peatross, and D. D. Meyerhofer, "Spatial Distribution of High-Order Harmonics Generated in the Tunneling Regime," in *Short Wavelength Coherent Radiation: Generation and Applications*, edited by P. H. Bucksbaum and N. M. Ceglio, (OSA, Monterey, CA, 1991), Vol. 11, pp. 23-27.

CHAPTER 2

EXPERIMENTAL CONDITIONS

An important goal of this work is to present evidence that the strong-field response of individual atoms can contribute significantly to harmonic far-field emission patterns. In particular, when harmonic light emitted from different locations of the interaction region has mismatched phases, the resulting interference can strongly influence the angular distribution of the emission. Collective effects such as field propagation in an extended target volume can obscure individual atomic response, and we have worked to reduce their role. In addition, if the laser intensity is strong enough to produce free electrons in the interaction region, and if the density of the free electrons becomes too high, the laser beam can become significantly modified by refraction while still in the target volume. This effect has also been minimized.

In this chapter we describe the experimental setup and the spectrometer used to detect the harmonics. The focusing quality of the laser beam as well as other characteristics of the laser are also described. In addition, we discuss how to minimize the effects of refraction of the laser beam due to ionization of the atomic medium. Details of a gas target which accomplishes this are given in Chapter 3.

2.1 EXPERIMENTAL EQUIPMENT

2.1.A Experimental Chamber

To accommodate the special requirements of these experiments and to avoid conflicts with other experiments in the laboratory, it was necessary to construct a separate experimental vacuum chamber. The chamber was designed and constructed primarily out of existing equipment. Fig. 2.1 shows a top-view schematic of the vacuum chamber. The laser beam enters the system through a 153cm lens which is mounted on the end of a long tube. The lens itself serves as the vacuum window. The laser focuses to the middle of the central tank where the gas target is positioned. The chamber is evacuated by a diffusion pump with an 8 inch throat. The background pressure is below 10^{-6} Torr. The long tube connects to the central tank through a flexible bellows which allows the lens to be accurately positioned. Once the tube's position is set, a fastener holds it securely in place.

Near the focus, the laser intersects a thin gas target which provides a low-density gas distribution. The target consists of two thin metal plates separated by a small gap wherein gas flows. A small hole drilled in the plates allows the laser to pass through and interact with the gas. The density of the gas within the hole remains relatively high, while outside of the hole it disperses quickly. To align the target, it is necessary to observe the laser beam emerging from the target. However, when the harmonic spectrometer is in place (described later), the forward path of the laser is blocked. A mirror attached to a mechanical lever allows the emerging laser beam to be momentarily diverted out through the side window.

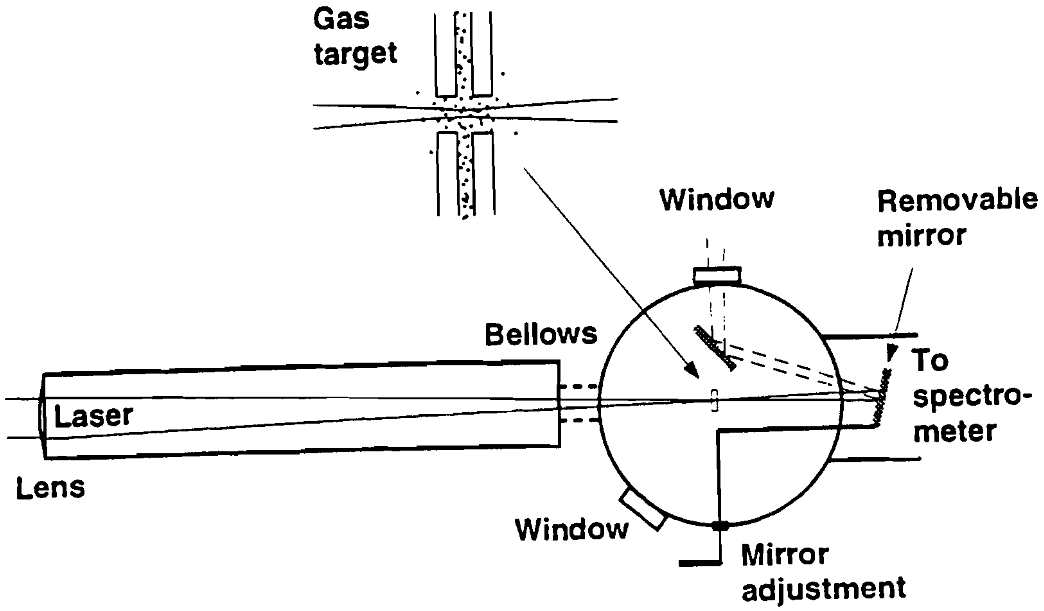
Gas
target
Window
Removable
mirror
Bellows
To
spectro-
meter
Laser
Lens
Window
Mirror
adjustment

Fig. 2.1 A top-view schematic of the vacuum chamber. The distance from the lens to the focus is approximately 1.5 m.

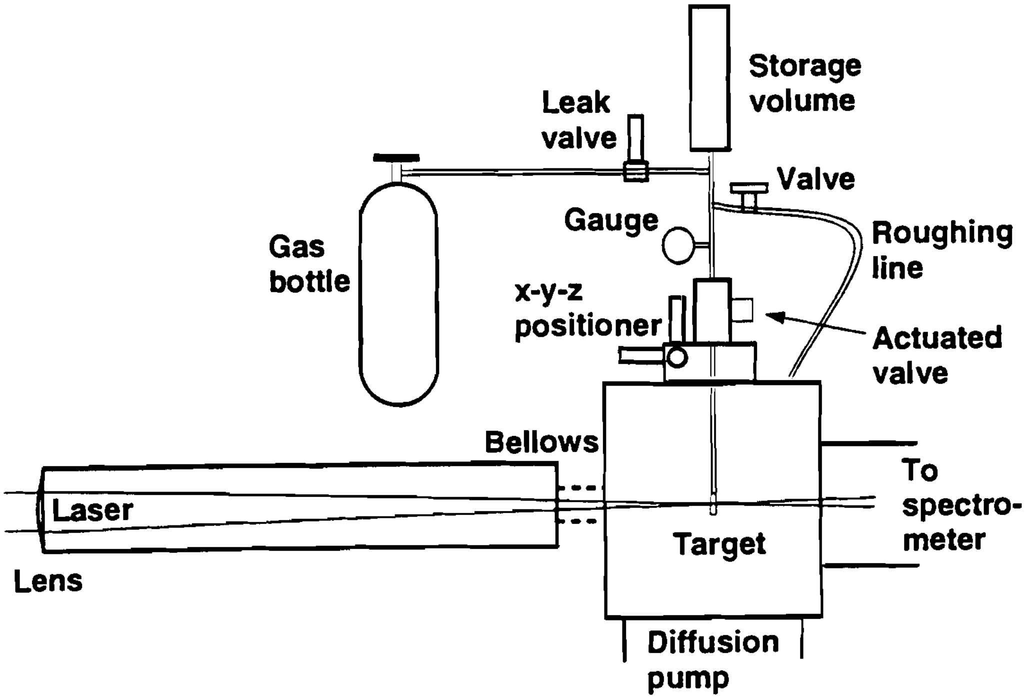
Storage volume
Leak valve
Valve
Gauge
Gas bottle
Roughing line
x-y-z positioner
Actuated valve
Bellows
Laser
Lens
Target
To spectro-meter
Diffusion pump

Fig. 2.2 The gas target operating system from the side view of the vacuum chamber.

Fig. 2.2 shows the system which operates the gas target from the side view of the vacuum chamber. The gas is fed into the target through a long tube which also serves as a holder. The tube is held by an x-y-z positioner, and an actuated valve allows gas to flow into the tube from the storage volume when the laser fires. The valve opens for about a second so that the flow can be thought of as continuous rather than pulsed. The inner diameter of the tube is much wider than the dimensions of the target opening, so the gas pressure backing the target is well approximated by a gauge reading on the storage volume. A leak valve allows the storage volume to be filled accurately to the desired pressure, typically a few Torr (as opposed to many atmospheres in the gas bottle).

The pressure is measured with a Granville-Phillips convectron gauge (series 275). The response of the gauge to He, Ne, Ar, and Kr is provided in the gauge documentation, but the response to Xe is not. The convectron gauge was calibrated for Xe using two mechanical pressure gauges. As a check of the calibration, the measurement was repeated for Kr, and there was good agreement with the gauge documentation. Fig. 2.3 shows the calibration curve for Xe. The two distinct lines are the measurements from the two mechanical gauges which gave readings over different pressure ranges.

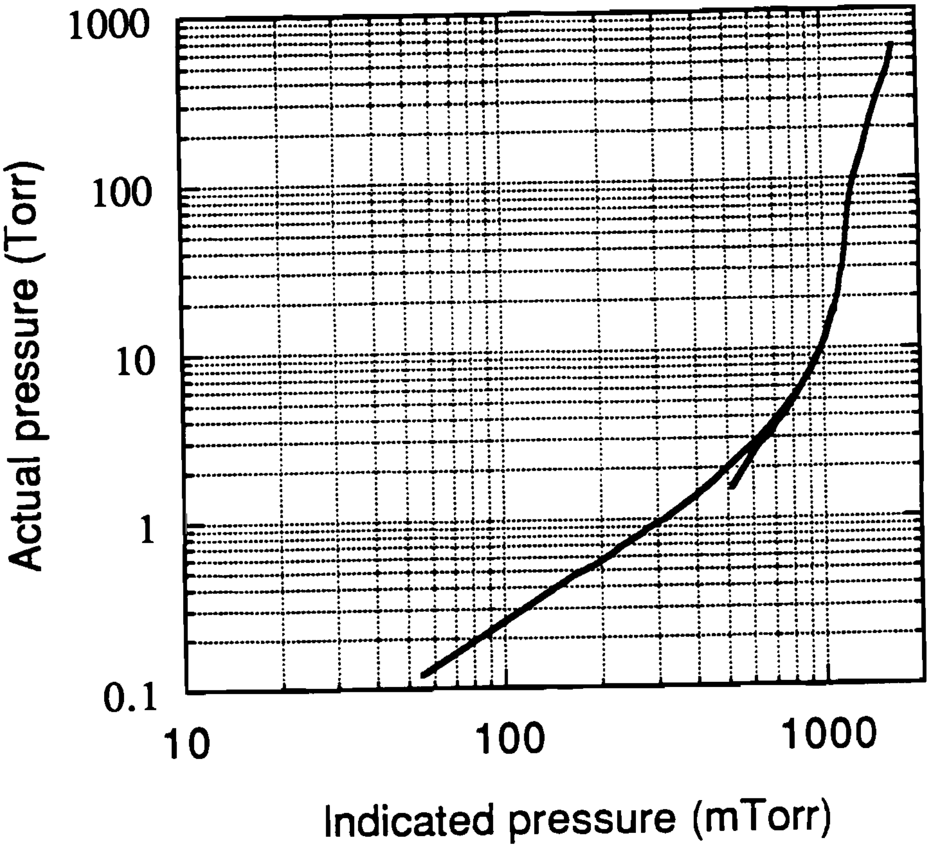

Fig. 2.3 Convectron gauge calibration curve for Xe. The two lines visible were produced from separate gauges which operated in different pressure ranges.

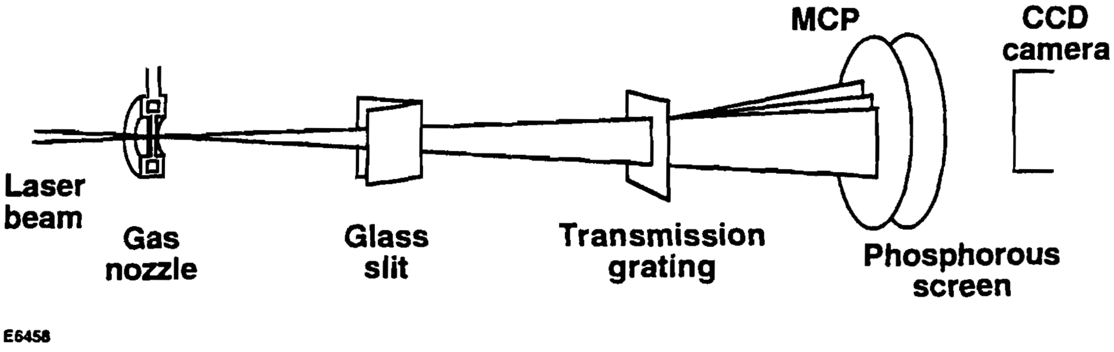
MCP
CCD camera
Laser beam
Gas nozzle
Glass slit
Transmission grating
Phosphorous screen
E6458

Fig. 2.4 Schematic of the experimental setup, including the gas target and the angularly resolved spectrometer.

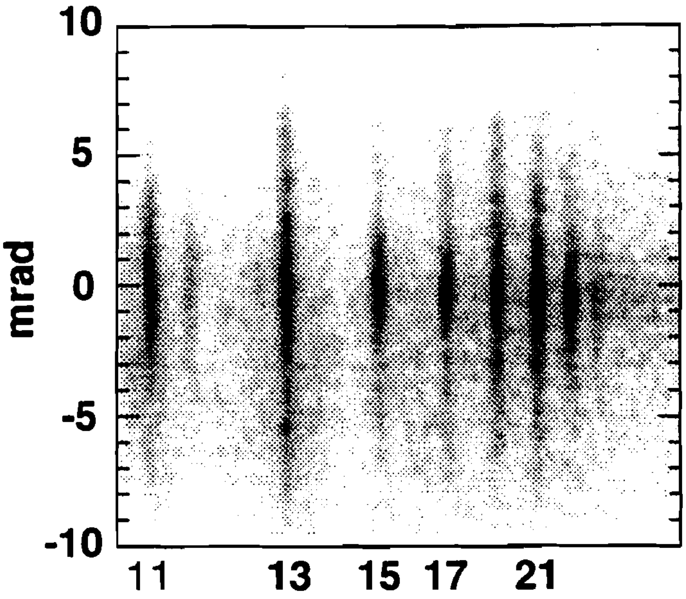

Fig. 2.5 High harmonics generated in Xe as captured by the CCD camera on the detector screen. Twenty images were averaged together to produce this picture.

2.1.B Spectrometer Design and Alignment

The harmonics produced in the gas target emerge collinear with the laser beam. The harmonics must be spectrally resolved without the incident laser pulse damaging the spectrometer. Fig. 2.4 shows a schematic of the spectrometer. Augst et al.[1] were the first to use this basic spectrometer design to see high-harmonic far-field profiles. In our current setup, a slit is positioned approximately 30cm behind the gas target, sampling a 1-dimensional cut through the center of the laser beam (and harmonic beams). After the slit, the light passes through a gold transmission grating (either 1μm or 0.2μm spacing). The grating lines are oriented parallel to the slit so that in the 1st-order diffraction the individual harmonics are resolved after propagating a short distance. The harmonics are detected by a micro-channel plate coupled to a phosphor screen (Galileo model 8081). The microchannel plate is not UV enhanced so it cannot detect harmonics lower than the ninth (177nm). Each harmonic appears on the detector as a distinct line which reveals the harmonic angular distribution along its length. The relative energies of the different harmonic orders can also be seen. The images are recorded electronically with a CCD camera. Fig. 2.5 shows an average of twenty harmonic images generated with Xe. The different harmonic orders are separated in the horizontal direction, and their angular profiles are shown in the vertical direction. For this picture, the 0.2μm grating was used in the spectrometer.

The slit is made from two pieces of uncoated glass held at an acute angle to reduce the laser intensity on the surfaces. Glass is used rather than metal because it has a higher damage threshold. The slit can be made narrow enough to cause the laser to strongly diffract, thereby reducing the energy density on the grating. This can be done without introducing significant diffraction to the high harmonics because they have much shorter wavelengths. Of critical concern is the energy density of laser light on the gold transmission grating. The slit width and the separation between the slit and grating must be chosen to keep the energy density below approximately 50 mJ/cm^2 on the grating surface. Depending on the needs of the experiment, the slit width was varied in the range from 100μm to 500μm.

The detector is aligned one component at a time. To aid in alignment, a He-Ne laser simulates the laser path, and the mirrors immediately preceding the chamber are adjusted until the beam enters the lens on axis. This is accomplished when the reflections from both surfaces of the lens return along the path of the incoming laser. At the other end of the chamber, the He-Ne beam is checked to see that it hits the desired location on the micro-channel plate, before the grating and slit are installed, and while the gas target is out of the beam path. The place where the He-Ne beam hits is where the zeroth-order grating line will be located when the slit and grating are later installed. The zeroth-order line was often positioned off center to allow for more detection area on the microchannel plate. If the He-Ne beam does not hit in the desired position, appropriate adjustments are made to the position of the tube holding the lens, and the process is repeated beginning with realignment of the beam to the lens. Once the tube and the beam are positioned correctly, the slit is placed in the beam followed by the grating. The directions of the slit and the grating lines are oriented parallel to each other.

2.1.C Spectrometer Resolution

The slit width and grating position determine which harmonics appear with appropriate resolution on the detector screen. A narrower slit gives better harmonic spectral resolution by making the lines thinner at the detector. At the same time, a narrow slit can significantly diffract the laser, thereby reducing the intensity on the grating. This can occur without significant broadening of the harmonic lines because of the large difference in wavelengths between the laser and the high harmonics ($q \geq 11$).

The laser reaches the Fraunhofer diffraction zone for the slit at a much shorter distance than do the harmonics. The distance to the Fraunhofer diffraction zone[3] is approximately qa^2/λ, where q is the harmonic order and a is the slit width. For a 200μm slit, the Fraunhofer diffraction begins to occur for the laser (λ=1054nm) at a distance of about 4cm, but for the 11th harmonic, the diffraction does not begin until about 40cm. The distance is even longer for higher harmonic orders. The distance between the slit and the detector is typically about 30cm, so the harmonics do not significantly diffract and can be thought of as being clipped by the edges of the slit in the sense of a projection. Thus, the width in the dispersion direction of all of the high harmonic lines at the detector is approximately d_1a/d_2, where d_1 is the distance from interaction region (laser focus) to the slit, and d_2 is the distance from the slit to the microchannel plate. The grating does little to alter the widths of the harmonic lines but only redirects their propagation.

The width of the laser light when it reaches the grating is given approximately by the width of the central peak of the Fraunhofer diffraction pattern from a slit.[3] This width is approximately $2d\lambda/a$, where d is the distance from the slit to the grating. The laser intensity on the grating decreases by the factor $2d\lambda/a^2$ compared to the intensity with the slit removed. For d=20cm and a=200μm, the intensity is reduced by a factor of 10. This simple estimate was checked by measuring the intensity at the grating position with and without the slit using a CCD camera. The measurement agreed with the estimate to within a factor of 2. This method enables higher laser intensities while protecting the grating against damage. Without the intensity-reducing effect of the slit, the energy density on the grating positioned 50cm after the laser focus would be 100 mJ/cm^2 when the peak laser intensity in the focus is 10^{14} W/cm^2. With the slit in place, it is possible to achieve intensities of a few times 10^{14} W/cm^2, without exceeding the 50 mJ/cm^2 limit on the grating.

The distance between the grating and the microchannel plate is chosen to bring onto the detector screen whichever harmonics are desired to be seen. The spacing on the detector surface between the first-order diffraction lines and the zeroth-order line is given by

$$\ell_q = x \tan\left[\sin^{-1}\frac{\lambda}{qh}\right] \qquad (2.1.1)$$

where x is the distance from the grating to the microchannel plate, and h is the periodic spacing of the grating structure. The higher the value of q, the closer the harmonic line appears to the zeroth-order line. For the higher harmonic orders, the arcsine and tangent can often be approximated by their arguments, so the spacing between two consecutive harmonic lines is approximately $\ell_q - \ell_{q+2} \cong 2x\lambda/hq^2$. If this value becomes less than the width of the harmonic lines, the harmonics will no longer be resolved.

The second-order diffraction lines of the higher harmonics fortunately do not overlap the first-order diffraction lines of the lower harmonics, so this is not an issue. In Fig. 2.5, the faint line which appears to the side of the 11th harmonic is the second-order diffraction of the 23rd harmonic. In some of the images that are shown in this thesis, the second-order diffraction lines appear even brighter than some of the near-by lower-order harmonic lines and should not be confused with them.

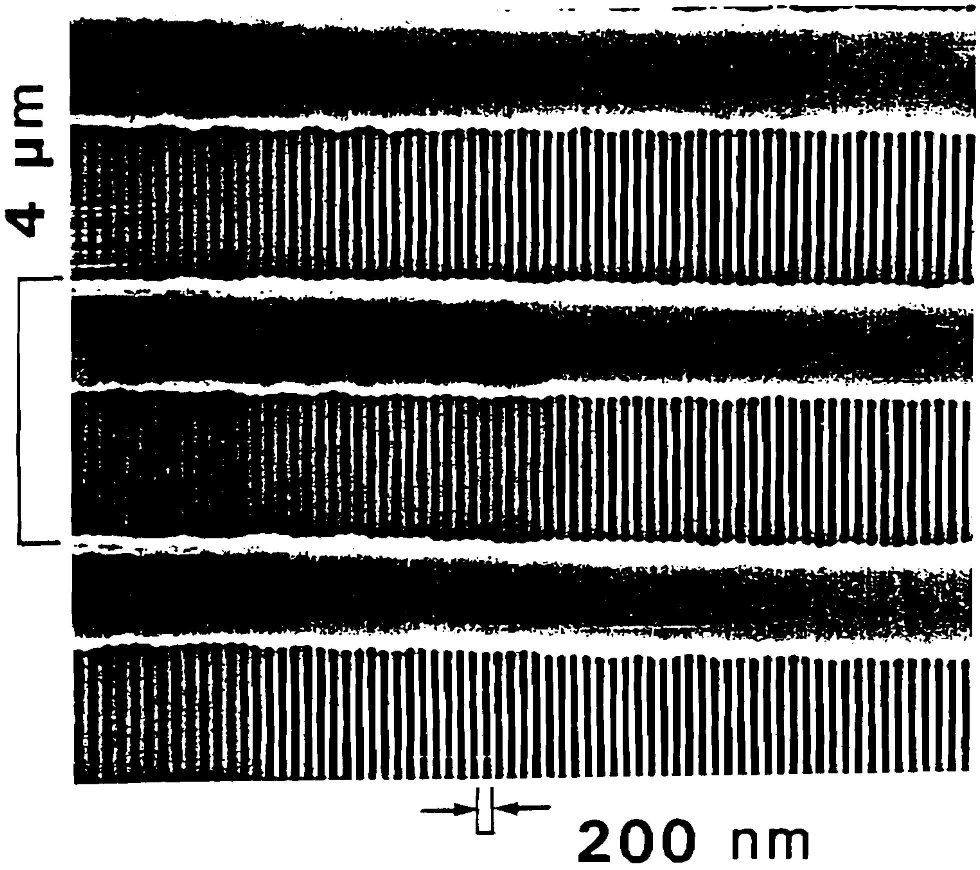

Fig. 2.6 Electron micrograph of the 0.2µm-period, 0.5mm-thick free standing gold grating. The perpendicular 4µm grating substructure is apparent. [Ref. 3]

2.1.D Detector Dynamic Range

The spectrometer is not absolutely calibrated so that only relative levels of harmonic emission can be measured. The dynamic range (not the gain) of the detector is only about one order of magnitude, so care must be taken to know at what point it begins to saturate. The dynamic range was checked by taking advantage of a 4μm periodic substructure which runs perpendicular to the lines on our 0.2μm transmission grating. (The 1μm grating has no periodic substructure.) Fig. 2.6 shows an electron microscope image of the 0.2μm grating.[3] The 4μm grating substructure is apparent. The additional lines form a grating which causes weak ghost images to appear superimposed but slightly off center along the slit direction for each harmonic. In Fig. 2.5 the ghosts caused the central peaks to appear one to two milliradians wider than they might otherwise. Rotating the transmission grating so that the 0.2μm lines are skewed relative to the slit causes the ghost images to appear distinctly outside of the main harmonic lines. Since the ratio between the energy in the ghost images to the energy in the main harmonic images is fixed, this ratio can be monitored as a function of detector illumination to determine at what point the detector saturates. Because of this investigation, it is known that the central peaks in Fig. 2.5 are significantly saturated.

The small dynamic range of the detector used in these experiments is one of the more serious limiting factors in this work. Many of the images shown in this thesis have portions of them which are significantly saturated. This was done purposefully to enable the weaker portions of the harmonic images to be seen. As the harmonic data is presented in Chapter 4, it will be pointed out which portions are saturated.

The relative amount of light that goes into a grating's first-order diffraction is independent of wavelength provided the gaps between the grating wires are much larger than the wavelength.[2] For harmonic orders below the mid twenties ($\lambda_q \geq 50\text{nm}$), this condition is not well satisfied for the 0.2μm grating. When the light wavelength is about the same as the grating wire gaps, the gaps function as wave guides in some complicated fashion, creating a wavelength dependence to the amount of light diffracted. This effect caused the lower-order harmonics in Fig. 2.5 to appear weaker than they actually should. A comparison between harmonic data taken with the 1μm and 0.2μm gratings reveals that our 0.2μm grating attenuates the 11th harmonic signal relative to the highest ones by about a factor of 4. This attenuation gradually decreases with increasing harmonic order until harmonic orders in the mid twenties, after which the relative efficiency is roughly constant.

The fact that the 0.2μm grating attenuates the lower harmonics is sometimes advantageous because it allows a larger number of harmonics to be seen simultaneously within the dynamic range of the detector. Another reason for using the 0.2μm grating is that our 1μm grating has many defects which scatter the light, obscuring the higher harmonics in noise.

2.1.E Tradeoffs in the Detector Configuration

The spectrometer was configured in a variety of ways to obtain the different harmonic far-field images presented in this thesis. The detector setup was chosen in each case to reveal a specific feature of the far-field pattern. Not all features could be accurately seen simultaneously. As pointed out previously, it is important to avoid saturation of the microchannel plate in order to get an accurate representation of the far-field harmonic angular profile. The linearity of the response is best when the harmonic signal is weak so that only a small fraction of the microchannels are depleted. On the other hand, enough of the channels must respond to achieve a clear signal. One way to improve the harmonic signal detection is to configure the spectrometer so that each harmonic line illuminates a wider strip on the detector. This increases the number of microchannels involved in detecting each harmonic, thus improving the statistics when a lesser fraction of the channels are depleted. The disadvantage is the sacrifice in resolution; only a few harmonics can be distinguished at a time.

With a wide slit in place, the grating must be positioned a greater distance behind the slit to avoid damage by the laser beam. Because the harmonic beams are continually expanding, a larger grating area is required to avoid clipping the light. The 1μm grating (2cm clear aperture) was best suited for this kind of measurement. The spectrometer was aligned using a 500μm slit and the 1μm grating was positioned 35cm behind the slit. The microchannel plate was placed an additional 30cm behind the grating. At the detector, the harmonic lines were approximately 1.5mm wide. Fig. 2.7 shows an image of the harmonics produced in Xe taken with this detector setup. The purpose of the measurement was to obtain an accurate representation of both the bright and dim parts of the far-field patterns without saturation on a single shot.

The 0.2μm grating was better suited than the 1μm grating to simultaneously measure a large number of harmonics. The 0.2μm grating was also better able to observe harmonic orders in the mid twenties and higher because of the high-quality of the grating structure. The smaller clear aperture (1.2cm) of the 0.2μm grating required the grating to be positioned no further than 50cm from the focus to avoid clipping the harmonic light. The microchannel plate was positioned between 5cm and 7cm behind the grating depending on the required harmonic spectral range. The slit had to be set at approximately 200μm or less to reduce the laser intensity on the grating. This made the thickness of harmonic lines at the detector about 300μm. The narrower harmonic lines made it difficult to see the dim portions of the harmonic profiles without the bright portions saturating the detector.

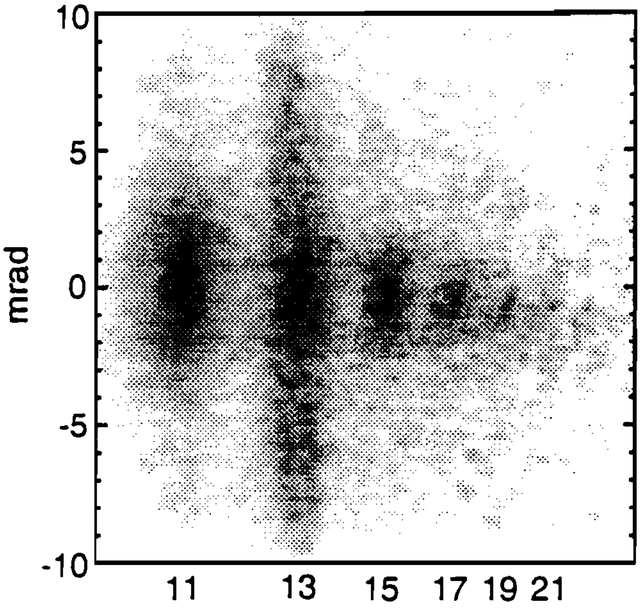

Fig. 2.7 An average of five harmonic images produced in 0.5 Torr Xe at 9×10^{13} W/cm^2. The spectrometer used a 500µm slit and a 1µm grating.

2.2 LASER CHARACTERISTICS

The experiments presented in this thesis benefitted from an extensive upgrade to the laser system which increased the firing repetition rate and improved the focusing characteristics of the beam. The path layout of the laser was re-configured, and many components of the system were changed or reconstructed. The energy capability of the system was also significantly increased. Our experiments, however, did not take advantage of this increase.

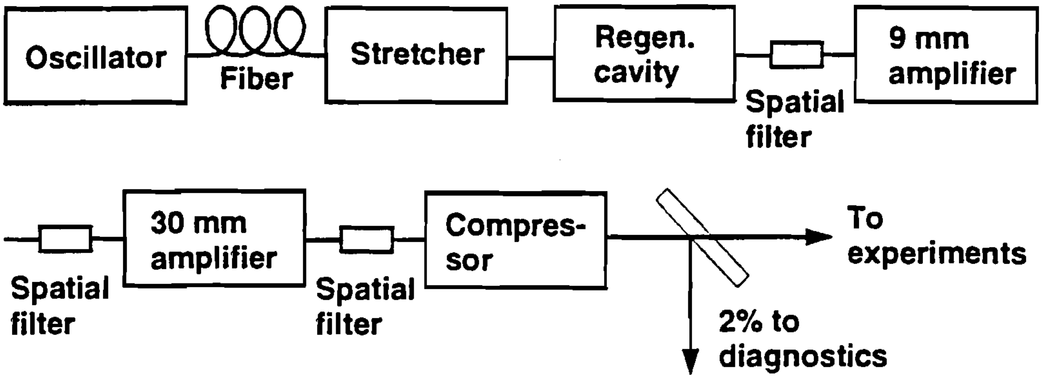
Oscillator
Fiber
Stretcher
Regen. cavity
Spatial filter
9 mm amplifier
Spatial filter
30 mm amplifier
Spatial filter
Compres-sor
To experiments
2% to diagnostics

Fig. 2.8 Schematic of the chirped-pulse-amplification laser system.

2.2.A Laser System

The laser is a neodymium glass system which operates on the principle of chirped-pulse amplification.[4] The system, which temporally compresses the pulse to a picosecond after amplification, can achieve peak powers of about a terawatt. The laser has been well characterized and is described in the literature.[4,5] Fig. 2.8 shows a schematic of the principle stages of the laser system.

The laser beam originates in an actively mode-locked YLF oscillator cavity which produces a train of band-width-limited pulses separated by 10ns. The wavelength is 1054nm, and the pulses are 50ps in duration with about 1nJ of energy. The pulse train goes through a 1km glass fiber which increases the bandwidth from about 0.3Å to 35Å through self-phase-modulation. The pulses are then temporally stretched to 500ps by a pair of gratings, which gives a linear chirp to the pulses. A single pulse is selected and injected into a Q-switched regenerative amplifier cavity. After about 70 round trips in the cavity, a 0.3 mJ pulse is selected from the beam which emerges through an 80% cavity end mirror. Gain narrowing in the cavity reduces the 35Å quasi-square spectral profile of the seed pulse to a gaussian with full-width-at-half-maximum 16Å, the bandwidth required for a 1ps pulse. The beam emerging from the regenerative amplifier has a diffraction-limited gaussian profile with a diameter of 2.0mm (defined by where the intensity falls to $1/e^2$ of the peak). To this point, the laser system remains relatively unchanged from previous descriptions.[5] Further amplification of the beam does not significantly effect its spectral and temporal characteristics. However, care must be taken to preserve the focusing characteristics as the beam must pass through and reflect from many optical components before reaching the end of its path. To help preserve the focusing quality, the beam goes through four different spatial filters as it is several times up-collimated and twice amplified.

After the regenerative amplifier, the beam goes through a 200cm air spatial filter with a magnification of 3. The pinhole diameter is 600μm. The emerging 6.0mm diameter beam enters the 9mm-diameter amplifier system which passes the laser pulse through the amplifier rod three times for a total gain of 150. Fig. 2.9 shows a schematic of the 9mm amplification system. An important feature is the 90cm, 1:1 spatial filter between the second and third passes through the amplifier rod. This allows the diffraction caused by the rod to be removed before its final amplification. Another important feature of the amplification system is the manner in which the Pockel cell is switched. Rather than switching after amplification, the cell is switched before. If the cell fails to switch, the pulse is unable to enter the amplification system in the first place. This scheme protects the regenerative amplifier from the energy produced in the 9mm amplifier. Energy cannot return down the system in the event that the Pockel cell does not switch or only partially switches. Another advantage of this setup is that the laser pulse does not go through the Pockel cell after the last trip through the amplifier rod. This is advantageous because the Pockel cell has a lower damage threshold than most optical components and is relatively expensive. One disadvantage to the system is caused by the limited contrast typical of the coatings for Brewster's-angle polarizers. This gives a pre-pulse from the exiting polarizer which is only a factor of 10^2 smaller in energy than the main pulse. However, since the prepulse comes out after the second pass through the amplifier, the main pulse which comes out after the third pass can be made to have a slightly different direction. Thus, the subsequent spatial filter is able to block the prepulse completely.

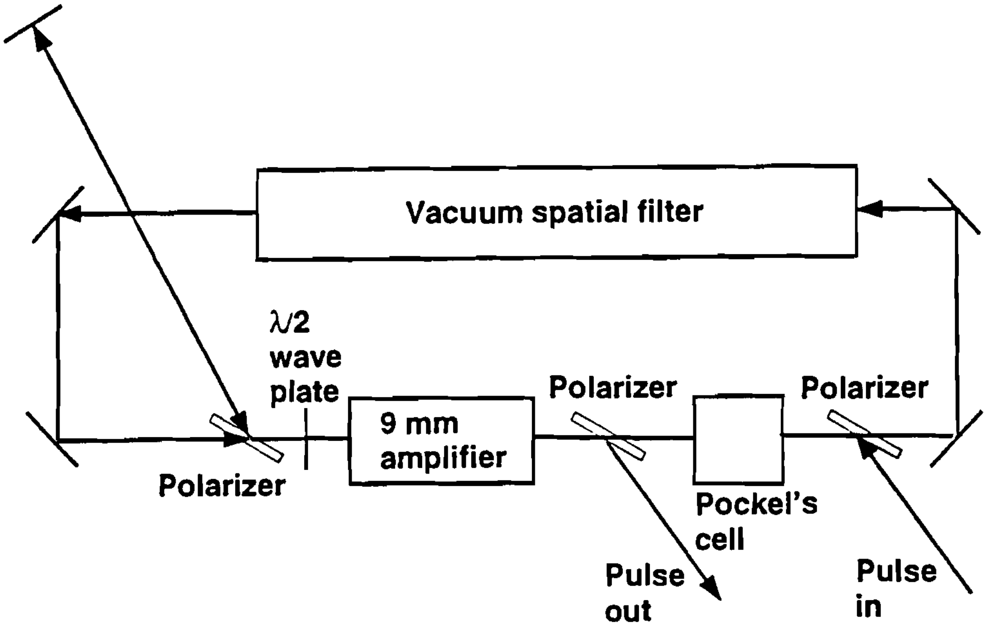
Vacuum spatial filter
λ/2
wave
plate
9 mm
amplifier
Polarizer
Polarizer
Polarizer
Pockel's
cell
Pulse
out
Pulse
in

Fig. 2.9 Schematic of the 9mm amplification system. The pulse enters the system by reflecting off the first polarizer and transmitting through the second one, the polarization being rotated by the Pockel cell. Before the pulse returns to the Pockel cell, the voltage on the cell goes to zero so that it has no effect. The pulse is spatial filtered between the second and the final pass through the amplifier.

Further expansion and amplification of the beam is straightforward. It consists of two more vacuum spatial filters with a 30mm amplifier in between. The first spatial filter has a length of 160cm with a magnification of 3 so that the emerging beam has a diameter of 1.8cm. The pinhole diameter is 200μm. The amplifier can produce a gain of up to 30, after which the beam goes through the last spatial filter. This spatial filter has a length of 275cm and a magnification of 1.2. The pinhole diameter is 200μm. At this point, depending on the energy of the beam and the desired focusing conditions, the beam can be sent either through or around a galilean up-collimator with magnification 8/3. Finally the chirped pulse is temporally compressed to 1ps duration on gold holographic gratings (1740 lines per mm). After the beam is compressed, it goes through a 1cm glass wedge which splits off 2% of the energy for diagnostics. The beam then goes off two alignment mirrors before being focused into the experimental chamber. The diagnostics consist of an energy monitor and an autocorrelator which can measure the pulse duration on every shot. The focusing length of the lens is 153cm, and depending on whether the beam goes around or through the galilean up-collimator, the resulting f-number is 70 or 25. For these experiments the f/70 setup was used exclusively.

2.2.B Focusing Characterization

Fig. 2.10 shows a scan of the f/70 laser focal spot which has been imaged with a magnification of 4 onto a CCD camera. The pictures are taken at various positions to show how the beam goes into and out of focus The diameter of the focal spot at the beam waist is approximately 1.25 times larger than the theoretical diffraction limit. Fig. 2.11 shows a comparison between the measured beam radius and the diffraction-limited radius of an f/70 beam. The radius of the beam was determined by integrating over the intensity to find the effective area and then by calculating the radius (to the $1/e^2$

intensity point) assuming a gaussian distribution. The confocal parameter of the focus as defined by the diffraction-limited curve is 13mm.

The peak intensity of a spatially and temporally gaussian laser pulse is given very nearly by $I_o=E/(A_{1/e}T_{fwhm})$ where E is the pulse energy, $A_{1/e}$ is the focal spot area inside the 1/e intensity contour, and T_{fwhm} is the full-width-at-half-maximum of the pulse duration. The energy of the pulse is measured on each shot by a photodiode connected to a charge-integrating device. The relative uncertainty in the energy measurements is about 10%, and the absolute uncertainty is about 20%. The pulse duration is monitored also on each shot using an auto-correlation technique. For most of the experiments, the pulse duration was about 1.4ps with a fluctuation of about 25%. The uncertainty in each measurement is about 25%. The focal-spot area is not measured every shot. However, when the area was measured, it was observed that it fluctuated very little from shot to shot (≤4%). The measured focal area for the beam used in the experiments was about 5500μm^2 with an uncertainty of about 10%. Together, the different uncertainties give an absolute uncertainty for the laser intensity of about 35% and a relative uncertainty of about 25%.

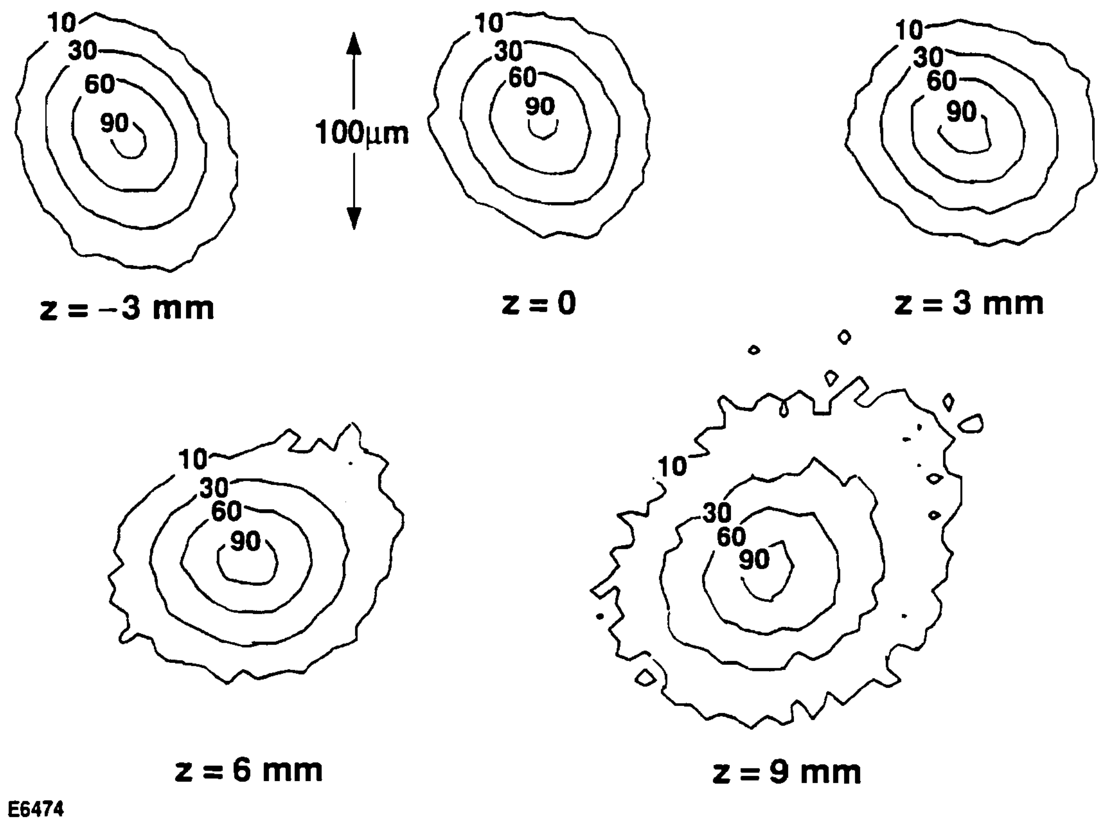

Fig. 2.10 The laser distribution for various positions in front and behind the focus. The pictures were taken by imaging the laser focus with a magnification of 4 into a CCD camera.

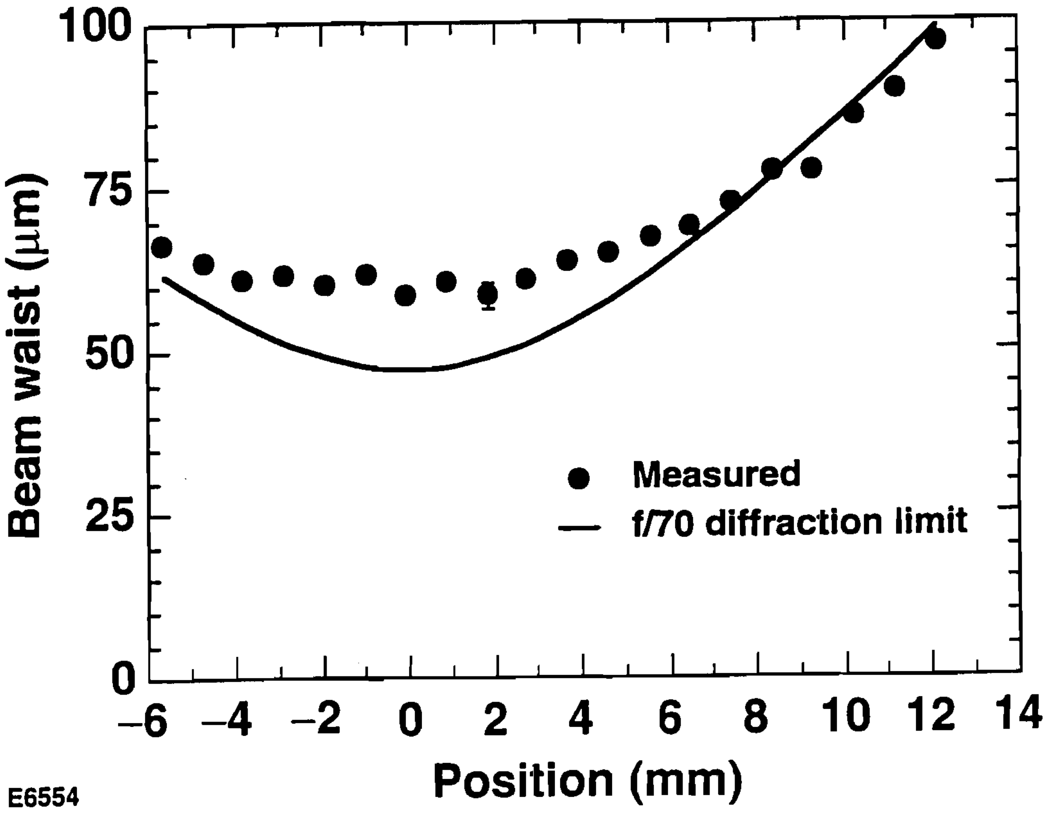

Fig. 2.11 Plot of the measured laser beam waist as a function of axial position along the focus, showing that the beam is 1.25 times diffraction limited with f/70 optics. The solid line shows the theoretical diffraction limit.

2.3 REFRACTION OF THE LASER BY FREE ELECTRONS

A laser propagating through an ionized medium can undergo refraction due to the radial profile of the free electron density.[6,7] To determine under what conditions ionization in the laser focus significantly alters the beam, the laser was focused through the gas target and imaged onto a CCD camera with various xenon gas pressures and with various peak laser intensities. The target was positioned at the laser focus. Fig. 2.12 shows a schematic of the setup. This is essentially the same setup used to measure the focus [see Figs.2.10 and 2.11]. Fig. 2.13, first row, shows the imaged focal spot as a function of laser intensity where the gas pressure is 0.6 Torr. At the highest intensity the xenon is 2 and maybe 3-times ionized at the center of the focus. At this low pressure, the imaged focal spot is virtually identical to that observed with no gas, independent of the laser intensity. When the pressure is increased to 3 Torr as in the second row of Fig. 2.13, a decrease in the imaged focal area is observed as the laser intensity increases. This is due to refraction which increases the cone angle of the laser as it leaves the gas target. The larger emerging beam images to a smaller spot. Fig. 2.14 shows a scan of the imaged focal spot radius for two gas pressures and intensities. As the beam refracts more, the imaged focus not only gets smaller but also moves toward the imaging lens. Because the imaged focus moves toward the imaging lens shows that the effect is due to free electrons and not to self focusing in the neutral gas. Such a significant change in the laser beam path indicates that the basic phase-matching assumption, that the laser is unaffected in the medium, cannot be used. To avoid this complication, the experiments presented in this thesis were performed under conditions where refraction does not occur. This is in contrast with other experiments which have measured high harmonics in a regime where strong laser refraction can occur.[1,8-17]

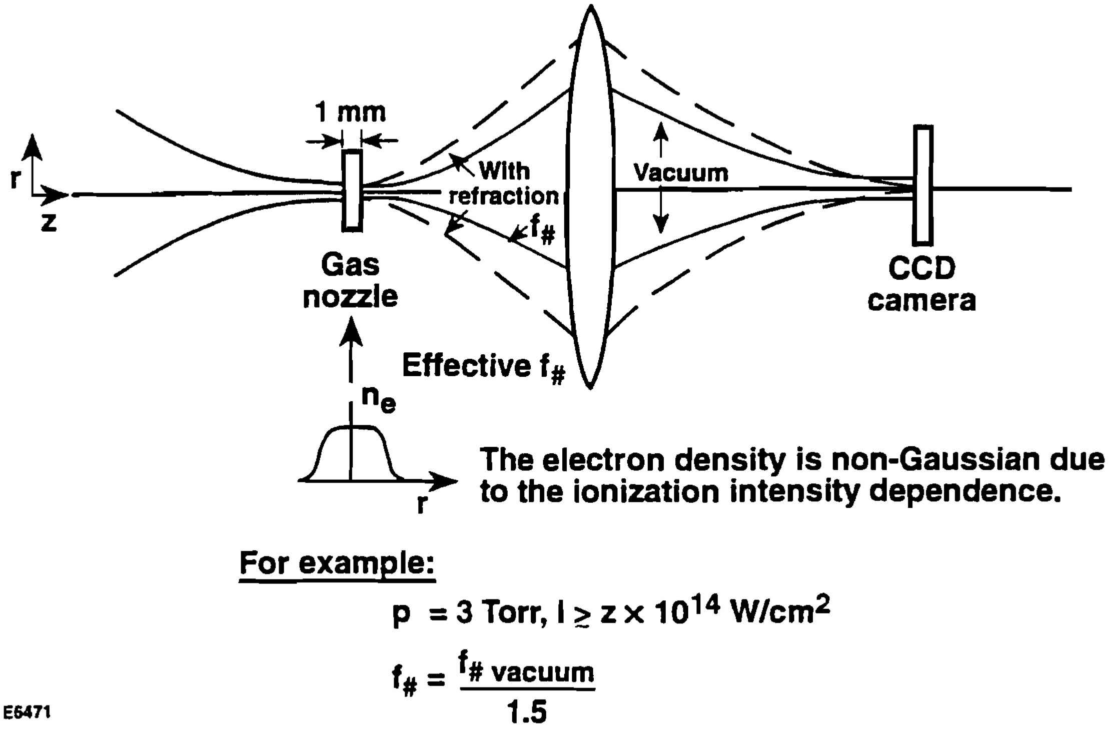
r
z
1 mm
Gas
nozzle
With
refraction
f#
Effective f#
Vacuum
CCD
camera
ne
r
The electron density is non-Gaussian due
to the ionization intensity dependence.
For example:
p = 3 Torr, I ≥ z x 10^14 W/cm^2
f# = f# vacuum / 1.5
E6471

Fig. 2.12 A schematic depicting the imaging technique used to study defocusing from free electrons. The imaged spot gets smaller.when the beam undergoes refraction at the origin.

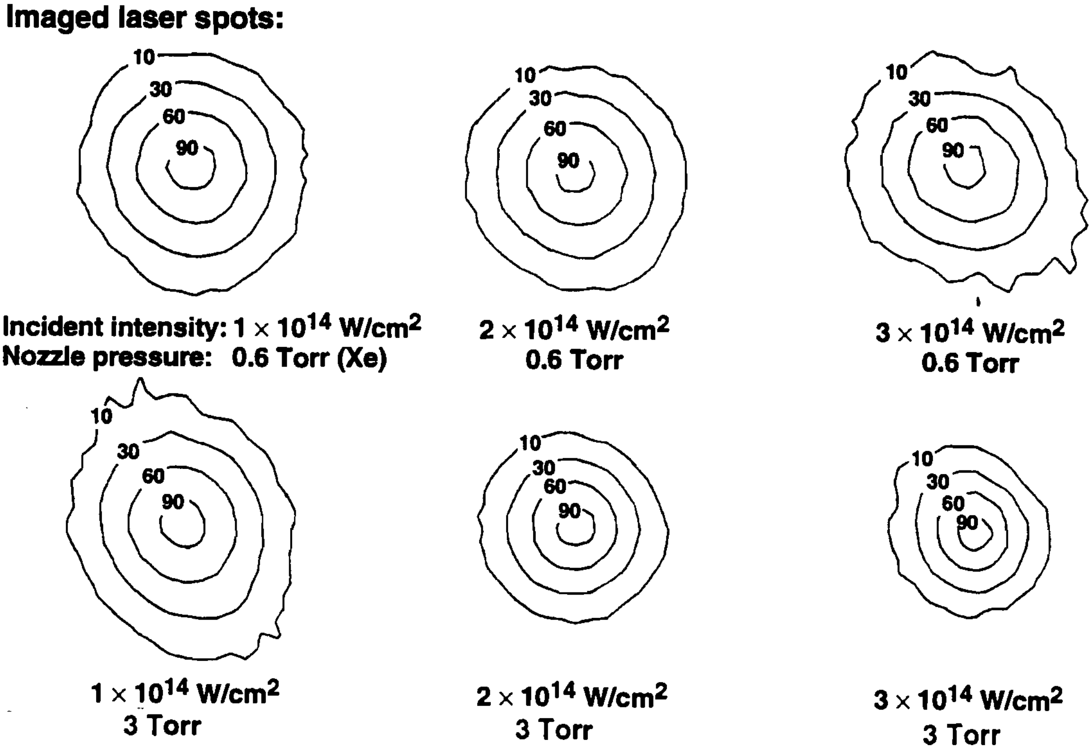
Imaged laser spots:

Incident intensity: 1 × 10^{14} W/cm^2
Nozzle pressure: 0.6 Torr (Xe)

2 × 10^{14} W/cm^2
0.6 Torr

3 × 10^{14} W/cm^2
0.6 Torr

1 × 10^{14} W/cm^2
3 Torr

2 × 10^{14} W/cm^2
3 Torr

3 × 10^{14} W/cm^2
3 Torr

Fig. 2.13 The imaged laser focus as a function of intensity and gas target pressure. The first row shows images with 0.6 Torr of Xe in the target, and the second row shows the same scan for approximately 3 Torr. The gas target is positioned at the laser focus.

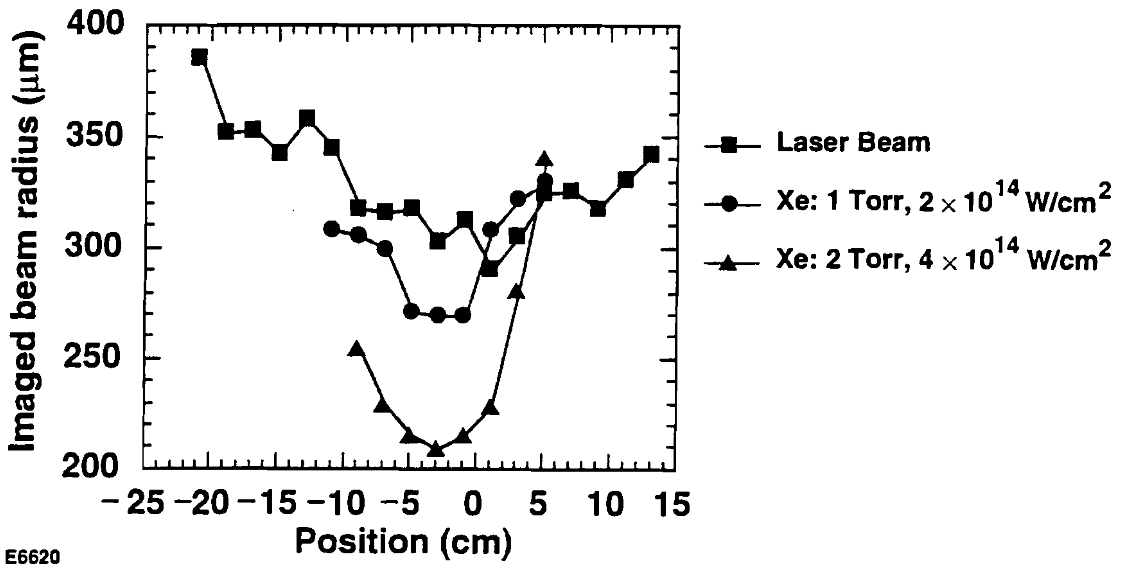

Fig. 2.14 A scan of the imaged laser focal spot radius for several gas pressures and intensities. The horizontal axis refers to the position along the beam axis of the camera relative to the imaged focus. Refraction from free electrons causes the imaged focus to grow smaller and to shift toward the imaging lens. The gas target is positioned at the laser focus.

A simple estimate of the refraction is consistent with the results observed above. If the altered beam emerging from the gas target is assumed to follow a gaussian profile, the effective f-number of the emerging beam can be related to the on-axis electron density in the target. This simplification neglects the temporally-dependent appearance of the free electrons. It also implies that the electron distribution in the focus acts as a perfect thin lens. Depending on the laser intensity, the gas density, and the position of the gas target relative to the laser focus, the effective f-number of the emerging beam can increase or decrease relative to the initial beam. If the gas distribution is very thin, the position of the gas target relative to the exiting beam's focus, whether virtual or real, is given approximately by

$$\frac{z'}{z'_0} = \frac{z}{z_0} + \Delta k\ell \qquad (2.3.1)$$

where z_0 and z'_0 are the Rayleigh ranges of the incoming and exiting beams respectively, and z and z' are the target positions relative to the incoming and exiting beam focuses.

$\Delta k\ell$ is the on-axis phase mismatch caused by the free electrons. Its value is given by $k\ell(1-n)$ where n is the optical index of refraction in the free electrons, and ℓ is the gas target thickness. The optical index of refraction is given by

$$n = \sqrt{1 - \frac{\omega_p^2}{\omega^2}} \qquad (2.3.2)$$

where $\omega_p^2 = e^2 N_0 / \varepsilon_0 m_e$ is the plasma frequency and ω is the laser frequency. It follows for a low-density singly-ionized ideal gas that the index of refraction is

$$n-1 \cong -\frac{e^2 P\lambda^2}{8\pi^2 \varepsilon_o c^2 m_e (kT)} \tag{2.3.3}$$

where P is the pressure of the medium. For λ=1054nm, T=300°K, and P=1 Torr, Eq. (2.3.3) gives n-1=-1.6x10^{-5}. k is Boltzman's constant.

The magnification of the divergence of the exiting beam relative to the incoming beam is defined by

$$M^2 = \frac{1+(z'/z'_o)^2}{1+(z/z_o)^2}. \tag{2.3.4}$$

z_0' is found to be equal to z_0/M^2.

For the approximate conditions of of the upper right picture in Fig. 2.13 (0.6 Torr, 3 ionized electrons per atom, ℓ=1mm, z=0), Eqs. (2.3.1) and (2.3.3) give $z'/z'_0=\Delta k\ell=0.2$. From Eq. (2.3.4), the magnification in diameter of the exiting beam is $\sqrt{1.04}$ which is negligible. This is in agreement with the picture which shows no change to the beam. For the pressure and intensity used to obtain the lower right picture in Fig. 2.13 and also the lower curve seen in Fig. 2.14, $\Delta k\ell$ approaches unity, giving a beam cone magnification near $\sqrt{2}$. This reduces the imaged focal spot radius by near a factor of $\sqrt{2}$ as observed.

REFERENCES

1. S. Augst, C. I. Moore, J. Peatross, and D. D. Meyerhofer, "Spatial Distribution of High-Order Harmonics Generated in the Tunneling Regime," in *Short Wavelength Coherent Radiation: Generation and Applications*, edited by P. H. Bucksbaum and N. M. Ceglio, (OSA, Monterey, CA, 1991), Vol. 11, pp. 23-27.
2. E. Hecht, *Optics*, 2nd ed. (Addison-Wesley, Reading, Massachusetts, 1987), pp. 397-412.
3. M. L. Schattenburg, E. H. Anderson, and H. I. Smith, "X-Ray/VUV Transmission Gratings for Astrophysical and Laboratory Applications," Physica Scripta. **41**, 13-20 (1990).
4. P. Maine, D. Strickland, P. Bado, M. Pessot, and G. Mourou," Generation of Ultrahigh Peak Power Pulses by Chirped Pulse Amplification," IEEE J. Quantum Electron. **QE-24**, 398 (1988).
5. Y.-H. Chuang, D.D. Meyerhofer, S. Augst, H. Chen, J. Peatross, and S. Uchida, "Pedestal Suppression in a Chirped Pulse Amplification Laser," J. Opt. Soc. Am. B **8**, 1226-1235 (1991).
6. S. C. Rae, "Ionization-Induced Defocusing of Intense Laser Pulses in High-Pressure Gases," Opt. Comm. **97**, 25-28 (1993).
7. X. D. Cao, J. Peatross, and D. D. Meyerhofer, "Defocusing of a laser in a Thin Gas Target," in preparation (1993).
8. R. A. Smith, J. W. G. Tisch, M. Ciarrocca, S. Augst, and M. H. R. Hutchinson, "Recent Ultra-high Harmonic Generation Experiments with Picosecond Laser Pulses," to be published in the proceedings of the 3rd

Conference on Super Intense Laser-atom physics, (NATO, Han-sur-Lesse, Belgium, 1993).

9. N. Sarukura, K.Hata, T. Adachi, and R. Nodomi, "Coherent Soft X-Ray Generation by the Harmonics of an Ultra-High Power KrF Laser," Phys. Rev. A **43**, 1669-1672 (1991).

10. K. Kondo, N. Sarukura, K. Sajiki, and S. Watanabe, "High-Order Harmonic Generation by Ultrashort KrF and Ti:Sapphire Lasers," Phys. Rev. A **47**, R2480-R2483 (1993).

11. A. L'Huillier and Ph. Balcou, "High-Order Harmonic Generation in Rare Gases with a 1-ps 1053-nm Laser," Phys. Rev. Lett. **70**, 774-777 (1993).

12. L. A. Lompre, A. L'Huillier, M. Ferray, P. Monot, G. Mainfray, and C. Manus, "High-Order Harmonic Generation in Xenon: Intensity and Propagation Effects," J. Opt. Soc. Am. B **7**, 754-761 (1990).

13. A. L'Huillier, K. J. Schafer, and K. C. Kulander, "High-Order Harmonic Generation in Xenon at 1064nm: The Role of Phase Matching," Phys. Rev. Lett. **66**, 2200-2203 (1991).

14. Ph. Balcou and A. L'Huillier, "Phase-Matching Effects in Strong-Field Harmonic Generation," Phys. Rev. A **47**, 1447-1459 (1993).

15. A. L'Huillier, "Spatial and Temporal Coherence of the High Harmonics," Invited talk at the 6th International Conference on Multiphoton Processes, Quebec City, June 1993.

16. M. H. R. Hutchinson, "Studies of High-Harmonic Generation at High Laser Intensities," Invited talk at the 6th International Conference on Multiphoton Processes, Quebec City, June 1993.

17. Ph. Balcou, A. L'Huillier, P. Salieres, "High-Order Harmonic Generation in an Ionizing Medium," Invited talk at the 6th International Conference on Multiphoton Processes, Quebec City, June 1993.

CHAPTER 3

GAS TARGET

High-order harmonic-generation experiments traditionally have been carried out by focusing a laser into a jet of gas.[1-6] A gas jet relies on the principles of fluid flow to propel gas from its orifice in a thin stream, making a localized gas distribution which a laser can intersect. Lompré *et al.* measured the characteristics of such a gas jet.[6] They were able to produce a 1-mm gas distribution with a peak pressure of 25 Torr. A gas jet must operate at a sufficiently high pressure so as to ensure a narrow stream of flow. Typically the backing pressure of the jet is hundreds of Torr, while the usable region of the jet is of the order of tens of Torr. A lower pressure causes a more diffuse gas distribution in the plume, making the phase matching in the experiment more difficult. The density of the gas expelled from a jet varies as a function of distance from the orifice, the distribution becoming broader as the distance increases. This can make the systematic alignment of the intersection between the laser and the gas jet a difficult and tedious task.

A gas target was designed to create well-characterized, narrow gas distributions at low densities (1–2 Torr or less). This low-density regime is desirable to reduce the phase-matching effects during the harmonic generation. Also, the low backing pressure has the advantage of reducing the possibility of dimer formation in gases such as Xe.[6]

3.1 GAS TARGET DESIGN

The gas target, shown in Fig. 3.1 (a)-(c), consists of a small cylindrical hole through which the focused laser passes. Gas enters the cylindrical hole from the sides of the cylinder wall. Because the laser beam goes through the target, the alignment of the device is comparatively simple. The gas target operates on the principles of molecular flow rather than fluid flow as in the gas jet. Since the flow rate is low, the target can be operated in a continuous mode rather than pulsed. The density of the gas within the hole remains high while the gas outside the hole disperses quickly (it goes as the inverse square of the distance from the hole edge). The target operation is limited to low densities just as the gas jet is limited to high densities. If the gas in the target hole is at too high a pressure, plumes may develop out of its ends that would lie on top of the incoming and outgoing laser beam. The jet and the target are thus complementary in the sense that they operate in opposite ranges of pressure.

The gas distribution in the target is characterized experimentally. It is perhaps more difficult to characterize than the jet since the gas densities are much lower, and the off-axis line of sight to the interaction region is obstructed by the target itself. However, the gas density profile was measured in the region just inside the target opening and outward. There is good agreement between the measurement and a calculation of the gas distribution using a Monte-Carlo computer simulation of free molecular flow. The same calculation also predicts the gas flow rate from the target. The flow rate has been measured for two gas target designs. In both cases, there is good agreement between the predicted and the measured gas flow rates.

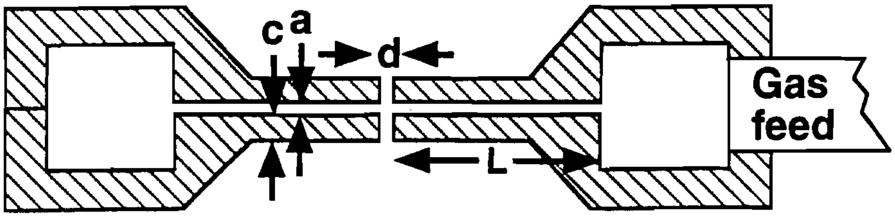

Fig. 3.1(a) A cutaway view of the two cylindrical gas target pieces that are glued together at their outer rims. Gas is fed into the outer ring-shaped pocket.

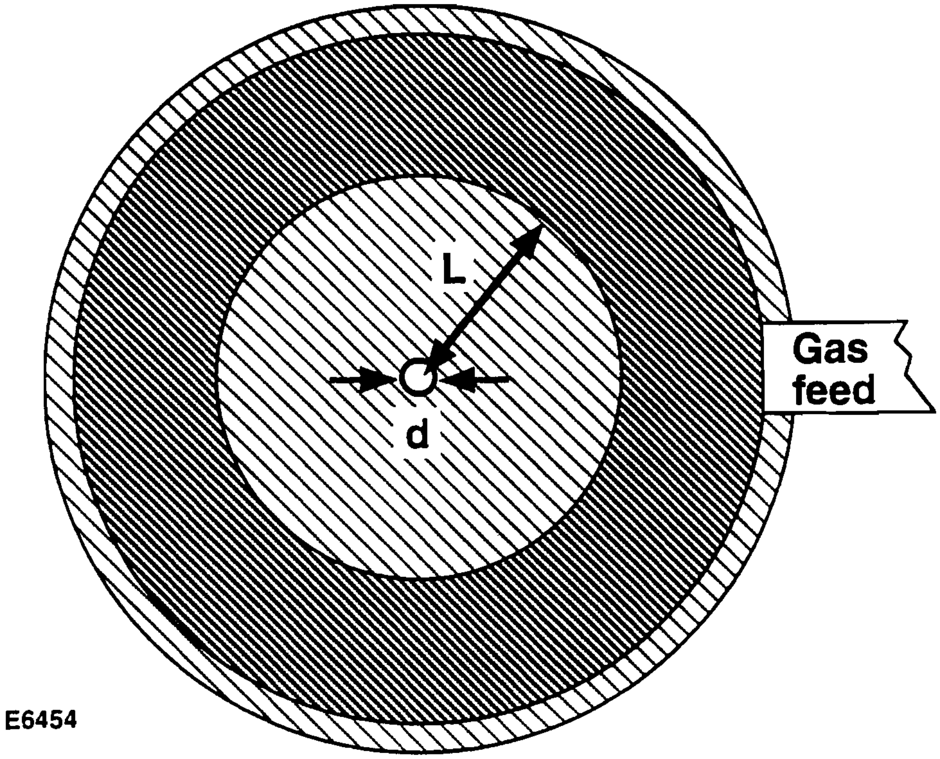

Fig. 3.1(b) An inside view of a single gas target piece that shows the ring-shaped pocket from which the gas flows across the thin plate toward the center hole.

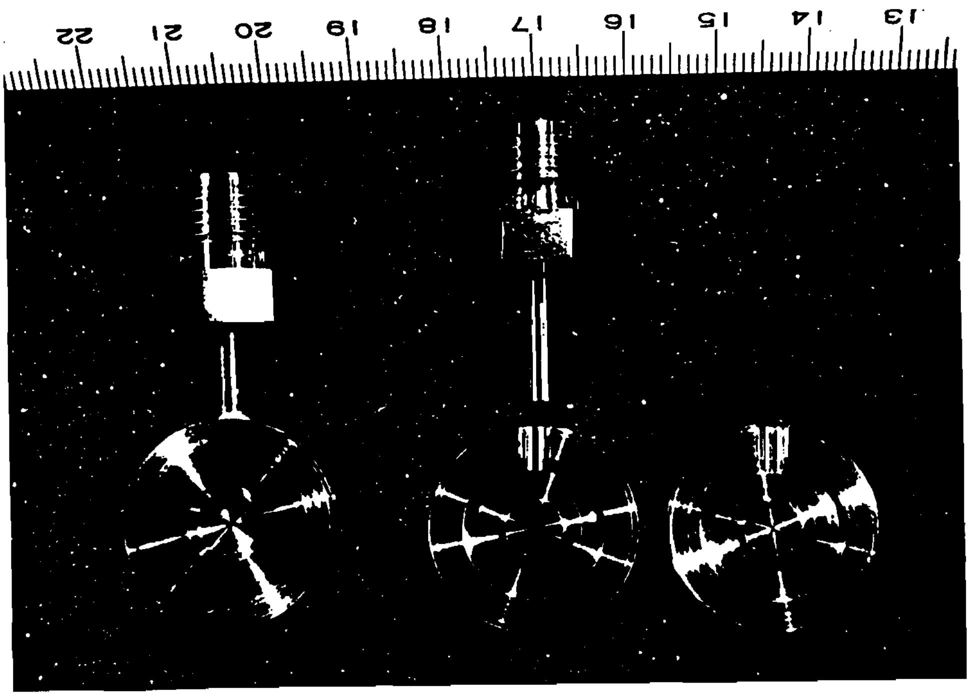
22
21
20
19
18
17
16
15
14
13

Fig. 3.1(c) A photograph of two gas targets. One has been glued together and the other is unassembled. The scale shown is in centimeters.

3.1.A Gas Target Dimensions

The gas target consists of two identically machined cylindrical aluminum pieces, which are glued together with a thin layer of vacuum epoxy. Aluminum is chosen because of its ease of machining. Fig. 3.1(a) shows a cut-away portion of the two pieces (upper and lower) which are already attached around the outer rim. Fig. 3.1(b) shows the inside of a single piece so that the cylindrical symmetry is observable. Fig. 3.1 (c) is a photograph of two gas targets; one has been glued together and the other is still in separate pieces. Gas flows from the outer ring-shaped pocket into the gap between the thinly spaced plates and toward the hole at the center. The gas then escapes out both ends of the hole. When gluing the pieces together, the drill bit that made the holes is inserted through both pieces to ensure alignment. As shown in the figures, a is the separation of the plates, c is the thickness of the plates, d is the hole diameter, and L is the length from the hole center to the inside edge of the outer gas pocket. Typical values for these are a = 0.2 mm, c = 0.4 mm, d = 0.5 mm, and L = 4 mm.

3.1.B Molecular Flow Range

A gas that flows within a boundary such as a pipe or some other confining shape is in the molecular flow range if the collisional mean free path of the particles is longer than the characteristic dimension of the boundary (such as a pipe diameter). Knudsen's number (Kn) is the ratio of a gas particle's collisional mean free path to a typical dimension of the boundary. Pure molecular flow begins when Kn > 1. This regime of gas flow is the best understood. The flow of gas in this range is completely determined by the geometry of the walls and can be calculated numerically using Monte-Carlo averaging techniques.[7,8] The standard assumption is that a gas particle travels in a straight path until encountering a wall where it is re-emitted at some new angle. Due to the molecular coarseness of almost any surface, the new direction of the particle has virtually no correlation to the incident direction. The distribution of the rebound is generally taken as the cosine to the surface normal. This assumption has been experimentally verified for various geometries.[7,8] The problem is usually treated in terms of throughput; that is, for a given system, how likely is a particle that enters one end of the system to emerge out of the other end.

Harmonic-generation experiments often use the noble gases. The room-temperature mean free paths of the lighter noble gases are 2 mm, 1 mm, 0.8 mm, 0.6 mm, and 0.4 mm for He, Ne, Ar, Kr, and Xe, respectively, at 0.1-Torr pressure.[8] For the purposes of this paper, these numbers should be compared with the typical dimension of the gas target center (0.5 mm). The mean free path scales inversely with pressure.

The fluid flow regime begins when $Kn < 0.01$. The flow of the gas in this range behaves very differently from molecular flow. In the fluid flow regime the intraparticle collisions rather than particle-wall collisions dominate the flow of the gas. The regime in between fluid and molecular flow is not well understood. In this case both types of collisions have importance. However, it is likely that much of the dispersive nature of molecular gas flow is preserved even with Kn as low as 0.1.

3.2 CALCULATION OF TRAJECTORIES IN A MONTE-CARLO SIMULATION

This section describes the details necessary for numerically simulating molecular flow through the target. The particles are assumed to move in straight lines between encounters with the target walls. Intraparticle collisions are ignored. Particles enter the region between the thinly spaced plates of the target from the ring-shaped gas pocket at a distance L from the center [refer to Fig. 3.1 (b) and (c) throughout this section]. When particles hit the target walls, they rebound in some new direction, and their trajectories are recorded. Each particle propagates until it either exits the target opening or returns to the ring-shaped gas pocket.

The various straight segments of a particle's trajectory are represented by equations of straight lines. The more natural coordinate system for straight lines is Cartesian, wherein the equations for a straight line in three dimensions can be written as $x = m_x z + b_x$ and $y = m_y z + b_y$. The azimuthal symmetry of the target also requires the use of cylindrical coordinates, which are obtained with the transformations $r = \sqrt{x^2 + y^2}$ and $\phi = \tan^{-1}(y/x)$, where $\phi \rightarrow \phi + \pi$ if $x < 0$. The z-axis is chosen to lie along the target axis of symmetry, and the origin is taken to be the target center. When the particle encounters the planar surface of the interior of one of the thinly spaced plates, the position of impact is found from $z' = \pm a/2$. The standard assumption at this point is that the particles leave the surface with a Lambertian distribution. This is the same distribution as produced by an ideal gas escaping from a small hole in a thin-walled container. Under the diffuse rebound assumption, the slopes for the new line emerging from the point on the planar surface are given by

$$m_x' = \tan\alpha\cos\beta \quad \text{and} \quad m_y' = \tan\alpha\sin\beta\,, \tag{3.2.1}$$

where α and β are given by $\alpha = \sin^{-1}(Rnd_1)$ and $\beta = 2\pi(Rnd_2)$. Rnd_1 and Rnd_2 indicate two independent random numbers that have values between 0 and 1. The new z-plane intercepts are calculated by

$$b_x' = b_x + (m_x - m_x')z' \quad \text{and} \quad b_y' = b_y + \left(m_y - m_y'\right)z'\,. \tag{3.2.2}$$

This completes the cycle, and the equations for the new particle flight path are defined. These are then used to find the next point of impact with the target wall.

A collision of the particle with the interior of the target's cylindrical hole is more complicated. The z-value at the point of impact is given by

$$z' = \frac{-\left(m_x b_x + m_y b_y\right) \pm \sqrt{\left(m_x b_x + m_y b_y\right)^2 - \left(m_x^2 + m_y^2\right)\left(b_x^2 + b_y^2 - (d/2)^2\right)}}{m_x^2 + m_y^2}; \quad (3.2.3)$$

recall that d is the hole diameter. The azimuthal coordinate of the point of impact is

$$\phi = \tan^{-1}\frac{m_y z' + b_y}{m_x z' + b_x} \quad \text{where} \quad \phi \rightarrow \phi + \pi \quad \text{if} \quad m_x z' + b_x < 0\,. \quad (3.2.4)$$

The slopes for the new line emerging from this point under the diffusive rebound assumption is calculated by

$$m_x' = \frac{\sin\phi \tan\alpha \cos\beta - \cos\phi}{\tan\alpha \sin\beta} \quad \text{and} \quad m_y' = -\frac{\cos\phi \tan\alpha \cos\beta + \sin\phi}{\tan\alpha \sin\beta}, \quad (3.2.5)$$

where α and β are given the same as before, following Eq. (3.2.1). Again, the new z-plane intercepts are calculated by Eq. (3.2.2), and the cycle is complete. The trajectory for the particle leaving the point of impact is defined, and the process can be repeated.

The initial position for a particle's trajectory is at the inside edge of the ring-shaped pocket at $r = L$ where the gas density is assumed to be known. The direction of the initial path is distributed randomly over the half-sphere that points toward the target center. The slopes for this path are calculated by Eq. (3.2.5), with $\alpha = \cos^{-1}(\mathrm{Rnd}_1)$. Because of azimuthal symmetry it is not essential to choose ϕ randomly, but for conceptual completeness we take $\phi = 2\pi \mathrm{Rnd}_3$. The starting z-position is given by $z_o = a(\mathrm{Rnd}_4 - 1/2)$, and the z-plane intercepts are determined by $b_x = L\cos\phi - m_x z_o$ and $b_y = L\sin\phi - m_y z_o$. Each particle propagates from the input position until it either goes out of the target hole or returns to the ring-shaped gas pocket at radius L. The flow rate of the particles can be determined from the ratio of the number of particles that successfully exit the target to the total number of trial particles. The density of the gas as a function of position is obtained by summing over the intersections of all of the particle trajectories with each elemental volume of the target.

3.2.A Calculation of Gas Density within the Target

The gas distribution in a target was calculated using the Monte-Carlo computer simulation of free molecular flow described above. Appendix A is a printout of the computer code used. The dimensions of the target in the simulation were a = 0.2 mm, c = 0.4 mm, d = 0.5 mm, and L = 4 mm [See Fig. 3.1 (b) and (c)]. The number of particles propagated through the system was such that 10,000 successfully exited the hole. The throughput probability for an individual particle was 0.014, which later will be used to find the gas flow rate. This small number indicates that very few particles entering the system actually exit the target opening before returning to the starting point (1 in 70). This can be understood in part by the relative sizes of the entrance and exit areas (a factor of 16 difference). Figure 3.2 (a) shows the calculated density of the gas as a function of z (the cylindrical axis) for five different radii uniformly spaced inside of the center hole. The density is normalized to the density at the inside edge of the ring-shaped gas pocket (length L from the center), where the backing pressure is known. As can be seen, the density is only weakly dependent on radius. The small dip near z=0 results from the fact that the particles which enter the hole from the plate region tend to move in the z-direction, whereas the particles which rebound from the interior surface of the hole tend to move in the radial direction. When particle-particle collisions were included in the calculation using a crude model (assuming Kn=1), the dip in the center tended to fill in while the rest of the density profile remained largely unchanged. Along the z-axis, the density falls off sharply at the edge of the hole (located at 0.5 mm). The reason for this sharp drop is that the particles within the hole tend to have a strong radial component to their velocity so that when they exit the hole into the free vacuum, they quickly spread away from the z-axis. Fig. 3.2 (b) shows the calculated particle density as a function of radius for $z = 0$. Again the density is normalized to that in the ring-shaped pocket, so that at a radius of 4mm (the boundary with the pocket), the density is 1. From there, the density continually drops until inside the target opening ($r < 0.25$ mm), where the density on average is ~0.2.

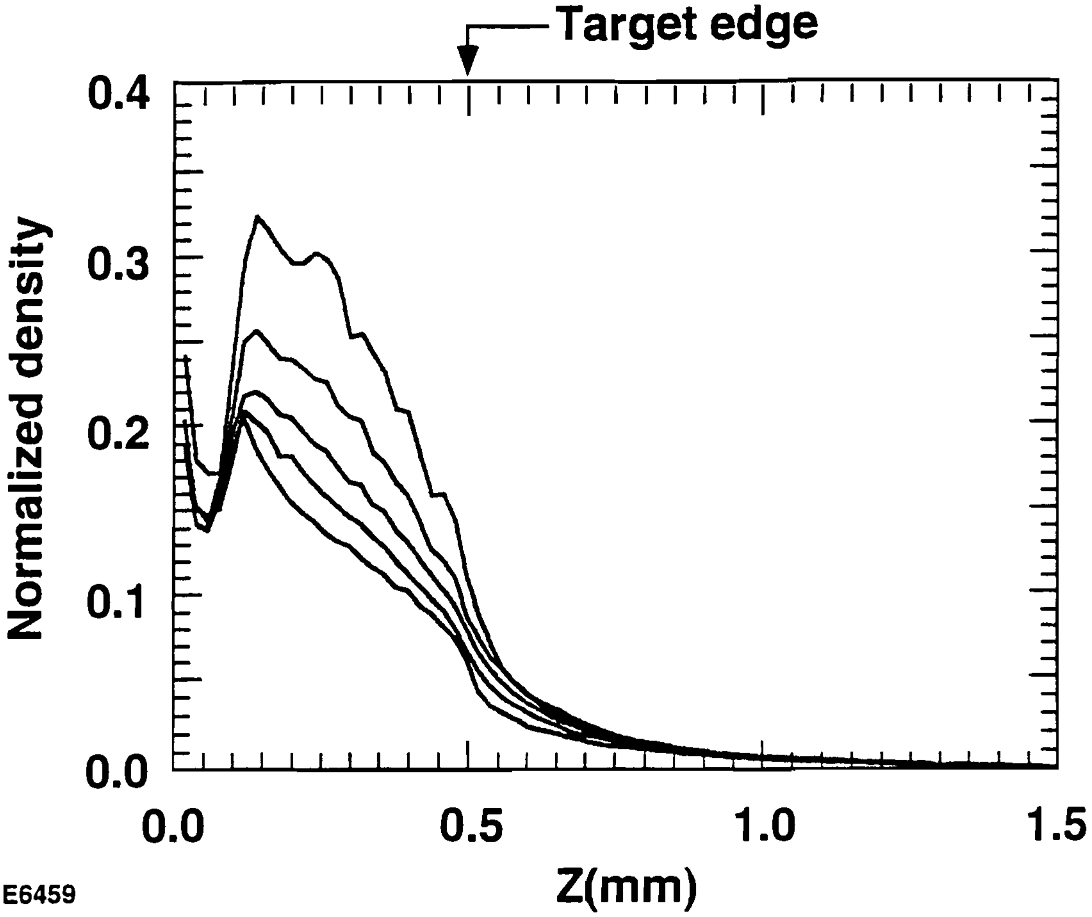

Fig. 3.2(a) The density of the gas as a function of z (the cylindrical axis) for five different radii uniformly spaced inside of the target hole. The origin is at the target center. The density is relative to the density of gas backing the device.

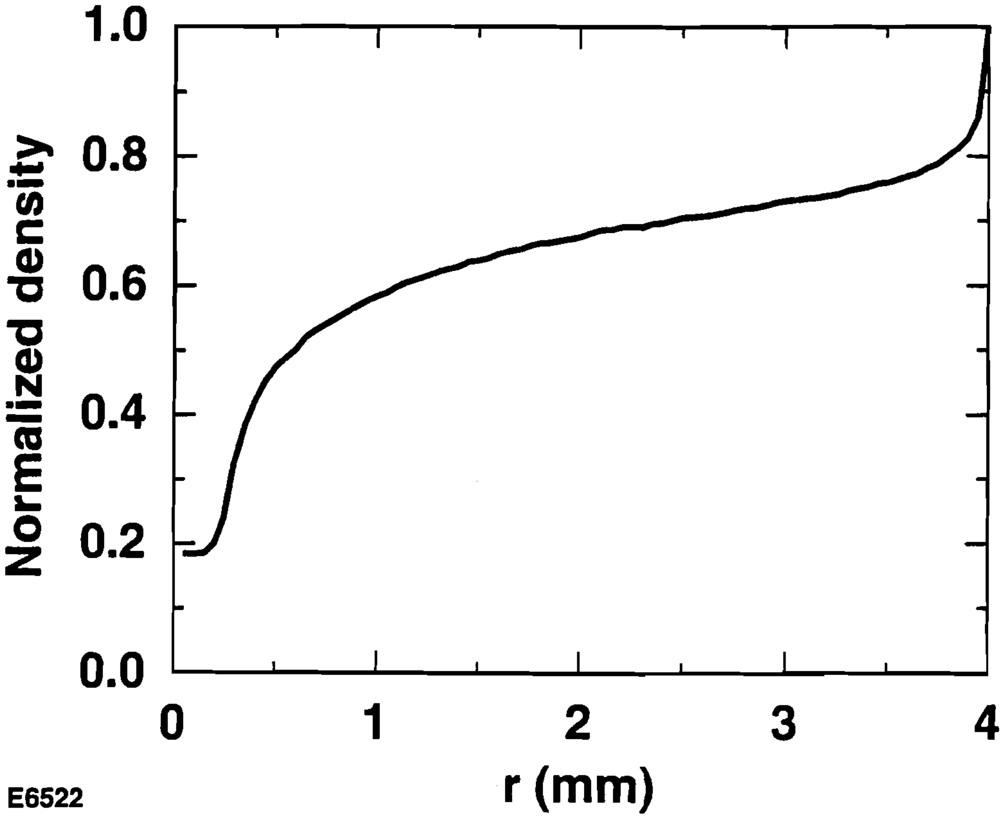

Fig. 3.2(b) The distribution of gas particles in the target as a function of radius (z = 0) from the target center out to the inside edge of the gas pocket (r = 4mm), where the density is assigned a value of 1. The target hole's cylindrical wall is at r=0.25mm.

3.2.B Gas Flow Rate

The flow rate of gas through the target can be derived from the throughput probability calculated using the Monte Carlo technique described above. The rate of particles exiting the nozzle per time is

$$\dot{N} = \rho(A\delta)\left(\frac{v_{mf}}{4\delta}\right)\gamma\,, \tag{3.2.6}$$

where ρ is the backing particle density, A is the entrance area at the edge of the ring-shaped gas pocket (2πaL), v_{mf} is the mean free velocity of the particles, and γ is the throughput probability. δ, introduced here briefly for conceptual convenience, is a small thickness that when multiplied onto the entrance area creates an element of volume. The factor of 4 in the denominator comes about since only half of the particles within the volume element are moving in a direction that will take them into the plates, and their component of velocity normal to the entrance is on average one half of the mean free velocity. Replacing ρ by N/V, where V is the fixed backing volume, and solving the differential equation yields

$$N = N_o \exp\left\{-\frac{A\gamma v_{mf}}{4V}t\right\}. \tag{3.2.7}$$

Since pressure is proportional to the number of particles, Eq. (3.2.7) applies as well to pressure. A useful term for comparison with experimental measurement is the time that it takes for the pressure to drop by a factor of 2. The half-life of the pressure is

$$t_{half} = \frac{4\ln 2V}{\gamma A v_{mf}}\,. \tag{3.2.8}$$

This theoretical result can be compared with experimental measurements as a check of the model.

A gas target with the same dimensions as those used in the numerical simulation of Section 3.2.A has been tested. The half-lives of the backing pressure in our system predicted by Eq. (3.2.8) for He, Ar, and Xe were 6 s, 19 s, and 35 s, respectively; we measured 9 s, 25 s, and 45 s. The measurements were taken at the pressures where the molecular flow range was expected to begin for the various gases. The backing pressures were 1 Torr, 0.5 Torr, and 0.3 Torr, respectively. Recall that the pressure at the target center is a factor of 5 below the backing pressure [See Fig. 3.2 (b)]. For each gas, t_{half} fell by approximately a factor of two when four times the backing pressure was applied. The higher backing pressures produced faster flow rates since intraparticle collisions began to reduce the randomness in the direction with which the particles drifted through the target. However, these pressures were still very far below the viscous flow regime (Kn>0.1). At very low pressures (Kn>2), t_{half} increased because particle collisions with the walls of the tube feeding the target began to play a significant role (i.e. molecular flow began to occur also in the tube).

To further test the accuracy of the model, we machined a different gas target with the dimensions of a = 0.12 mm, c = 0.17 mm, d = 0.35 mm, and L = 3.0 mm [See Fig.3.1 (b) and (c)]. The calculated throughput probability was 0.013, which for our system predicted a pressure half-life of 43 s for Ar; the measured half-life was 35 s. The reasonable agreement between predicted and measured flow rates lends confidence to the accuracy of the model.

3.2.C Sensitivity of Gas Flow and Density to the Nature of the Surfaces

The question arises—how sensitive is the flow of the gas in the target to the material nature of the walls? In other words, how good is the assumption that the particles rebound from the walls of the target with a Lambertian distribution? To answer the question, we explored what happens in the Monte-Carlo simulation if a fraction of the particle-surface rebounds are specular or mirror-like. For a specular reflection from the planar surface, the new slopes, rather than those of Eq. (3.2.1), are given simply by $m'_x = -m_x$ and $m'_y = -m_y$. For a specular reflection from the interior surface of the cylindrical hole, the new slopes, rather than those of Eq. (3.2.5), are given as $m'_x = \left(2\sin^2\phi - 1\right)m_x - \sin(2\phi)m_y$ and $m'_y = -\sin(2\phi)m_x - \left(2\sin^2\phi - 1\right)m_y$. The Monte-Carlo simulation was run with up to half of the interior particle-surface collisions treated as specular reflections, and it was found that there is very little effect on the spatial distribution of the gas. Only an increase in the gas flow rate was observed (40%). The model therefore seems only mildly sensitive to the nature of the surfaces.

3.3 EXPERIMENTAL MEASUREMENT OF GAS DENSITY

We have measured the gas distribution for a target with the same dimensions as previously described (a = 0.2 mm, c = 0.4 mm, d = 0.5 mm, and L = 4 mm). The distribution of gas from the target opening outwards is characterized using a 45°-off-axis imaging system that observes the recombination light from laser-induced ionization of Xe.[6] The imaging system employs a lens, a slit, and a photo-multiplier tube, which observes recombination light from a ~500-μm section of the laser beam. The gas target is positioned at various distances away from the section of the beam. Fig. 3.3 shows the experimental setup for the measurement. The laser beam was a 1-μm, 1-ps pulse that was focused with f/70 optics to a peak intensity of 2×10^{14} W/cm^2. Fig. 3.4 shows the effect of the spatial resolution of the detection scheme on the calculated density. The figure shows the axial gas distribution taken from Fig. 3.2 (a) along with its convolution with the experimental resolution of ~500μm. The measured gas density must be compared to this convolved curve to assess agreement with the calculated density.

The experimental results agree well with the theoretical predictions, especially at lower pressures. Fig. 3.5 shows a comparison in absolute pressure between the predicted and measured gas density for a backing pressure of 1.7 Torr. Again, it should be noted that the theoretical predictions are convolved by the experimental resolution. As seen in Fig. 3.4, this causes the peak density to appear below the actual value by a factor of 2. The density was calibrated by comparing the results to the signal obtained when back filling the vacuum chamber (target removed) to a known pressure (0.1 Torr). A low pressure had to be used for calibration to avoid significant refraction of the laser before it arrived to the imaged position. The gas density is proportional to the square root of the instantaneous (time scale on the order of tens of nanoseconds) recombination signal.[9]

Fig. 3.6 shows the results obtained for a wide variety of backing pressures. The gas density decreases rapidly outside of the target hole along the laser axis even for pressures up to ten times the molecular flow range cutoff. In the molecular flow range (backing pressure of 0.5 Torr), the gas density fell by more than a factor of 10 at a distance of 1mm from the target opening. With backing pressures of 3 Torr and 10 Torr applied to the target, the density dropped by a factor of 10 and 5, respectively, at 1mm. These comparisons neglected the convolution effect of the experimental resolution. Inclusion of this effect improves the contrast by about a factor of 2. The experiment thus shows that the pressure in the gas target is capable of exceeding the molecular flow regime to Kn as low as 0.1 without serious distortion to the gas distribution. It was also found that over this range of pressure the density in the target hole scales roughly with the backing pressure. Fig. 3.7 shows the measured density in the target opening plotted against the backing pressure. On the log-log plot, the points should follow a slope of 1 for them to behave like pure molecular flow. The deviation from a slope of 1 shows that the gas density profile has a slight pressure dependence when the target operates at pressures above the molecular flow range.

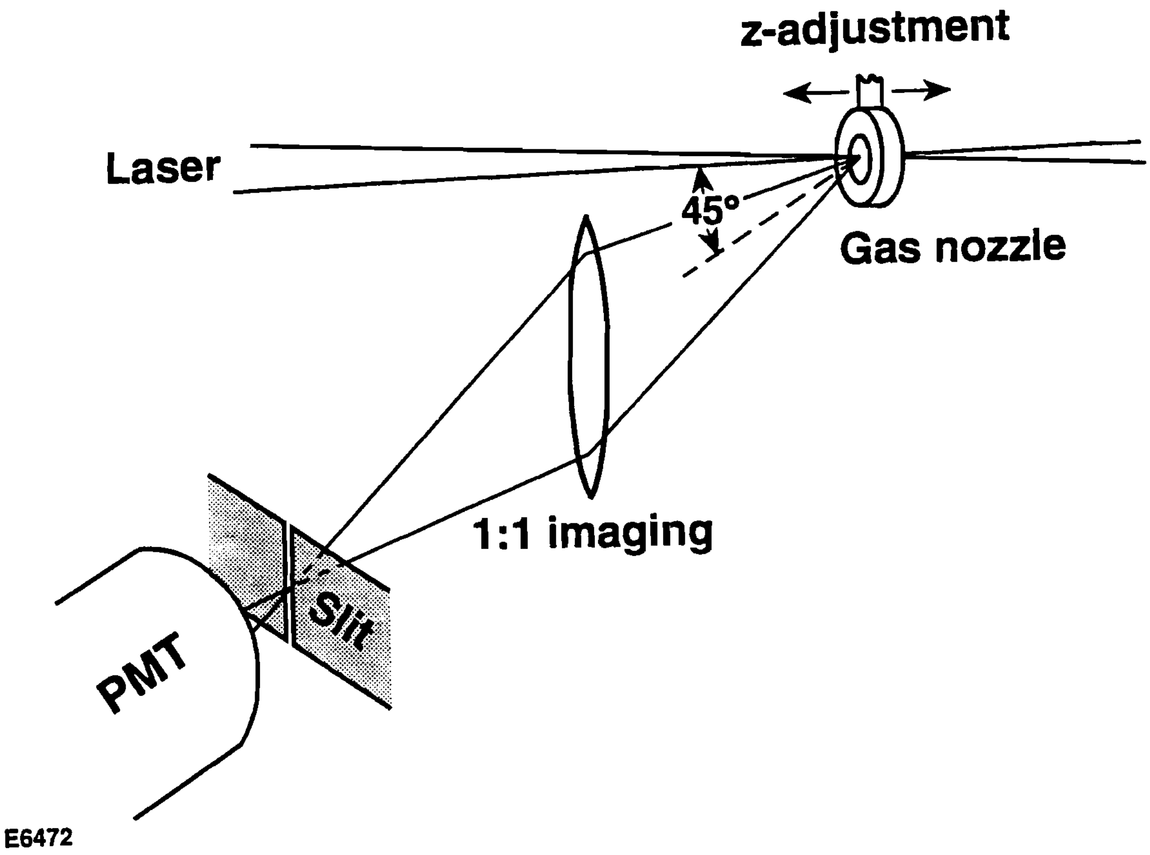
z-adjustment
Laser
45°
Gas nozzle
1:1 imaging
Slit
PMT
E6472

Fig. 3.3 The experimental setup for measuring the gas density just inside the target opening and outward along the z-axis.

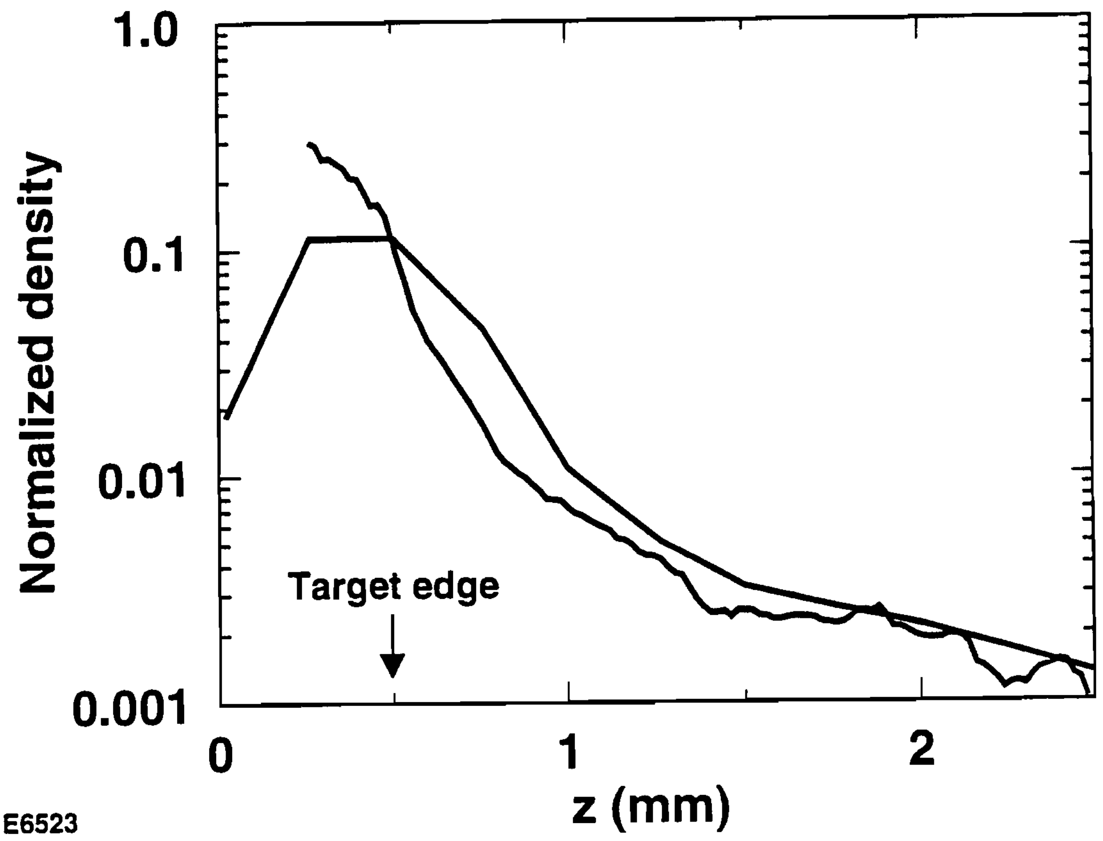

Fig. 3.4 The calculated density of the gas as a function of z along the cylindrical axis [see Fig. 3.2(a)] compared with its convolution with the detector resolution.

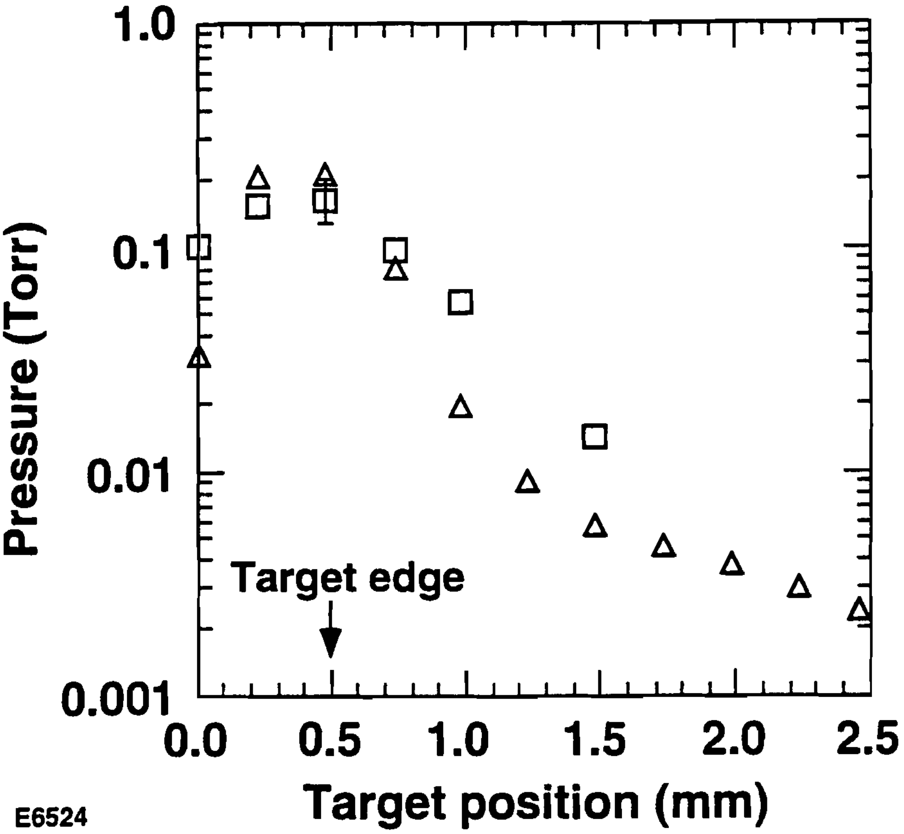

Fig. 3.5 A comparison between the predicted and measured gas density profiles for a backing pressure of 1.7 Torr. The triangles are the predicted values, and the squares are the measured ones. The third square shows a typical error bar from the experimental fluctuations.

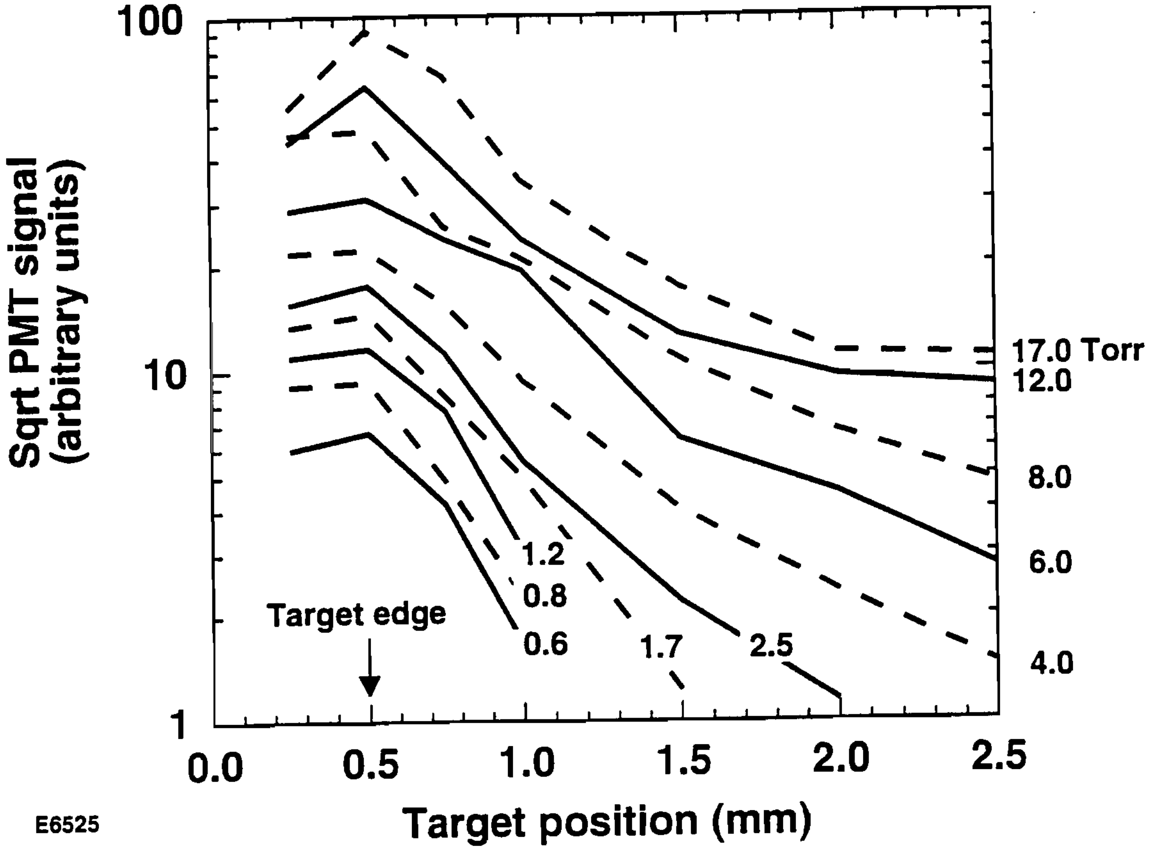

Fig. 3.6 The measured density of the gas as a function of z (the cylindrical axis) for ten different backing pressures: 0.6, 0.8, 1.2, 1.7, 2.5, 4, 6, 8, 12, and 17 Torr. The recombination light measured by the photo-multiplier tube is proportional to the square of the gas density.

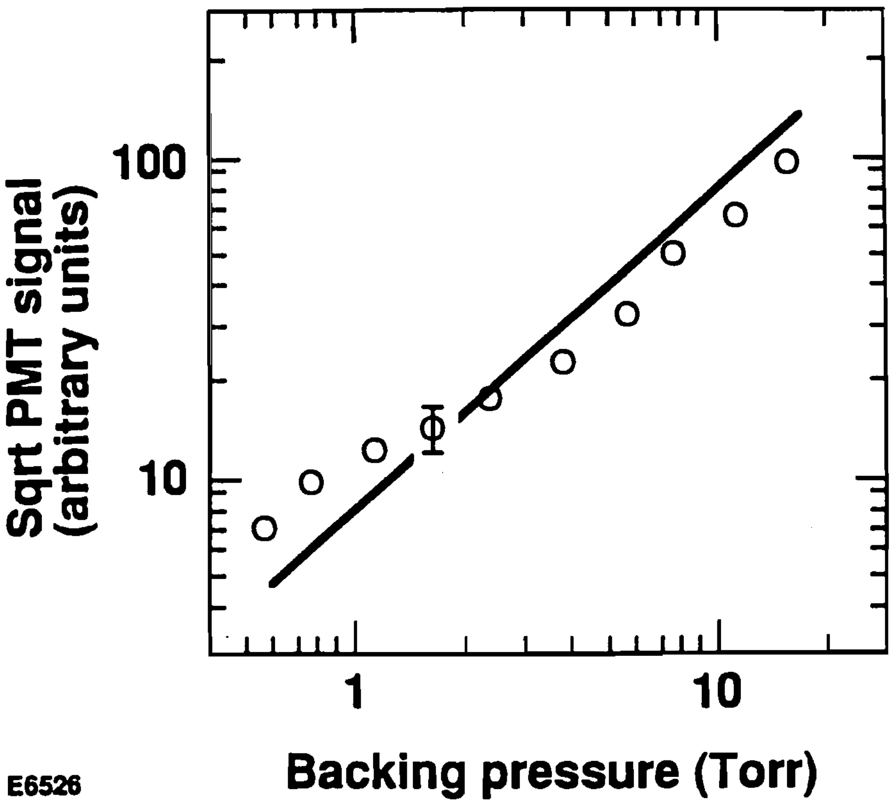

Fig. 3.7 The measured density in the target opening plotted against the backing pressure. The solid line, which is shown for comparison, has a slope of 1. The recombination light measured by the photo-multiplier tube is proportional to the square of the gas density.

REFERENCES

1. A. L'Huillier, K. J. Schafer, and K. C. Kulander, "Theoretical Aspects of Intense Field Harmonic Generation," J. Phys. B **24**, 3315–3341 (1991).
2. A. L'Huillier, K. J. Schafer, and K. C. Kulander, "High-Order Harmonic Generation in Xenon at 1064 nm: The Role of Phase Matching," Phys. Rev. Lett. **66**, 2200–2203 (1991).
3. Ph. Balcou and A. L'Huillier, "Phase-Matching Effects in Strong-Field Harmonic Generation," Phys. Rev. A **47**, 1447-1459 (1993).
4. C. T. Rettner, E. E. Marinero, R. N. Zare, and A. H. Kung, " Pulsed Free Jets: Novel Nonlinear Media for Generation of Vacuum Ultraviolet and Extreme Ultraviolet Radiation," J. Phys. Chem. **88**, 4459-4465 (1984).
5. A. McPherson, G. Gibson, H. Jara, U. Johann, T. S. Luk, I. A. McIntyre, K. Boyer, and C. K. Rhodes, "Studies of Multiphoton Production of Vacuum-Ultraviolet Radiation in the Rare Gases," J. Opt. Soc. Am. B **4**, 595–601 (1987).
6. L. A. Lompré, M. Ferray, A. L'Huillier, X. F. Li, and G. Mainfray, "Optical Determination of the Characteristics of a Pulsed-Gas Jet," J. Appl. Phys. **63**, 1791–1793 (1988).
7. G. A. Bird, *Molecular Gas Dynamics* (Clarendon Press, Oxford, 1976).
8. J. F. O'Hanlon, *A User's Guide to Vacuum Technology* (Wiley, New York, 1980).
9. H. R. Griem, *Plasma Spectroscopy* (McGraw-Hill, New York, 1964).

CHAPTER 4

EXPERIMENTAL RESULTS

We have measured and studied the far-field angular distribution of high-order harmonics created under the conditions described in Chapters 2 and 3. We have characterized the dependence of the harmonics on various experimental parameters such as gas pressure, target position, and laser intensity. The measurements indicate that, under these conditions, propagation effects within the medium play a minimal role in determining the far-field angular distribution of the harmonics.

4.1 FAR-FIELD ANGULAR DISTRIBUTION

The harmonics appear on the detector as a line of finite width (refer to Figs. 2.5 and 2.7). The width of each line typically occupies about 10 CCD pixels while the length of the line occupies about 200 pixels. Each pixel is assigned a numeric value (0-255) according to the brightness of the harmonic image. Thus, for each harmonic line, there are approximately 10 one-dimensional rows of pixels which sample the energy along its length. These several can be averaged together and plotted as a function of position along the harmonic line to reveal the far-field angular profile of the harmonic. Fig. 4.1 shows the angular profiles of the 11th through 21st harmonics produced in Xe at an intensity of 8×10^{13}W/cm^2. The approximate laser distribution is also depicted for comparison. The pressure of the gas in the target for this shot was 0.3 Torr, and the target was positioned at the laser beam waist. The data was taken with the 1μm grating setup described in Chapter 2. The harmonics all show a narrow central peak which diminishes slightly in width as the harmonic order increases. The 13th harmonic shows broad wings which are slightly wider than the laser beam itself. If the signal is enhanced by increasing the gas pressure, similar wings are observed on almost every

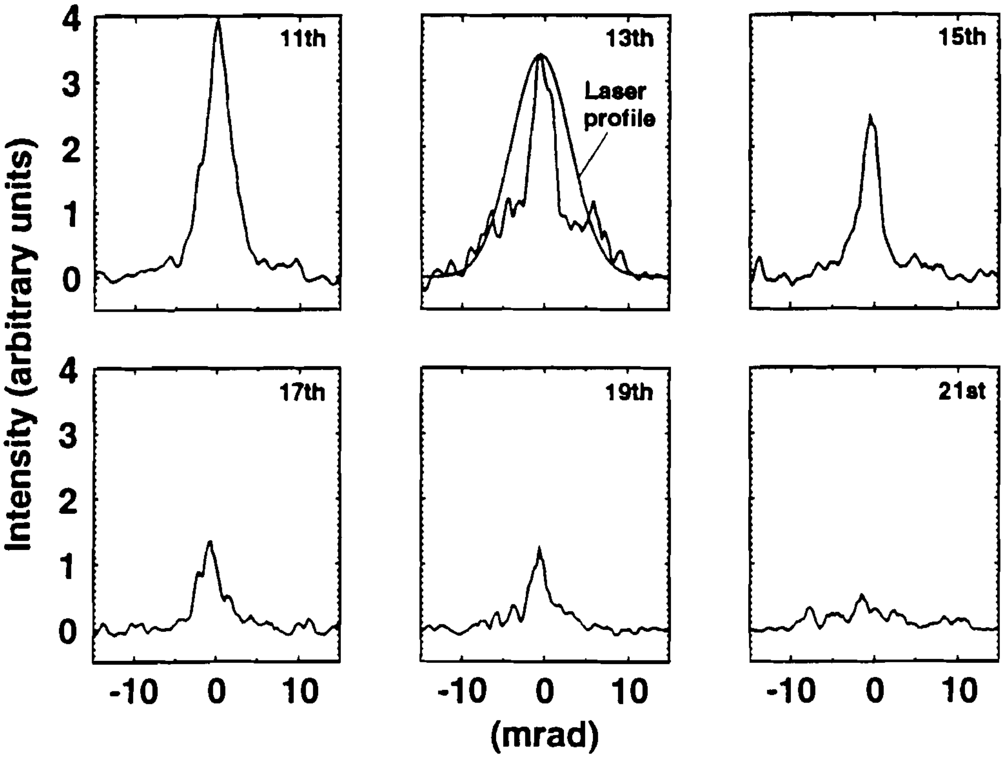

Fig. 4.1 The far-field angular profiles of the 11th through 21st harmonics produced in 0.3 Torr Xe at an intensity of 8×10^{13} W/cm^2. The profiles were obtained from a single shot.

harmonic. However, increasing the signal causes the central peaks to saturate on the detector. For Xe, the wings are the strongest on the 13th. Similar behavior can be seen in Kr and Ar, the wings appearing most pronounced on the 15th harmonic in Kr and on the 17th in Ar.

Fig. 4.1 was obtained from a single shot. Because the creation of the harmonics is a strongly non-linear process, small fluctuations in the laser parameters can cause significant variations in the harmonic images from shot to shot. However, the overall features seen in Fig. 4.1 are typical of data with nominally the same conditions. As a rule of thumb, the noise in the data is related to the amount of asymmetry in the harmonic curves. That is, any feature in the harmonic profile which does not appear the same on both sides of the center must be due to error, whether from scattered light or particles hitting the detector, from distortions in the laser or gas distribution, or from nonuniformities in the detector itself. An analysis of the fluctuations and errors in the data is given in Section 4.5.

4.2 DEPENDENCE ON GAS TARGET PARAMETERS

A number of experimental parameters were varied to explore what effects there might be on the harmonic emission. Some of these parameters are: the gas target thickness, the target position relative to the laser focus, the gas density, the laser intensity, the laser frequency, and the laser polarization. A discussion of the harmonic dependences on the laser parameters is given in the next section. For our experimental conditions, only a variation of the atomic species or the laser parameters such as intensity or polarization fundamentally alters the far-field profiles of the harmonic emission.

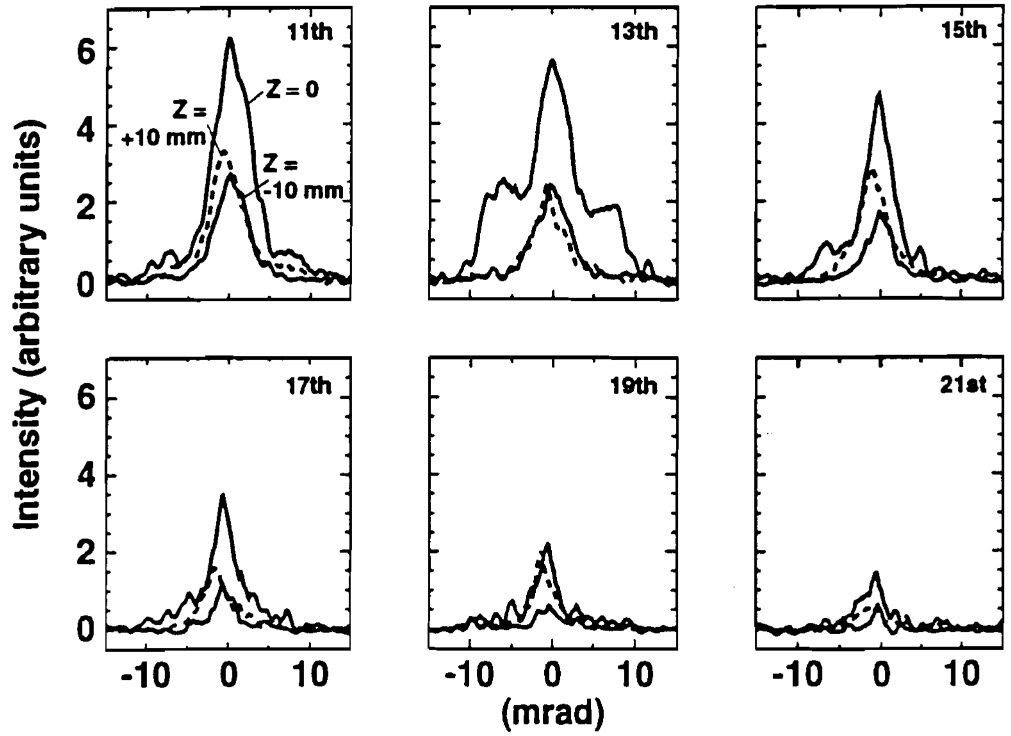

Fig. 4.2 The far-field angular profiles of the 11th through the 21st harmonics produced with 0.5 Torr Xe and $8x10^{13}$ W/cm^2 (at focus) for shots at three target positions: $z=-1.7z_o$, $z=0$, and $z=+1.7z_o$.

4.2.A Dependence on Target Position

The far-field angular profiles of the harmonics were investigated as a function of gas target position relative to the laser focus. In contrast to experiments by L'Huillier and co-workers[1-4] who saw dramatic changes in the harmonic emission with a change in gas target position, the changes observed in these experiments were primarily due to the decrease in intensity associated with moving away from the focus. The reason for the difference is that in this work, the gas distribution is much narrower than the laser confocal parameter. Fig. 4.2 shows the far-field angular profiles of the 11th through the 21st harmonics at 0.5 Torr Xe and 8×10^{13} W/cm^2 (at focus) for shots at three target positions: $z=-1.7z_0$, $z=0$, and $z=+1.7z_0$, where z_0 is the Rayleigh range of the laser focus. The data was taken with the 1μm-grating setup described in Chapter 2. As the target is moved away from the focus in either direction, the harmonic energy drops and the wings diminish and disappear altogether at a distance of about z_0. At $z = \pm z_0$, the laser intensity is half what it is at the focus. When the laser intensity is doubled at these positions, the wings can be seen again but they are less pronounced and slightly narrower. The narrower far-field pattern can be attributed to emission from a wider interaction area when it is considered that the wings come from a phase interference. The central structure, however, does not grow narrower and may even broaden slightly (not evident in Fig. 4.2).

4.2.B Dependence on target thickness

Two additional targets were fabricated which have thicknesses of 0.5mm and 2mm. Harmonic production from these targets was compared with the production from the usual 1mm target. Their far-field harmonic angular patterns were virtually identical to the far-field patterns generated by the 1mm target. This is expected since all of the target thicknesses are much less than the 13mm laser confocal parameter. The fact that the far-field angular profile is not influenced by small changes in the target thickness indicates that a regime has been achieved where the harmonics can be thought of as emerging from a simple plane at the focus. The thickness then only influences the efficiency of production. The strength of the harmonic emission was about the same for the 1mm and 2mm targets, and about 50% less for the 0.5mm target. At first it might seem that each time the target thickness is doubled, the harmonic emission should increase by a factor of 4. However, this is only true if each gas target thickness is significantly less than the harmonic coherence length. The coherence length is defined to be the propagation distance over which harmonics get out of phase with newly created harmonics by a factor of π. As will be explained in Chapter 5, the geometric coherence length of the harmonics for our conditions is approximately 1mm, so using a 2mm target rather than a 1mm target does little to boost harmonic production.[5,6] The 0.5mm target is thinner than the harmonic coherence length and so the conversion efficiency decreases. A more detailed comparison between the relative strengths of the harmonic emission from the different targets would require a more careful calibration of the targets. Only the 1mm target was calibrated in detail so there is some uncertainty in the relative target pressures. However, for these experiments the pressure in all of the targets was calculated to be the same.

4.2.C Dependence on Pressure

The total energy for a given harmonic can be found by integrating the harmonic far-field distribution, taking into account the circular symmetry. Since the detector is not absolutely calibrated, it is sufficient to do the calculation as

$$\mathrm{Energy}_{\mathrm{total}} \propto \int_0^{\pi/2} \theta\, d\theta\, \mathrm{Energy}(\theta) \qquad (4.2.1)$$

where θ is the angle of divergence from the z-axis. The dependence of the total harmonic energy is plotted in Fig. 4.3 as a function of target pressure. The 0.2μm grating setup was used to obtain this data. As expected, the harmonic signal follows very nearly the square of the pressure. This indicates that at these pressures the optical index of the medium does not contribute significantly to the collective characteristics of the harmonic emission. The fact that the harmonic production can be adjusted by changing the gas pressure allows the convenience of bringing into proper detector range whatever feature of the harmonic far-field pattern is of interest. Because of the good control over the gas pressure, this technique can be used to produce scans with a greater dynamic range than what the detector itself will allow.

4.3 DEPENDENCE ON LASER PARAMETERS

The harmonic emission increases rapidly with laser intensity until a saturation limit, above which the signal increases only gradually. This is the range of the harmonic plateau, where many harmonic orders are emitted with approximately the same strength. The intensity at which saturation of harmonic emission occurs is about 5×10^{13} W/cm^2 for Xe, 8×10^{13} W/cm^2 for Kr, and 1.5×10^{14} W/cm^2 for Ar. These intensities are roughly a factor of 2 below where the gas is strongly ionized.[7,8]

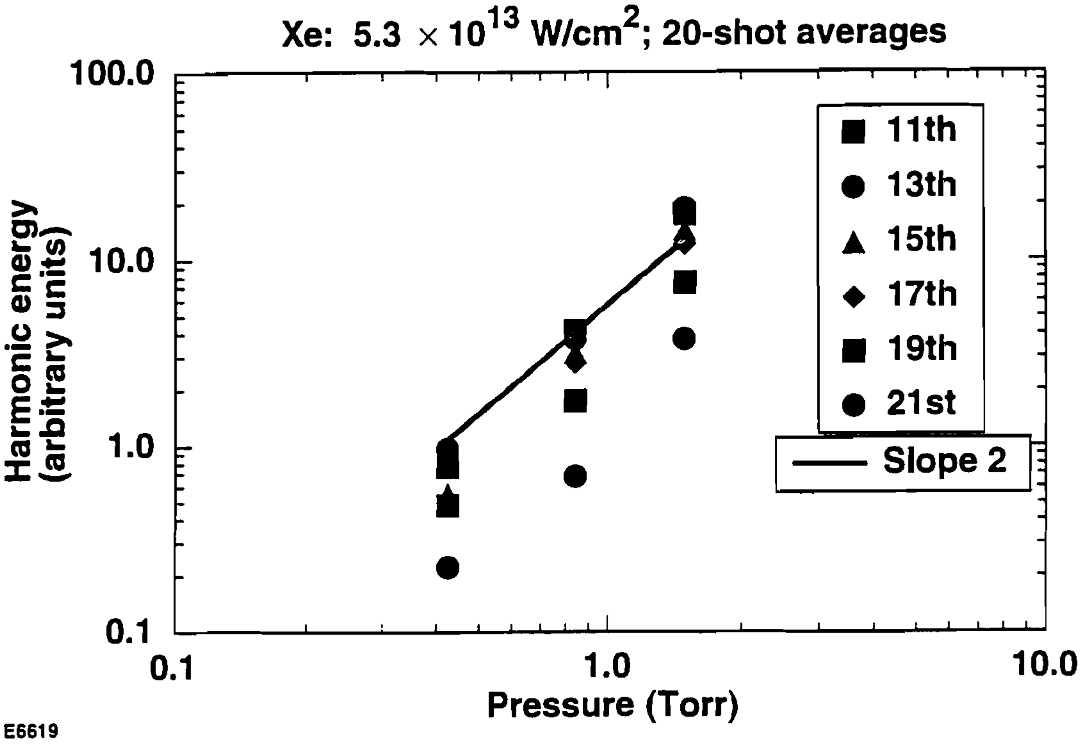

Fig. 4.3 The total harmonic energy plotted as a function of target pressure. Each point is a 20-shot average taken in Xe at 5.3x10^{13} W/cm^2.

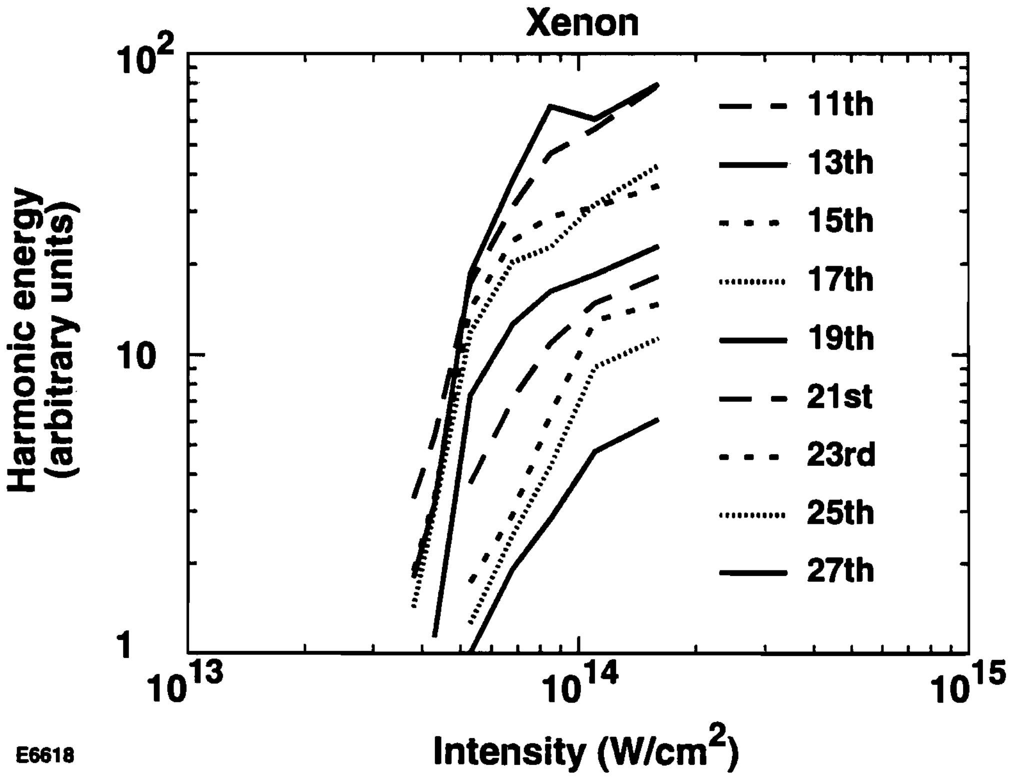

Fig. 4.4 The relative harmonic energy for the 11th through 27th harmonics in Xe as a function of laser intensity. The pressure has been varied to keep the detector from saturating, and the measured signal was adjusted by the square of the pressure. Each point is an average of approximately 20 shots (typical fluctuation 25%). The uncertainty in the absolute laser intensity is 35%.

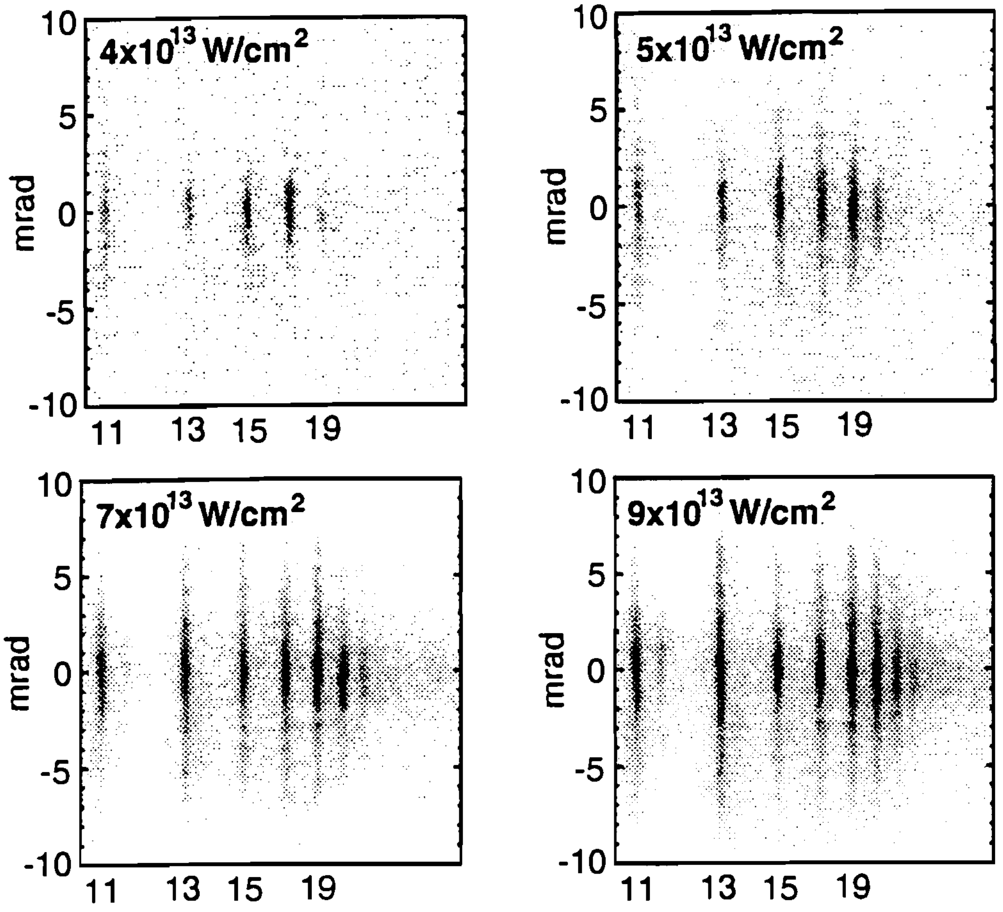

Fig. 4.5 (a) Images of the angular distributions of harmonics generated in Xe as a function of laser intensity at 0.85 Torr. Each image is an average of 20 shots.

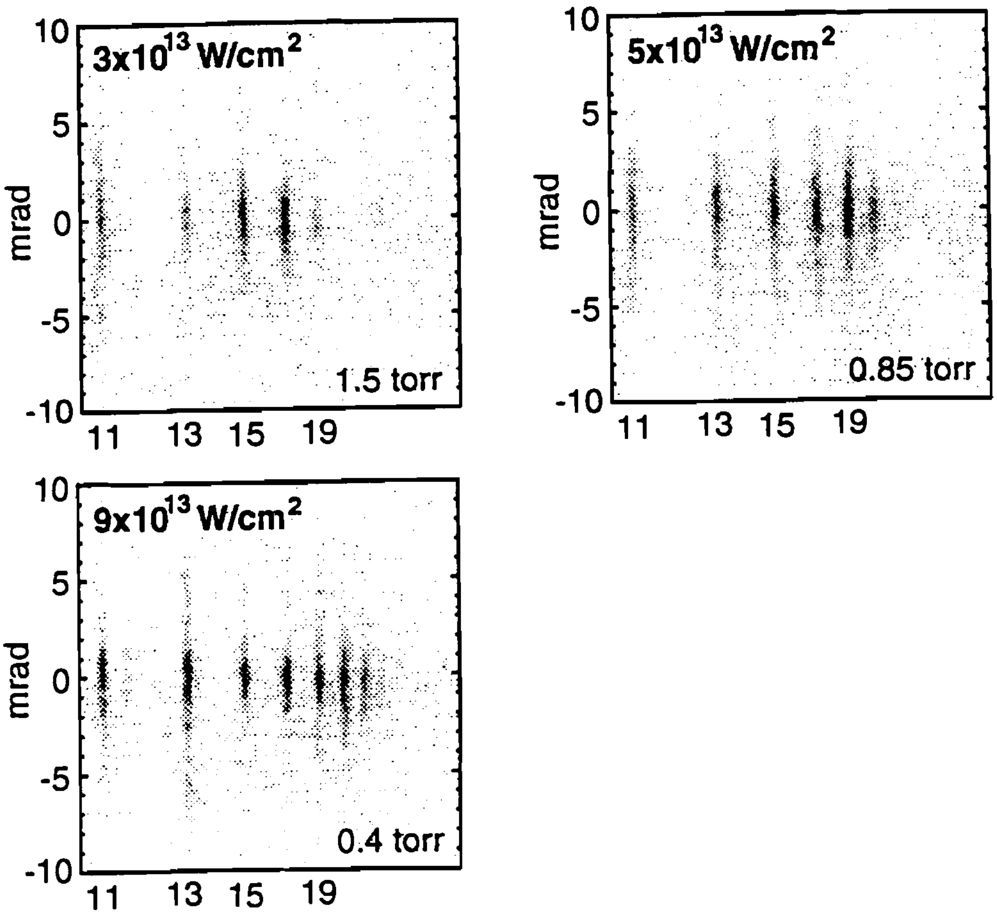

Fig. 4.5 (b) A similar intensity scan for Xe as in 4.5 (a), but the pressure is varied so that the detector signal remains roughly constant. Each image is an average of 20 shots.

4.3.A Dependence on Laser Intensity

Fig. 4.4 shows the relative energy in the 11th through 27th harmonics in xenon as a function of laser intensity. The 0.2μm grating setup was used in this measurement. Each point along the curve was determined by averaging together twenty shots. To enhance the dynamic range, higher gas pressures were used to determine the points of weaker emission, and lower pressures were used to determine the points of stronger emission. The pressure dependence was assumed to be quadratic. The development of a plateau with increasing laser intensity is evident. The center of the focal region begins to ionize strongly around 8×10^{13} W/cm^2.[7,8]

Fig. 4.5 (a) shows far-field images of harmonics produced in Xe as a function of laser intensity. Each picture is an average of 20 images. A discussion of the averaging technique as well as the amount of fluctuation and error in the data is given in Section 4.5. The 0.2μm grating configuration was used to obtain this data and all other data presented in this section. The pressure was held constant at 0.85 Torr for this series of pictures, so at the higher intensities the central portions of the harmonic lines are saturated. With increasing intensity, more harmonics become visible and a broad wing structure becomes apparent on nearly every harmonic. It should be recalled that the 0.2μm grating attenuates the lower harmonics (orders in the teens) relative to the higher ones. The lower harmonics should in fact appear about 4 times brighter than they do. Fig. 4.5 (b) shows a similar scan in Xe, but the pressure is reduced as the harmonics get brighter to avoid detector saturation. Still, the central peaks in many cases are saturated. This scan clearly shows that the wing structure is a function of intensity. For example, at the lower intensities, the 13th harmonic shows little if any sign of the having the wing structure while neighboring harmonics exhibit wings.

However, at higher intensities, the 13th harmonic shows some of the strongest wings, while the wings on the neighboring harmonics are not as strong.

Fig. 4.6 shows the energy of the harmonics produced in Xe as a function of harmonic order for a number of different laser intensities. As the intensity increases, the harmonic plateau extends further out as more harmonics appear. Each point along the curve was determined from an average of twenty shots. Again, the pressure was varied to enhance the dynamic range of the measurement.

Figs. 4.7 (a) and 4.7 (b) are similar to the intensity scans of Figs. 4.5 (a) and 4.5 (b) except that these are generated in Kr instead of in Xe. It should be noted that the second-order diffraction of the higher harmonics produces lines in the region near the lower harmonics. At times, they are quite bright and should not be confused with the lower harmonics. The harmonics generated in Kr behave similarly to the harmonics generated in Xe. Kr is able to produce more harmonics than Xe, and the wings are configured differently on the various harmonics. In Kr a prominent set of wings appears on the 15th harmonic similar to the set seen on the 13th harmonic in Xe.

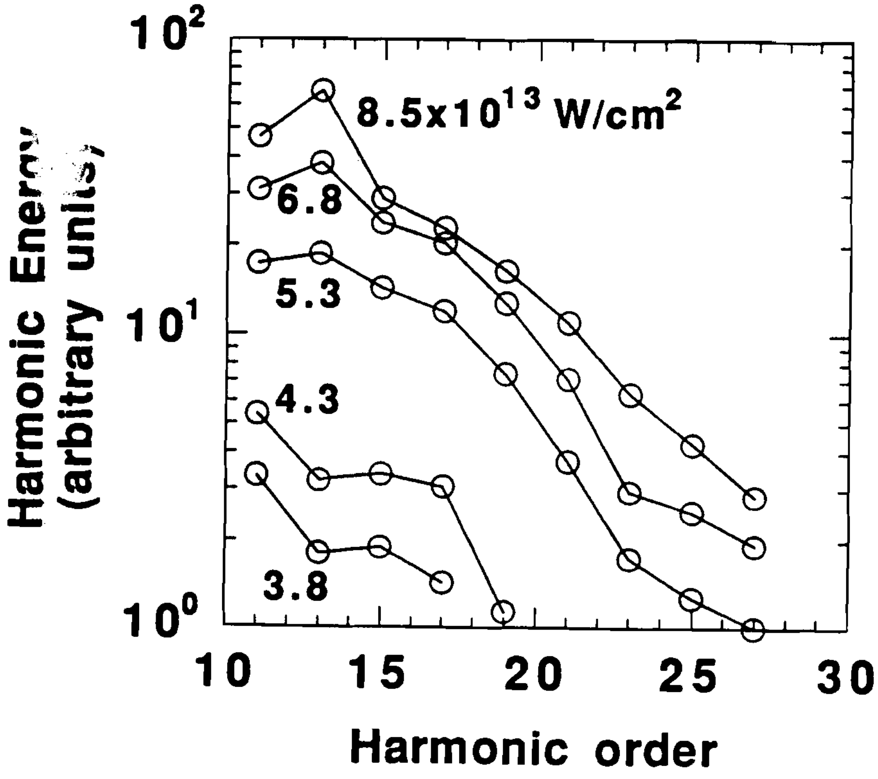

Fig. 4.6 The harmonic energies as a function of harmonic order for various laser intensities in Xe. The gas pressure was varied for the different data points to avoid detector saturation, and the measured signal was adjusted by the square of the pressure. Each point is an average of approximately 20 shots (typical fluctuation 25%). The uncertainty in the absolute laser intensity is 35%.

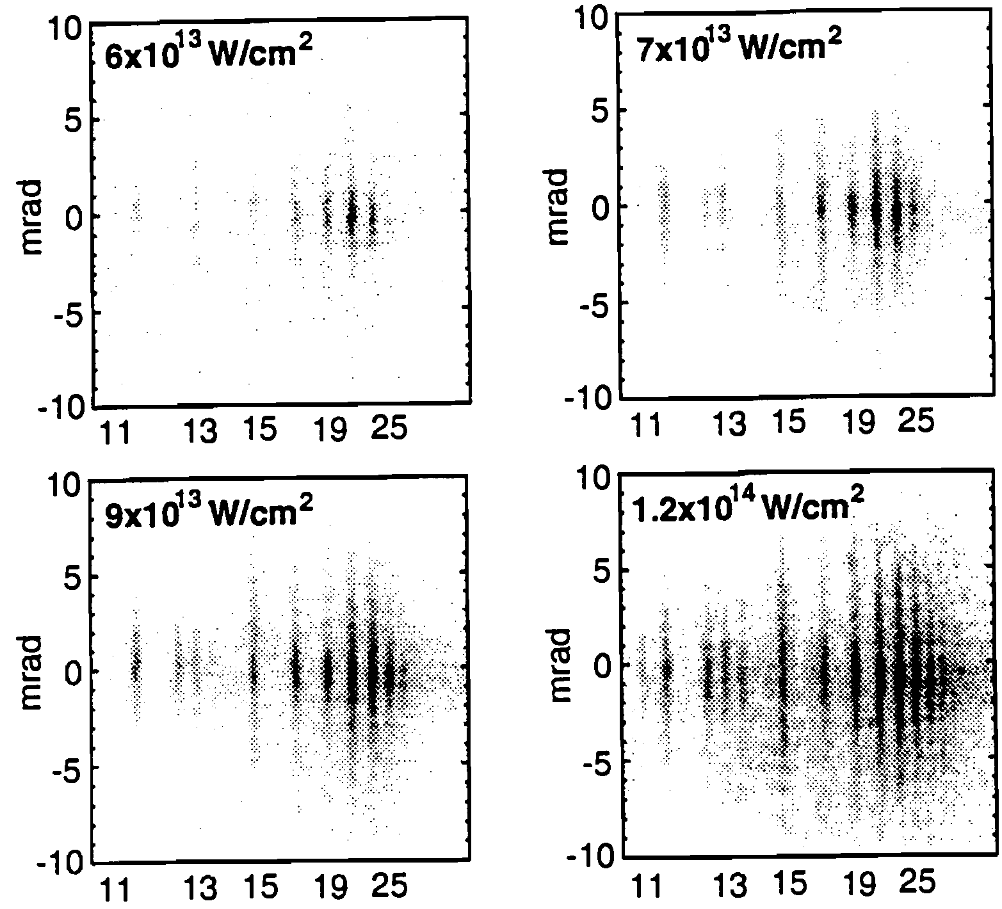

Fig. 4.7 (a) Images of the angular distributions of harmonics generated in Kr as a function of laser intensity at 2 Torr. Each image is an average of 20 shots.

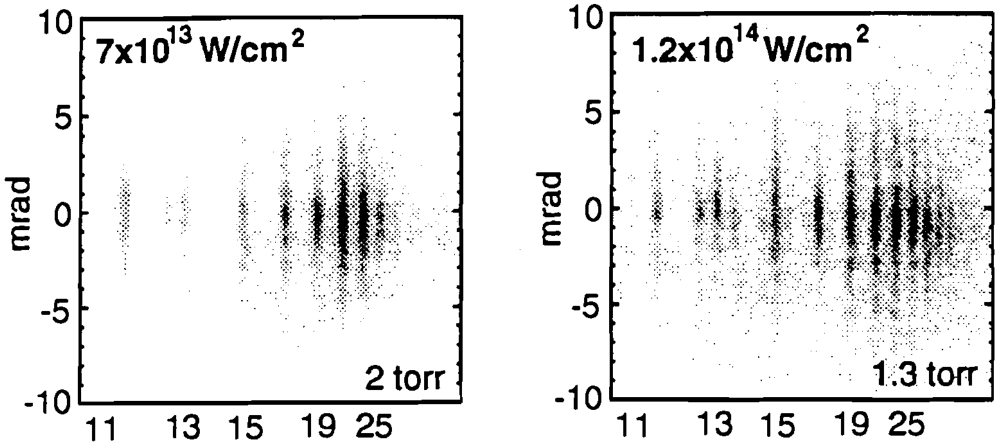

Fig. 4.7 (b) A similar intensity scan for Kr as in 4.7 (a), but the pressure is varied so that the detector signal remains roughly constant. Each image is an average of 20 shots.

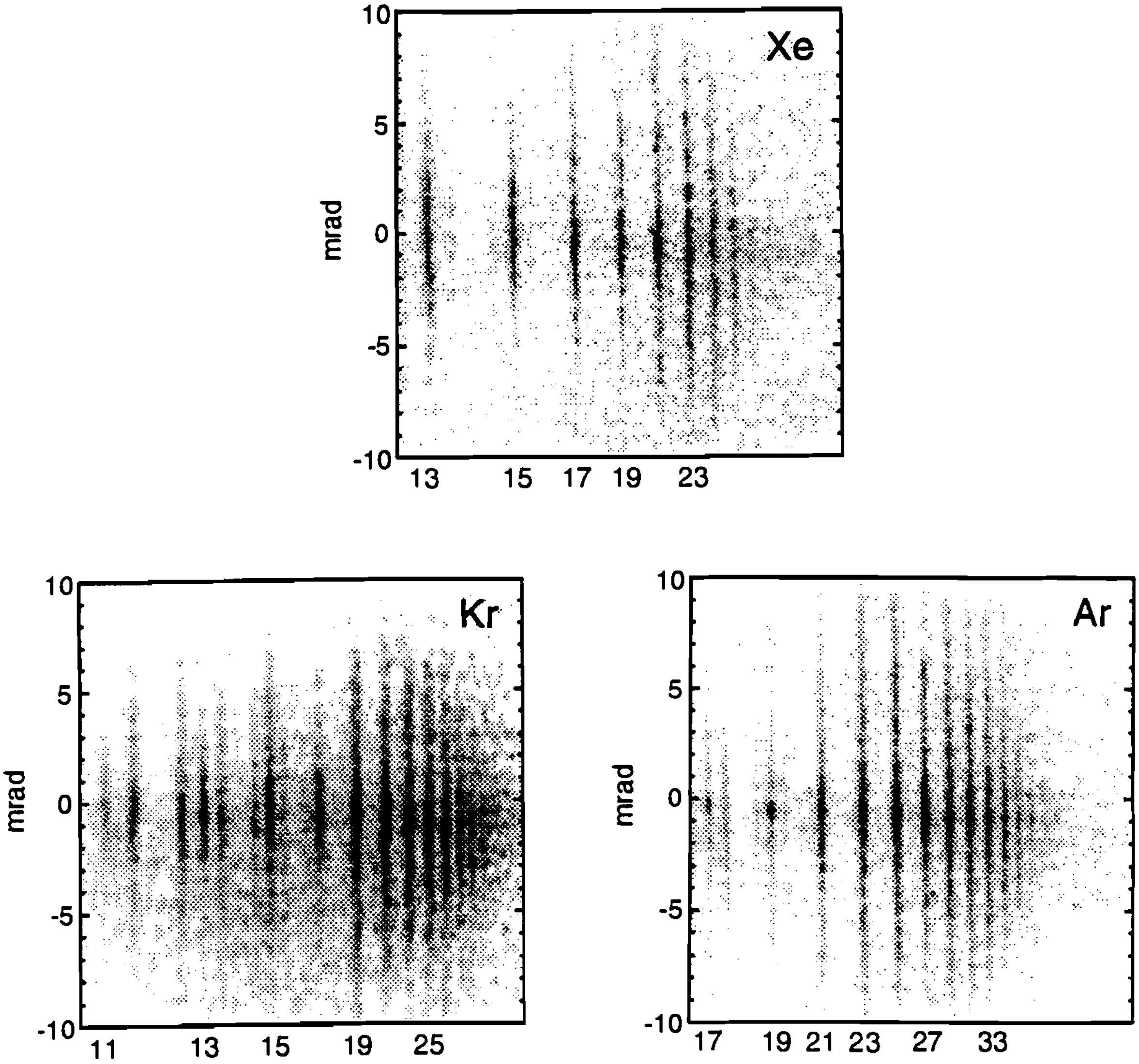

Fig. 4.8 Images showing the highest-order harmonics observed in Xe, Kr, and Ar respectively. The gas pressures were 1 Torr, 2 Torr, and 4 Torr respectively. Except for the highest harmonics, the central peaks on the harmonics are well saturated. Each image is an average of about 4 shots.

4.3.B Highest Harmonics Observed

The gas pressure and laser intensity were increased in an effort to see the highest harmonic orders possible with the experimental setup. Fig. 4.8 shows the highest-order harmonics observed in Xe, Kr, and Ar respectively. The gas pressures used were respectively 1 Torr, 2 Torr and 4 Torr. These shots were taken with the 0.2μm grating setup. In Xe, harmonics up to the 29th (34eV) were visible, in Kr harmonics up to the 35th (41eV) were visible, and in Ar harmonics up to the 41st (48eV) were visible. The energies of the harmonics are far in excess of the electron atomic binding potentials which are 12.1eV, 14.0eV, and 15.8eV respectively.

4.3.C Dependence on Beam Polarization

The harmonic production has been studied as a function of laser polarization. A half-wave plate was inserted in the laser beam before the focusing lens, and the harmonics were observed as a function of the direction of linear polarization. Rotating the polarization had no effect on the harmonic emission. In other words, the harmonic beams which are sampled by a 1-dimensional cut through their center, are indeed circularly symmetric. This observation could have been made as well by rotating the spectrometer instead of the beam polarization.

Harmonic production was also investigated as a function of laser beam polarization ellipticity. The ellipticity is defined as the ratio of the peak field along the minor polarization axis to the peak field along major polarization axis (E_y/E_x). A quarter-wave plate placed in the laser beam introduced varying degrees of ellipticity depending on its orientation. For circularly polarized light, the harmonics completely disappear as expected by angular momentum arguments. The closer the laser light is to being linearly polarized, the more efficiently the harmonics are generated. Fig. 4.9 shows harmonic production at fixed laser intensity as a function of beam ellipticity for

Xe and Kr. Each point represents an average of about 20 shots. The elliptical light can be thought of as the sum of purely linear and circular fields. As the light becomes more elliptical, the harmonic production decreases more rapidly than can be explained simply by the reduction in the strength of the linear component of the field. The higher-order harmonics decrease faster with increasing beam ellipticity than do the lower-order harmonics.

4.3.D Harmonics of Green Light

The laser light was frequency doubled using a KDP crystal, and the resulting 527nm beam was used to generate harmonics in Xe. The focal spot area was measured to be a factor of 2 smaller than the 1054nm beam. This was verified by measuring the spot with a CCD camera. For our doubling crystal, the temporal envelope of the green beam is of about the same in duration as the 1054nm beam. Fig. 4.10 (a) shows the far-field pattern of the harmonics of the green beam as a function of intensity. Each image is an average of several shots. As the intensity of the green light increases, the number of harmonics increases. Harmonics above the 7th appear rather suddenly and only at a relatively high intensity (1×10^{14} W/cm^2). The angular patterns of the harmonics are similar to the patterns observed with the infrared beam, bright central peaks with broad wings. Fig. 4.10 (b) shows the harmonics created at the highest intensity shown in Fig. 4.10 (a), 1×10^{14} W/cm^2, as a function of gas pressure. It was determined that the wings are less in intense than the central peaks by a little more than an order of magnitude.

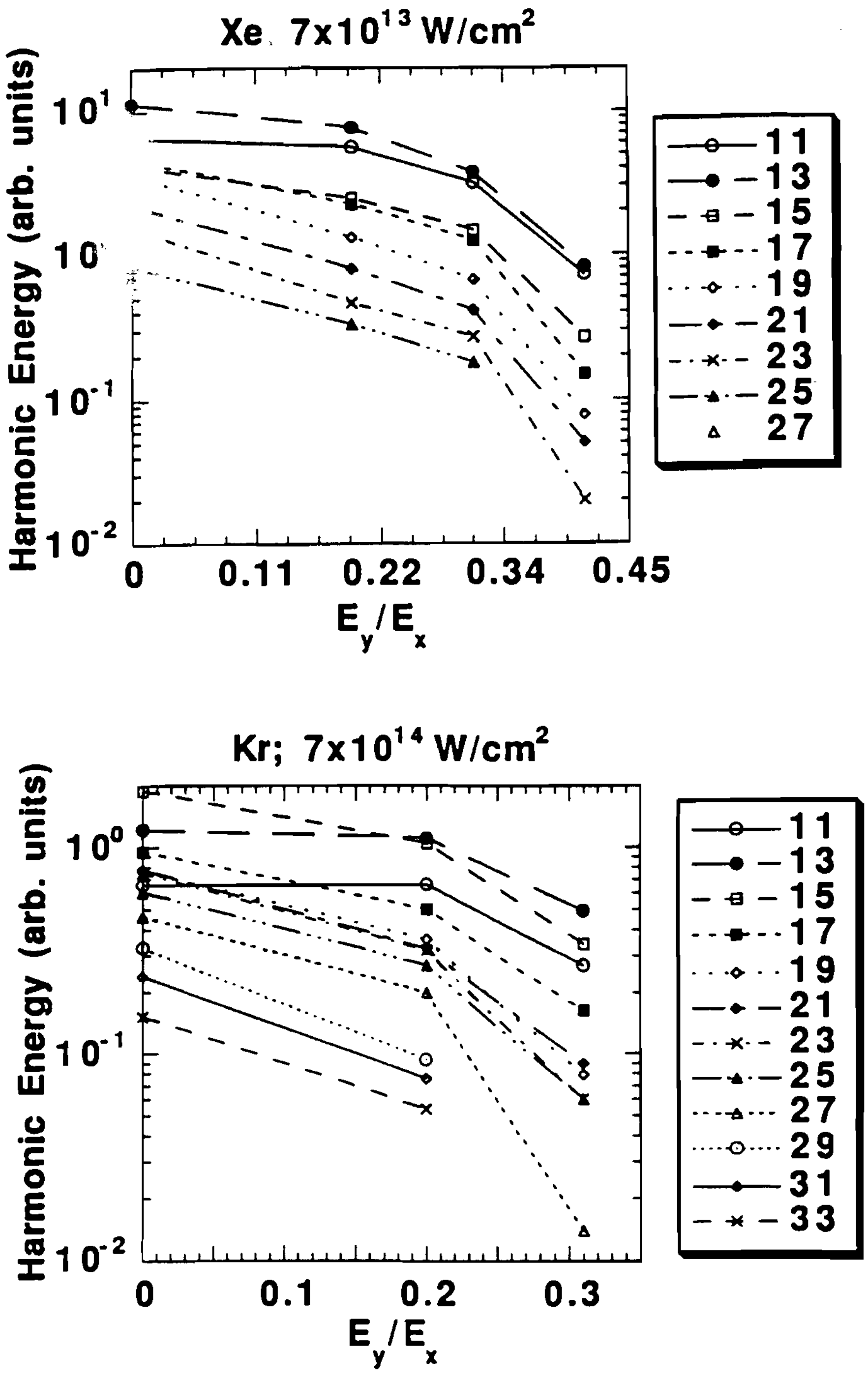

Fig. 4.9 Harmonic production at 7x10^{13} W/cm^2 laser intensity as a function of laser ellipticity for Xe (a) and Kr (b).

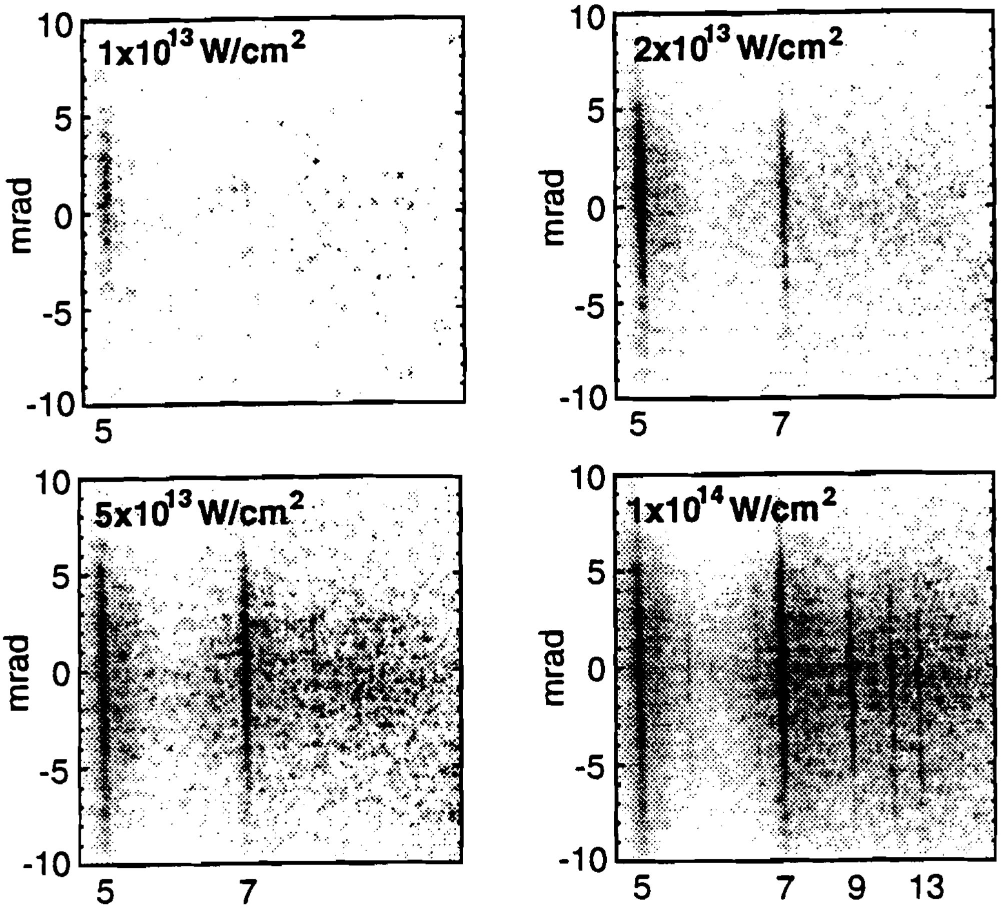

Fig. 4.10 (a) Far-field images of the harmonics of green light (527nm) produced in 1.5 Torr Xe as a function of laser intensity. Each image is an average of approximately 10 shots.

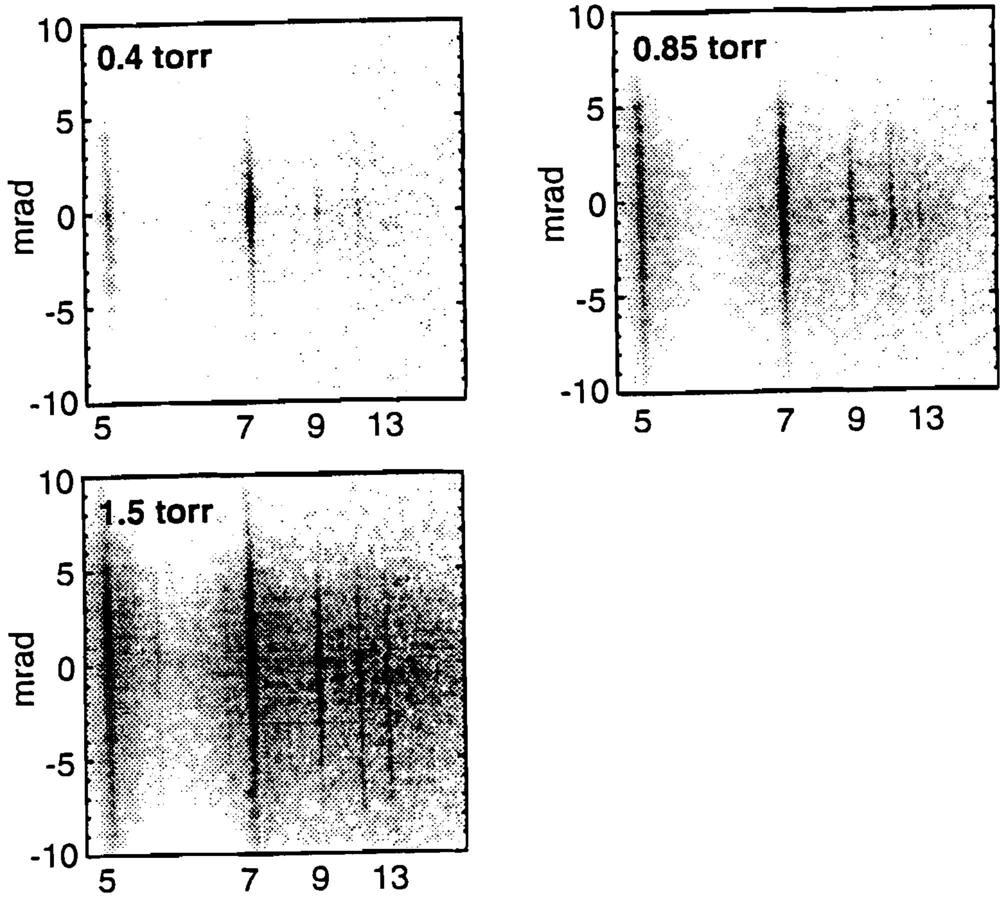

Fig. 4.10 (b) Far-field images of the harmonics of green light (527nm) in Xe produced at 1×10^{14} W/cm^2 for different gas pressures. Each image is an average of approximately 10 shots.

4.4 ATOMIC SPECIES DEPENDENCE

The angular profiles of harmonics generated in Kr and Ar have behaviors similar to the profiles of harmonics generated in Xe. An important difference, as previously discussed, is the number of harmonics created and the laser intensities required to make them. One feature which is common to all of the far-field distributions is the development of broad wings. The strength of the wings is not only a function of harmonic order but also of atomic species. A striking difference between the atomic species can be seen in the wing structure on the lower-order harmonics. The far-field emission for Xe, Kr, and Ar is shown in Fig. 4.11. Each curve is an average of four shots. The 1μm grating setup was used for these images. For this data, some of the central peaks are slightly saturated. For Xe, Kr and Ar, a prominent set of wings appears on the 13th, 15th and 17th harmonics respectively. These wings appear on the harmonic with energy which, for each gas, is one order higher ($2\omega_L$) than the first harmonic with greater photon energy than the field-free atomic ionization potential. The shift of the pattern with atomic species is evidence that the effect is a manifestation of atomic physics and not simply an artifact of propagation in the medium.

Although the intensity of the harmonic wings is typically an order of magnitude less intense than the central peaks, they often carry a large fraction of the total harmonic energy, owing to the circular symmetry. Investigations of harmonics produced in Xe and Kr showed that the wings of many harmonics often contain about three times the energy as the center peaks.

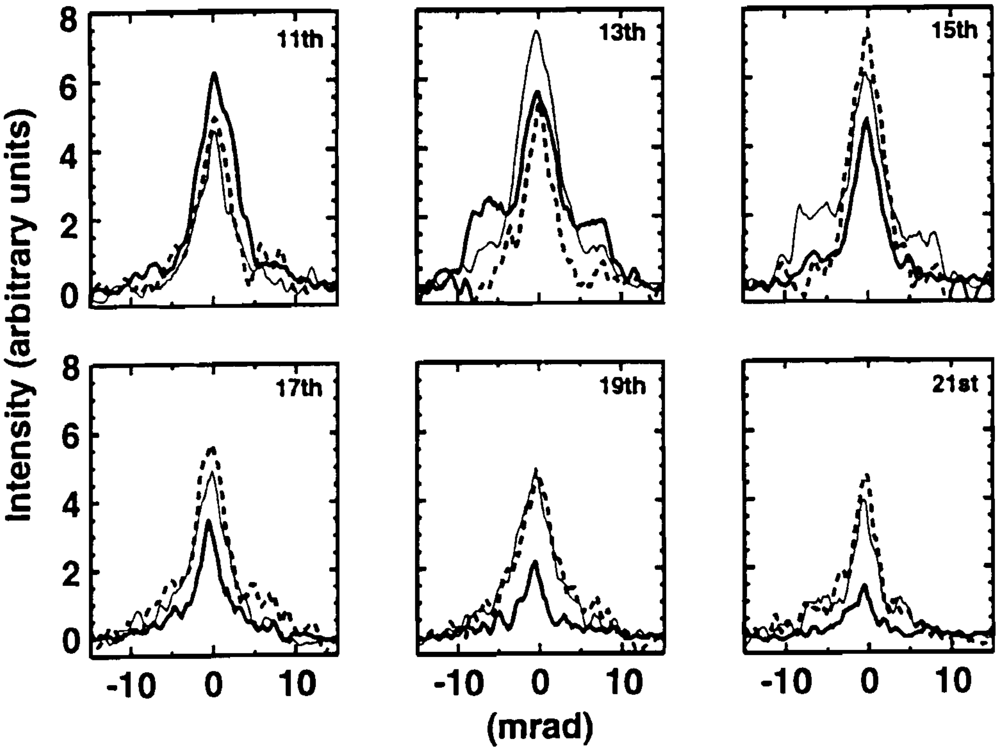

Fig. 4.11 The far-field patterns of the 11th-21st harmonics emitted from Xe (thick line), Kr (thin line), and Ar (dashed line). Each curve represents a single shot. The gas pressures were 0.5 Torr, 1.2 Torr, and 2 Torr, and the peak laser intensities were 9×10^{13} W/cm^2, 1.2×10^{14} W/cm^2, and 2.1×10^{14} W/cm^2 respectively.

4.5 FLUCTUATIONS AND ERRORS

Many of the pictures presented in this Chapter were produced by averaging a number of far-field images together. This was done by numerically averaging electronic images from single shots. The averaging significantly improved the signal-to-noise ratio of the data. Background signal was removed by subtracting an average of a few images of shots taken under the same conditions but with no gas in the target. Fig. 4.12 shows the angular profile of the 13th harmonic obtained from a single shot in Xe at 0.3 Torr. The laser intensity for this shot was approximately 7×10^{13} W/cm^2. The 1μm grating was used for this measurement. However, the detector was configured in the manner usual for the 0.2μm grating. This included a relatively narrow slit of 200μm which caused each harmonic line to have a width of ~400μm at the detector. This is in contrast with other data taken using the 1μm grating for which the harmonic lines had a width of 1.5mm at the detector. Wider lines improve the signal-to-noise ratio for a single shot as can be seen by comparing Fig. 4.12 to the 13th harmonic in Fig. 4.1 which was obtained with similar conditions.

Fig. 4.13 shows a superposition of harmonic profiles from 5 different shots for the same conditions as in Fig. 4.12. All of the lines show the 13th harmonic. The typical amount of fluctuation in the data is evident. Fig. 4.14 shows the 13th harmonic profile obtained from an average of approximately 20 images. As can be seen, the signal to noise ratio is greatly improved. The laser intensity for all of the shots falls within the window defined by 7×10^{13} W/cm^2±15%. A similar window was used to select shots of equivalent intensity for the data averages shown throughout this chapter.

One source of noise in the harmonic images is randomly scattered light which reaches the detector. Defects in the transmission grating can cause the harmonic light to be scattered. Also, plasma generation on the slit or grating can cause noise from light and charged particles which reach the detector. In addition, if the target gas is strongly ionized, recombination light can produce significant noise at the detector. Fig. 4.15 shows the profile of the noise between the 13th and 15th harmonic lines on the detector for the same 20 shot average as in Fig. 4.14. This strip of background noise was sampled in the same way as the harmonic lines, using a strip of CCD pixels of equal width. A comparison of Figs. 4.14 and 4.15 reveals that the wings seen in the far-field profile are far above the noise level. The small structure seen on the curve in Fig. 4.14 cannot be important since it is on the same scale as the noise in Fig. 4.15.

Because of the cylindrical symmetry in the experimental setup, it is expected that the harmonic far-field profiles be symmetric about the laser axis. The much of the small structure in Fig. 4.14 is not symmetric with respect to the origin. Fig. 4.16 shows the curve of Fig. 4.14 superimposed on a reflected version of itself. The reflection takes place with respect to the vertical axis through θ=0. The coarser features which are preserved in the reflection are the ones which can be taken seriously. In this image, the wings show a definite two-tier structure.

For Figs. 4.4 and 4.6, the pressure was adjusted to avoid detector saturation. To compensate, the measured harmonic signal was scaled according to the square of the pressure. As can be seen in Fig. 4.3, the harmonic signal deviates from this scaling law by about 25% over the range of pressures used in the experiment. Thus, this scaling technique introduces only a small error between the higher and lower harmonic signal levels in Figs. 4.4 and 4.6 The data in these figures was taken using the 0.2μm grating. As mentioned before, this grating attenuates the lower harmonics relative to the higher harmonics. A comparison between harmonics obtained with the 0.2μm and the 1μm gratings gave the following attenuation factors: 4.1, 3.8, 3.0, 2.5, and 1.5 for harmonic orders 11th through 19th respectively. The signals in Figs. 4.3, 4.4, and 4.6 were multiplied by the appropriate attenuation factors to compensate for this error. For the 21st harmonic and above, there was no apparent attenuation.

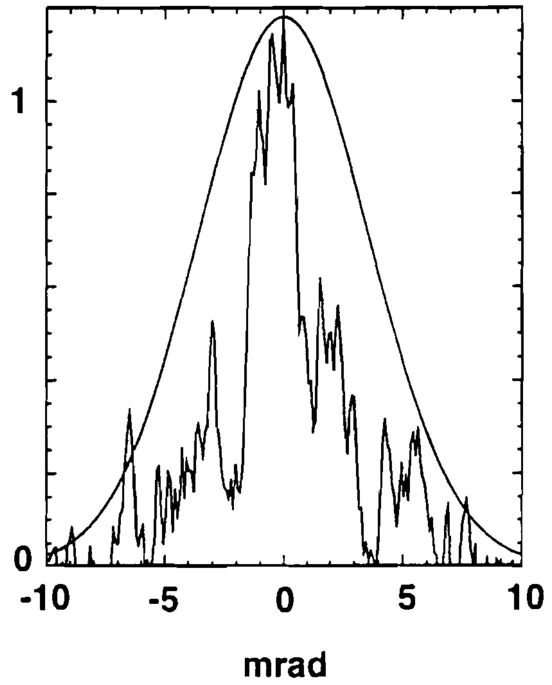

Fig. 4.12 The angular profile of the 13th harmonic obtained from a single shot in Xe at 0.3 Torr and 7×10^{13} W/cm^2. The laser profile is depicted for comparison.

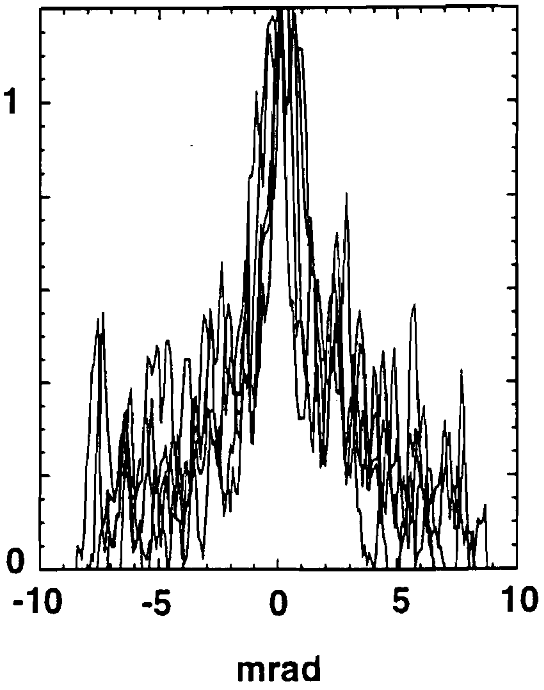

Fig. 4.13 A superposition of harmonic profiles from 5 different shots for the same conditions as in Fig. 4.12. Each curve is for the 13th harmonic.

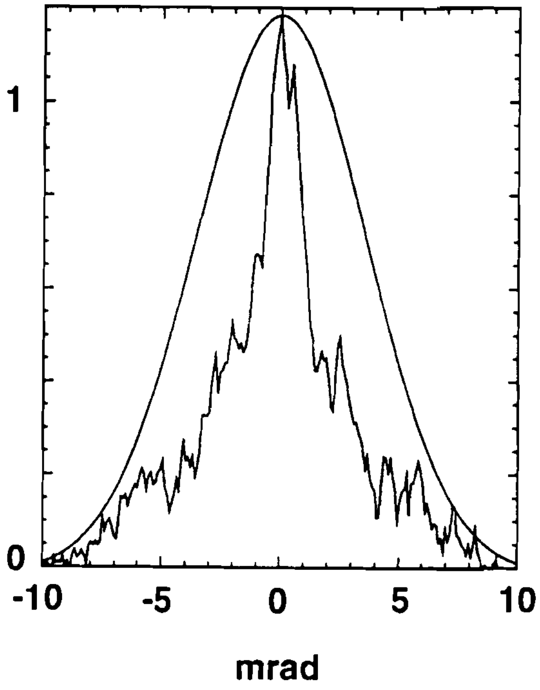

Fig. 4.14 The 13th harmonic profile obtained from an average of approximately 20 images for the same conditions as in Fig. 4.12. The laser profile is depicted for comparison.

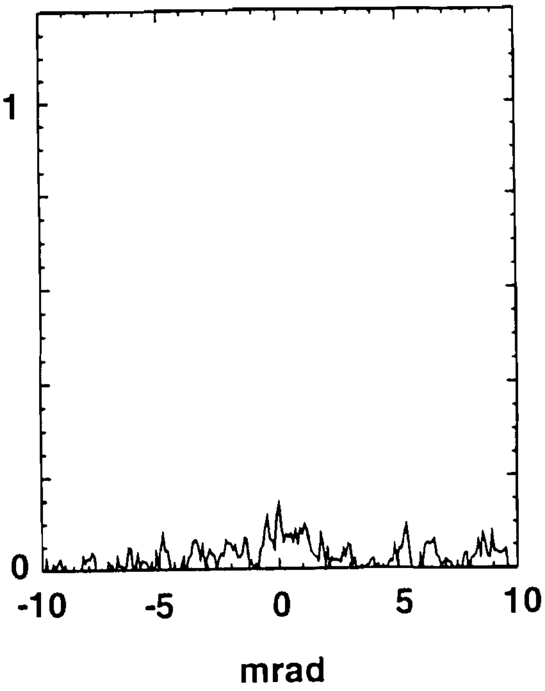

Fig. 4.15 A sampling of the noise in between the 13th and 15th harmonic lines for the same 20-shot averaged image used to generate Fig. 4.14.

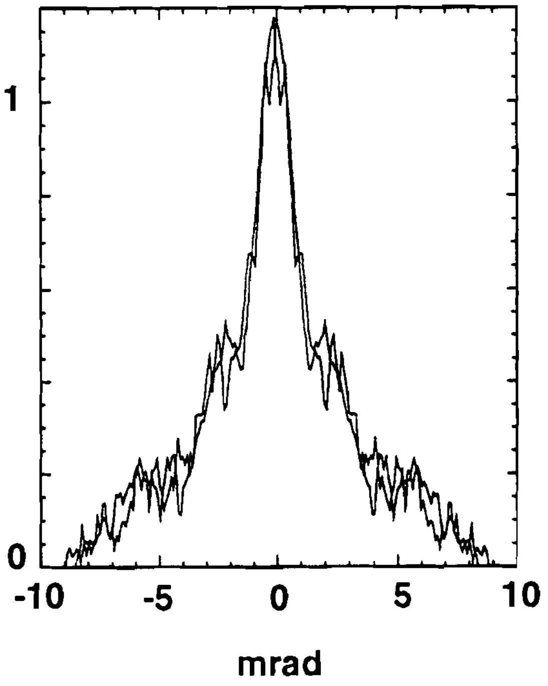

Fig. 4.16 The curve of Fig. 4.14 superimposed with a reflected version of itself.

REFERENCES

1. A. L'Huillier, X. F. Li, and L. A. Lompre, "Propagation Effects in High-Order Harmonic Generation in Rare Gases, "J. Opt. Soc. Am. B **7**, 527-536 (1990).
2. A. L'Huillier, Ph. Balcou, and L. A. Lompre, "Coherence and Resonance Effects in High-Order Harmonic Generation," Phys. Rev. Lett. **68**, 166-169 (1992).
3. Ph. Balcou and A. L'Huillier, "Phase-Matching Effects in Strong-Field Harmonic Generation," Phys. Rev. A **47**, 1447-1459 (1993).
4. A. L'Huillier and Ph. Balcou, "High-Order Harmonic Generation in Rare Gases with a 1-ps 1053-nm Laser," Phys. Rev. Lett. **70**, 774-777 (1993).
5. L. A. Lompre, A. L'Huillier, M. Ferray, P. Monot, G. Mainfray, and C. Manus, "High-Order Harmonic Generation in Xenon: Intensity and Propagation Effects," J. Opt. Soc. Am. B **7**, 754-761 (1990).
6. A. L'Huillier, K. J. Schafer, and K. C. Kulander, "Theoretical Aspects of Intense Field Harmonic Generation," J. Phys. B **24**, 3315-3341 (1991).
7. S. Augst, D. D. Meyerhofer, D. Strickland, and S. L. Chin, "Laser Ionization of Noble Gases by Coulomb-Barrier Suppression," J. Opt. Soc. Am. B **8**, 858-867 (1991).
8. S. Augst, D. Strickland, D. D. Meyerhofer, S. L. Chin, and J. H. Eberly, "Tunneling Ionization of Noble Gases in a High-Intensity Laser-Field," Phys. Rev. Lett. **63**, 2212 (1989).

9. S. Augst, C. I. Moore, J. Peatross, and D. D. Meyerhofer, "Spatial Distribution of High-Order Harmonics Generated in the Tunneling Regime," in *Short Wavelength Coherent Radiation: Generation and Applications*, edited by P. H. Bucksbaum and N. M. Ceglio, (OSA, Monterey, CA, 1991), Vol. 11, pp. 23-27.

CHAPTER 5

RADIATION BY A COLLECTION OF DIPOLES

The radiation emitted from a collection of driven oscillating dipoles depends as much on their geometrical configuration and temporal phase relationships as on their individual oscillation amplitudes. Variations of their spatial and temporal arrangements not only influence the distribution of the radiation, but also the total emitted power. Experimental investigations into high-order harmonic generation require large numbers of atoms to attain practical signal levels. Thus, a fundamental understanding of the atomic medium's macroscopic response is essential before the individual atomic behaviors can be discovered. Indeed, it will be seen that it is exactly this macroscopic effect which allows a signal enhancement making measurements possible in the first place. This chapter outlines the general framework necessary to consider these issues. Specific application of the framework which is relevant to our experimental conditions is also made.

5.1 RADIATION FROM A TWO-DIPOLE SYSTEM

As an illustration of how the radiation emitted from a collection of dipoles can be influenced by their relative orientations, consider the simple problem of two identical dipole radiators positioned side by side. Fig. 5.1 shows a diagram of the configuration. Let the first dipole be located at the origin with its oscillation in the z-direction defined by $z_1=z_0\cos(\omega t)$. Let the second dipole be located at a distance d on the x-axis with its oscillation also in the z-direction defined by $z_2=z_0\cos(\omega t+\alpha)$. The electric field at a very distant point $\bar{r}$ due to the dipole positioned at the origin is approximately[1]

$$E_1(r,\theta,\phi) = -\frac{e\omega^2 z_o \sin\theta}{4\pi\varepsilon_o c^2 r}\cos(kr-\omega t), \tag{5.1.1}$$

and the contribution to that same point which is made by the second dipole is approximately

$$E_2(r,\theta,\phi) = -\frac{e\omega^2 z_o \sin\theta}{4\pi\varepsilon_o c^2 r}\cos\bigl(k(r-d\sin\theta\cos\phi)-\omega t+\alpha\bigr). \tag{5.1.2}$$

Eqs. (5.1.1) and (5.1.2) are expressed in the usual spherical coordinates (r,θ,ϕ). The equations employ the MKS system of units, as is the case for all equations in this thesis. Eq. (5.1.2) is an approximation valid only when $r \gg d$. The term $\left|\vec{r}-\hat{i}d\right|$ has been replaced by r in the denominator, and by $r-d\sin\theta\cos\phi$ in the cosine argument. Let the point $\vec{r}$ be so distant relative to the dipole separation d that the electric field polarization from each dipole is virtually identical. Thus, the total electric field at point $\vec{r}$ can be taken as the sum $E_{tot}=E_1+E_2$. The time-averaged field intensity at position $\vec{r}$ is

$$I(r,\theta,\phi) = \frac{c\varepsilon_o}{2}E_{tot}^2 = \frac{e^2\omega^4 z_o^2 \sin^2\theta}{16\pi^2\varepsilon_o c^3 r^2}\bigl[1+\cos(kd\cos\phi\sin\theta+\alpha)\bigr]. \tag{5.1.3}$$

The intensity retains the dependence of all of the spatial variables so that a highly nonuniform radiation field is evident. Some regions experience an intensity enhancement due to constructive interference between the two fields. Other regions experience relatively weak intensity due to cancelations between the fields. Exactly where these occur depends strongly on d and α.

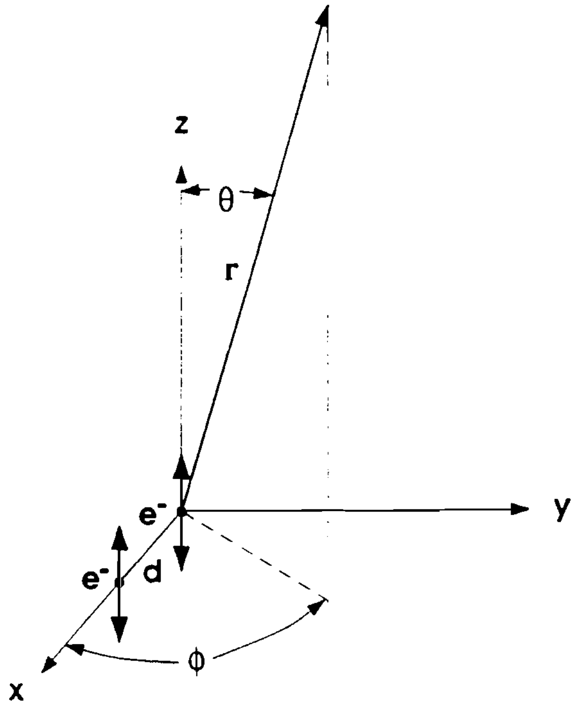

Fig. 5.1 Two identical dipole radiators positioned side by side shown with the coordinate system used.

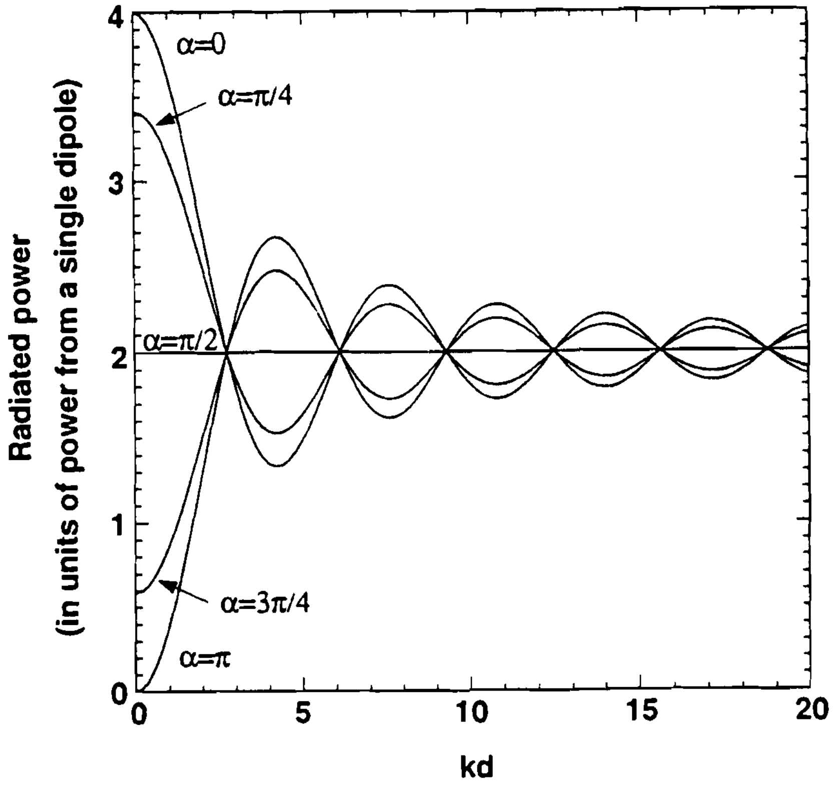

Fig. 5.2 The average power radiated from a two dipole system as a function of dipole separation for five different relative phases. The power is expressed in units of the power radiated from a single dipole.

The total average radiated power from the system can be calculated by integrating the intensity over a distant spherical surface centered about the origin. The integration can be performed analytically[2] to obtain

$$P(\alpha,d)=\frac{e^2\omega^4 z_o^2}{12\pi\varepsilon_o c^3}\left\{2+3\cos\alpha\left[\frac{\sin kd}{kd}-\frac{1}{(kd)^2}\left(\frac{\sin kd}{kd}-\cos kd\right)\right]\right\}. \qquad (5.1.4)$$

Fig. 5.2 shows a plot of the power as a function of dipole separation for several different values of relative phase α. Just as the values of d and α effect the spatial distribution of the radiation, they also effect the amount of power radiated. When the two radiators are far apart, the power emitted is simply the sum of the powers emitted from two individual dipole radiators. Closer together, however, the dipoles can emit up to twice that amount, or they may reduce their emission to zero depending on their relative phase and separation.

For this example, the oscillations of the dipoles were exactly specified. It is interesting to explore how the oscillations might differ if they resulted instead from an applied sinusoidal force. The question is whether radiative forces might significantly affect the oscillations as a function of their separation and relative phase. The answer is that the dipoles do not significantly influence each other's oscillations for parameters of experimental interest. For example, the inertial force required to cause an electron to oscillate is usually far greater than the electron's radiative self force.[3] The radiative force that two identical electron oscillators exert on each other is on a similarly small scale for parameters in the range of our experimental conditions. This is true even though the total radiated power can be strongly influenced by the relative orientation of the dipoles. It should be pointed out that, on average, the work done by the driving force in the absence of radiative forces is zero. It is only the work done against the radiative forces which is nonzero. It can be shown that the total radiated power from the two-dipole system is equal to the rate of work done by the individual radiative self forces plus the rate of work done by each dipole's field on the other dipole.

If the two dipoles in the example given above are electrons driven by a sinusoidal force with amplitude $F=-z_0 m_e \omega^2$, the dipoles will undergo the same oscillations as previously specified provided the radiative forces are negligible compared to the driving force. The radiative self force[3] that a single oscillating electron feels is $F_{self} = e^2\dddot{z}/6\pi\varepsilon_o c^3$. F_{self} can be obtained perturbatively from the equation of motion for an electron experiencing only the driving force $F\cos\omega t$. It is found that F_{self} is also oscillatory with amplitude $e^2\omega F/6\pi\varepsilon_o c^3 m_e$. For frequencies in the range of visible light, F_{self} is on the order of $10^{-8}F$. Thus, the perturbative assumption is justified. Even for frequencies in the range of x-rays, the self force is small compared to the driving force. When the two dipoles in the example are very close together, the radiative force that they exert on each other[1] has an approximate strength of $F_{self}/(kd)^3$. In a gas at 1 Torr and 300°K, the inter-atomic spacing is on average 32nm. If d is taken to be this distance, then for optical frequencies, $1/(kd)^3$ is about 10^2 which falls short of the factor of 10^8 required to distort the oscillations. Thus, the individual oscillations of the two dipoles are virtually unaffected by the fact that they are members of a group.

A similar situation arises in high-harmonic generation in low density gases. An applied laser field stimulates the atoms which induces bound electrons to oscillate at frequencies which are harmonics of the laser frequency. The motions of the electrons in the individual atoms are determined exclusively by the applied laser field. As in the example above, the electron motions are not significantly influenced by harmonic emission from neighboring atoms.[4-6] Thus, the response of each atom to the driving field is decoupled from the responses of the other atoms. This is an important point which makes possible the extraction of single-atom information from the radiation emitted from a large group of atoms.

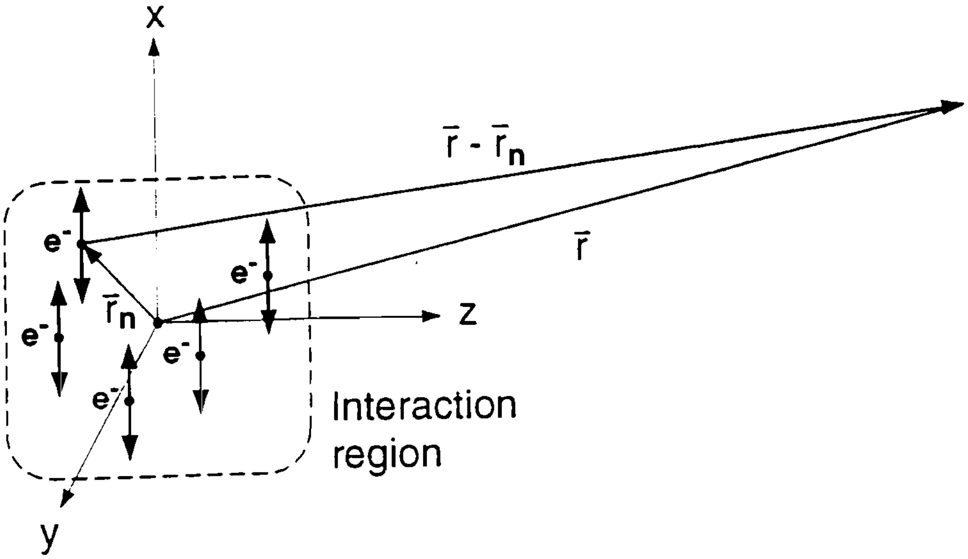
x
$\bar{r} - \bar{r}_n$
$\bar{r}$
e^-
e^-
$\bar{r}_n$
z
e^-
e^-
e^-
Interaction region
y

Fig. 5.3 A collection of dipole emitters which radiate into the surrounding space shown with the coordinate system used.

5.2 HARMONIC GENERATION IN A MANY-DIPOLE SYSTEM

Harmonic generation experiments are performed with large collections of atoms. The medium is driven by an applied electric field oscillating at a frequency ω. As the bound electrons respond to the field, they can oscillate with frequency components which are harmonics of the applied field frequency. Each harmonic frequency component in the emission from the medium can be considered separately. In other words, the total average power emitted from the medium equals the sum of the average power emitted at each harmonic frequency. Thus, it is appropriate to consider a collection of dipoles, stimulated in some manner, emitting radiation at a single frequency.

To find the electric field at a point in space due to a large collection of dipoles, the same procedure as employed in the previous section may be used. That is, the contribution from each dipole with its unique position, phase, and strength can be summed to give the total electric field at a distant point. As was previously discussed, the influence of each dipole's radiation on its neighbors may be ignored. For simplicity, let all of the dipoles be oriented parallel to one another (say along the x-direction), and let the point in question $\vec{r}$ be far outside the atomic medium so that the polarization of the field contribution from each dipole is the same. In addition, let the atomic medium have low enough density that the harmonic radiation can be considered to travel at speed c. These assumptions are well maintained for the experimental conditions employed in this work. Fig. 5.3 gives a schematic of the situation. The electric field at position $\vec{r}$ can be constructed beginning with the expression for the radiation emitted from a single dipole [see Eq. (5.1.1)], and by summing over all dipoles in the region. The summation can be written as

$$
\begin{aligned}
E_q(\vec{r},t) = \frac{eq^2\omega^2}{8\pi\varepsilon_o c^2} \sum_n \frac{\left|\hat{e}_r \times \hat{i}\right|}{\left|\vec{r}-\vec{r}_n\right|} \, x_{n,q}\left(t-\frac{\left|\vec{r}-\vec{r}_n\right|}{c}\right) \\
\times \exp\left[ik_q\left|\vec{r}-\vec{r}_n\right| - iq\omega t + i\alpha_{n,q}\left(t-\frac{\left|\vec{r}-\vec{r}_n\right|}{c}\right)\right] + \text{C.C.}
\end{aligned}
\tag{5.2.1}
$$

where $\hat{e}_r$ is a unit vector in the direction of $\vec{r}$ (approximately the same as $\vec{r}-\vec{r}_n$), and $x_{q,n}$ and $\alpha_{q,n}$ are the oscillation amplitude and phase for the nth dipole. The subscript q on the electric field specifies and elsewhere the field component with harmonic frequency $q\omega$ where ω is the frequency of a driving field. Eq. (5.2.1) is valid only when r is much larger than the region containing the dipoles. The interaction region is assumed to be near the origin. For a very large number of identical electric dipoles, the summation can be done as an integral over the region of space containing the dipoles. Thus we have,

$$
\begin{aligned}
E_q(\vec{r},t) = \frac{eq^2\omega^2}{8\pi\varepsilon_o c^2} \int d^3r' \frac{N_o(\vec{r}')}{\left|\vec{r}-\vec{r}'\right|} \left|\hat{e}_r \times \hat{i}\right| x_q\left(\vec{r}',t-\frac{\left|\vec{r}-\vec{r}'\right|}{c}\right) \\
\times \exp\left[ik_q\left|\vec{r}-\vec{r}'\right| - iq\omega t + i\alpha_q\left(\vec{r}',t-\frac{\left|\vec{r}-\vec{r}'\right|}{c}\right)\right] + \text{C.C.}
\end{aligned}
\tag{5.2.2}
$$

where N_o is the dipole volume density. To perform the integral, the spatial and temporal dependence of x_q and α_q must be known. These, of course, depend on how the dipole medium is stimulated and how the individual dipoles respond to the stimulus. For harmonic generation experiments, the stimulus is provided by a laser field which has a well known spatial and temporal distribution. For our conditions, the electron oscillations depend entirely on the individual atomic responses to the laser field. However, the response of the entire system depends on the configuration of the medium relative to the laser.

5.3 HARMONIC EMISSION INDUCED BY AN APPLIED FIELD

In the case of experimental harmonic generation, the dipole medium is stimulated by an oscillating electric field. Two important driving fields are gaussian and plane wave laser fields. In cylindrical coordinates, they can both be written as[7]

$$\vec{E}(\rho,z,t)=\hat{i}\frac{1}{2}E_0\left\{t-\frac{z}{c}\left(1+\frac{\rho^2}{2R(z)}\right)\right\}f(\rho,z)\exp\left\{i\left(kz-\omega t+\alpha(\rho,z)\right)\right\}+\mathrm{C.C.} \qquad (5.3.1)$$

where for a plane wave

$$f=1,\ \ \alpha=0,\ \ R=\infty, \qquad (5.3.2)$$

and for the gaussian laser field

$$f(\rho,z)=\frac{w_0}{w(z)}e^{\frac{-\rho^2}{w^2(z)}} \quad \text{and} \quad \alpha(\rho,z)=\frac{k\rho^2}{2R(z)}-\tan^{-1}(z/z_0). \qquad (5.3.3)$$

ρ and z are the usual cylindrical coordinates. The width of the gaussian laser beam is defined by $w(z)=w_0\sqrt{1+z^2/z_0^2}$, where w_0 is the radial distance from the laser focus to where the electric field decreases by a factor of e, and z_0 is the Rayleigh range defined as the distance along the z-axis from the focus to where the field decreases by a factor of $\sqrt{2}$. Their values are $w_0=2\lambda f^{\#}/\pi$ and $z_0=\pi w_0^2/\lambda$, where $f^{\#}$ is the ratio between the distance to the focus from the lens and the beam diameter (1/e) at the lens. The term $R(z)\equiv z+z_0^2/z=z_0^2w^2(z)/w_0^2z$ is identified with the radius of curvature of the laser beam wave front.

The field defined by Eq. (5.3.1) can be substituted into Eq. (5.2.2) to yield the response of the dipole medium to the driving field. The phase of each dipole's emission is determined from the phase of the laser as well as from the the dipole's individual response. Thus, α_q of Eq. (5.2.2) is written as $\alpha_q(\rho',z') = qk_1z' + q\alpha(\rho',z') + \nu_q$, where ν_q is the difference between the dipole phase and q times the local phase of the laser. The last term is unimportant unless it varies during the laser pulse. As is proposed in this thesis, ν_q indeed can have a very strong dependence on the laser field strength, and this is the primary cause of broad wings observed in the harmonic far-field patterns. We consider the oscillation amplitude x_q and phase ν_q to depend adiabatically on the local instantaneous field amplitude and not on the past history of the field. The result of the substitution is

$$E_q(\bar{r},t) = \frac{eq^2\omega^2}{8\pi\varepsilon_o c^2}\int d^3r'\mathcal{N}_o(\bar{r}')\frac{|\hat{e}_r \times \hat{i}|}{|\bar{r}-\bar{r}'|}x_q\left\{E_o\left[t-\frac{|\bar{r}-\bar{r}'|+z'-\rho'^2/2R(z')}{c}\right]f(\rho',z')\right\}$$
$$\times\exp\left[ik_q|\bar{r}-\bar{r}'|+iqk_1z'-iq\omega t+iq\alpha(\rho',z')+i\nu_q\right]+\mathrm{C.C.} \qquad (5.3.4)$$

It has been assumed in Eq. (5.3.4) that the driving field is not significantly affected by the harmonic interaction. However, the wave number k_1 can in principle depend on the local optical index of the atomic medium. The spatial variation of this dependence must be weak so that the driving field does not experience defocusing such as described in Section 2.3. By contrast for the high harmonics ($q \geq 11$), k_q is assumed not to depend on the atomic medium at all, and is taken to be $q\omega/c$.

The propagation direction of the driving field, which enters into the phase of the dipole emission [qk_1z' enters into $\alpha_q(r',z')$], causes the harmonic field to have a similar propagation direction. This can be seen easily by observing that the term $\exp\left[ik_q|\bar{r}-\bar{r}'|+iqk_1z'\right]$ in Eq. (5.3.4) is strongly oscillatory unless $|\bar{r}-\bar{r}'| \cong z-z'$.

Thus, the overwhelming portion of the harmonic emission comes out along the z-axis in the forward direction. Although the field emission in the other directions is not exactly zero, it is very nearly so compared with the field emission in the forward direction. This fact allows for the following simplifying approximations which may be applied to Eq. (5.3.4):

$$\left|\hat{e}_r \times \hat{i}\right| \cong 1 \ , \quad |\bar{r} - \bar{r}'| \cong z - z' + \frac{\rho^2(1+z'/z) + \rho'^2 - 2\rho\rho'\cos(\phi-\phi')}{2z}. \tag{5.3.5}$$

If the interaction region is small compared to the distance r, then $|\bar{r} - \bar{r}'|$ in the denominator may be approximated as r, and $\exp\left\{i k_q \rho'^2/2z\right\}$ may be set equal to one, the Fraunhofer approximation.[8] If, in addition, the interaction region is located very near the laser focus, then within the temporal pulse envelope of the field, $|\bar{r} - \bar{r}'|$ is approximately equal to $z - z' + \rho^2/2z$, giving an envelope of $E_o\left[t - \left(z + \rho^2/2z\right)/c\right]$ which is independent of the variables of integration. This can be properly done provided the neglected terms within the field envelope are all small compared to the pulse duration τ. Specifically, the following conditions must be satisfied:

$$\rho'^2/2\left(z' + z_o^2/z'\right) \ , \quad z'\rho^2/2z^2 \ , \quad \rho'\rho/z \ , \quad \rho'^2/2z \quad << c\tau. \tag{5.3.6}$$

Experimentally, these conditions often hold very well. Neglecting the terms implies that all emission which arrives at point $\bar{r}$ at a given moment come from dipoles which were experiencing the same portion the laser temporal envelope. Finally, if $N_o(\bar{r}')$ has azimuthal symmetry so that it can be written as $N_o(\rho', z')$, then the only angular dependence inside the integral of Eq. (5.3.4) comes from the last exponent [note the approximation in Eq. (5.3.5)]. The azimuthal integration can be performed analytically as

$$\int_0^{2\pi} d\phi' \exp\left\{-i\frac{k_q \rho\rho'}{z}\cos(\phi-\phi')\right\} = 2\pi J_o\left(\frac{k_q \rho\rho'}{z}\right). \tag{5.3.7}$$

All together, the approximations of Eqs. (5.3.5) - (5.3.7) when inserted into Eq. (5.3.4) yield

$$\begin{aligned} E_q(\vec{r},t) = \frac{eq^2\omega^2}{4\varepsilon_o c^2 r} e^{ik_q r - iq\omega t} \int \rho' d\rho' dz' \mathcal{N}_o(\rho',z') x_q\{E_o[t-r/c] f(\rho',z')\} J_o\left(\frac{k_q \rho\rho'}{z}\right) \\ \times \exp\left\{-i\Delta k z' + ik_q z'\rho^2/2z^2 + iq\alpha(\rho',z') + i\nu_q\right\} + \text{C.C.} \end{aligned} \tag{5.3.8}$$

where $r = \sqrt{z^2+\rho^2} \cong z + \rho^2/2z$, and $\Delta k = k_q - qk_1$. The collection of points in the far-field with fixed r defines a spherical wave front. Fig. 5.4 gives a schematic of the situation described in Eq. (5.3.8). Eq. (5.3.8) is referred to as the phase-matching integral because it describes how the collection of dipole emitters cooperate in creating the radiative field.

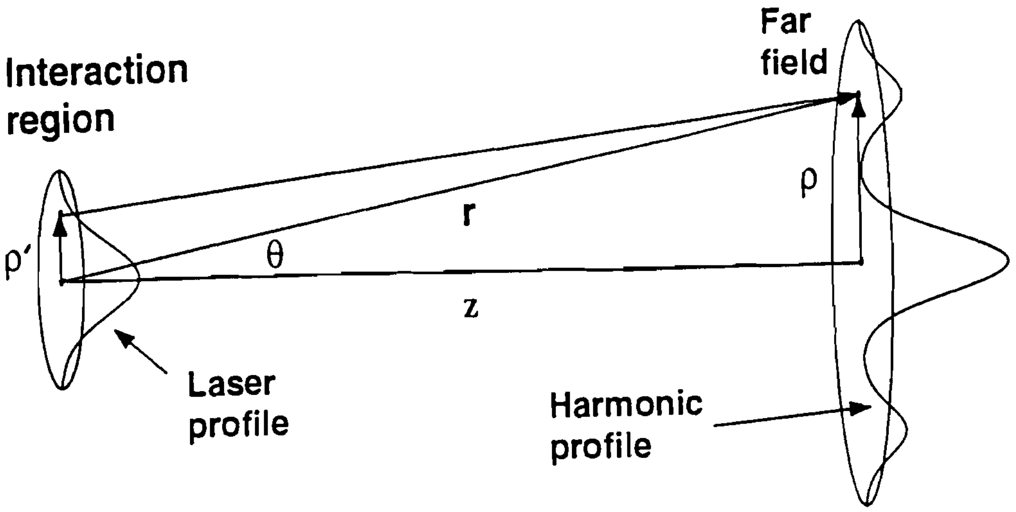
Interaction region
Far field
ρ'
θ
r
ρ
z
Laser profile
Harmonic profile

Fig. 5.4 A schematic depicting the propagation of laser harmonics into the far field.

Δk of Eq. (5.3.8) is a constant only if the dipole density distribution is uniform throughout the interaction region. However, in general this is not the case. The medium density can vary spatially causing qk_1-k_q to be different throughout the interaction region. In addition, if ionization of the medium occurs during the interaction, the resulting free electrons can change the value of k_q-qk_1. This is particularly complicated because the electron density not only varies with position but also with time. To include these effects correctly, $\Delta kz'$ must by replaced by[4,9,10]

$$\Delta kz' \equiv \int_{-\infty}^{z'} dz'' \Delta k(\rho', z'', t). \tag{5.3.9}$$

In the case of ionization, the density of the medium must also be considered to be a function of time and written as $N_o(\rho', z', t)$.

In general, Δk is nonzero because light of different frequencies travels at different velocities in any material. When the harmonics and the laser propagate through the medium, their phases become mismatched so that harmonics created in different regions interfere. High-harmonic generation experiments are often performed using the noble gases. The phase mismatch in these gases is usually unimportant at pressures less than 10 Torr. However, if the gas undergoes ionization, a much stronger phase mismatch can occur due to the presence of free electrons. Δk is given by $q\omega(n_q$-$n_1)/c$, where n_l and n_q are the indexes of refraction for the laser and the harmonic. For high-order harmonics ($q \geq 11$), n_q is approximately 1 for conditions of interest in this thesis. For a fully ionized gas at 1 Torr (1 electron per atom), 1-n_1 is 1.6×10^{-5} assuming λ=1054nm [see Eq. (2.3.3)]. Table 5.1 gives the phase mismatch (Δkz) associated with propagation though neutral Xe and through an ionized gas as a function of harmonic order.[4] The gas pressure is chosen to be 1 Torr, and the propagation distance is 1mm.

q	3	5	7	9	11	13	15	17	19	21
Xe	$.0003\pi$	0.002π	0.007π	0.05π	-0.01π	-0.03π	-0.04π	-0.05π	-0.05π	-0.05π
elect.	0.09π	0.16π	0.22π	0.28π	0.36π	0.41π	0.47π	0.53π	0.60π	0.66π

Table 5.1 The phase mismatch associated with propagating though 1mm of neutral Xe and a fully ionized gas (1 electron per atom). The values are calculated at 1 Torr and 300°K, and the fundamental wave length is 1054nm.

High-order harmonic generation experiments have often been carried out by focusing a laser into a jet of gas at a pressure of 10 Torr or more [see Refs. 1-6 of Chapter 3]. If during the interaction the gas strongly ionizes, the phase mismatch can be severe. For example, the phase mismatch for the 21st harmonic of 1054nm light traveling 1mm through 10 Torr of a singly ionized gas is 7π. Under such conditions, the path of the laser beam itself can become significantly distorted as discussed in Section 2.3. To keep the phase mismatch for 1mm of propagation below π, the pressure of the ionizing gas should be about 1 Torr or less (see bottom row of Table 5.1).

5.4 APPLICATION OF THE PHASE-MATCHING INTEGRAL

High harmonics emitted from different locations in the interaction region can have mismatched phases due to a number of reasons. One source of phase mismatch is the frequency-dependent refractive index of the interaction medium as discussed above.

Phase mismatches can also arise from the geometry of the interaction medium and the laser field. This includes phase mismatches associated with the strong diffraction associated with a laser focus. Phase mismatches not only reduce the efficiency with which harmonics are produced, but they can also affect the angular distribution of the emission in complicated ways. For high harmonic generation, it is difficult to create a situation where phase mismatches from all sources completely offset one another. Thus, the approach used in this work has been to minimize all of the different sources of phase mismatch. This is accomplished through the use of a thin, low-density gas distribution. This section provides insight into how the thickness of the atomic medium influences the angular distribution of the harmonics. It is established in this section and in Appendices B and C that for our conditions the harmonic far-field patterns can be thought of as emerging from a plane in the interaction region. At the same time a number of possible sources for the broad wings observed in the harmonic profiles are eliminated.

5.4.A Harmonic Generation by a Plane Wave Incident on a Cylindrical Medium

Consider the $q^{\underline{th}}$ harmonic generated by a plane wave incident on a cylinder of radius ρ_o and length ℓ. For simplicity, we consider a uniform density N_o. Fig. 5.5 shows a diagram of the setup. From Eqs. (5.3.2) and (5.3.8), the harmonic electric field at a point in the far-field is

$$E_q(\rho,z)=\frac{eN_o q^2\omega^2 x_q}{4\varepsilon_o c^2 r}e^{ik_q r-iq\omega t}\int_0^{\ell} e^{-i\Delta kz'+i\frac{k_q\rho^2}{2z^2}z'}dz'\int_0^{\rho_o}\rho' d\rho' J_o\left(\frac{k_q\rho\rho'}{z}\right)+\text{C.C.} \quad (5.4.1)$$

Recall that $r=\sqrt{\rho^2+z^2}$. By performing the integration and solving for the intensity, we find

$$I_q(\rho,\theta)=\frac{e^2q^4\omega^4x_q^2N_o^2\rho_o^4\ell^2}{32\varepsilon_o c^3r^2}\left[\frac{2J_1(k_q\rho_o\theta)}{k_q\rho_o\theta}\,\frac{\sin\left(\ell\left[\Delta k-k_q\theta^2/2\right]\right)}{\ell\left[\Delta k-k_q\theta^2/2\right]}\right]^2 \tag{5.4.2}$$

where $\rho/z\equiv\sin\theta\equiv\theta$. As expected, the intensity of the harmonic depends on the square of the cylinder length ℓ and the square of the density N_o. The square of the factors inside the brackets ranges between 0 and 1. The first or the second factor can dominate the angular profile depending on the length of the cylinder. The first factor describes the far-field angular pattern from a circular aperture. It contains the radial information of the emission from the interaction region. The second factor depends on the length of the cylinder. When ℓ is large enough, the term introduces a radial distortion which obscures the angular profile of the circular aperture. Fig. 5.6 shows the far-field distribution of the harmonic intensity for several different values of ℓ ranging from $k_q\rho_o^2/2$ to $8k_q\rho_o^2$. Eq. (5.4.2) is plotted for two different values of Δk. All factors outside of the brackets of Eq. (5.4.2) are ignored.

The fact that the far-field angular profile is sensitive to the cylinder length illustrates the principle that a thinner interaction region (ℓ small) makes the interpretation of the far-field profile less complicated. That is, if the interaction region is thin enough, the harmonic emission can be thought of as emerging from a single plane. For the example of the cylinder, the far-field profile is that given by a circular aperture when $\ell<\lambda/(2q\theta^2)$ [see sine term in Eq. (5.4.2)]. This criterion can be used to give a simple estimate of how thick the interaction region can be before the far-field angular profile is strongly affected. For our conditions (ℓ=1mm, λ=1054nm, q=13), the criterion is violated for θ ≥ 7 mrad. The angular widths of the harmonic profiles presented in this thesis lie more or less within this range. Thus, complications arising from a thick medium were avoided.

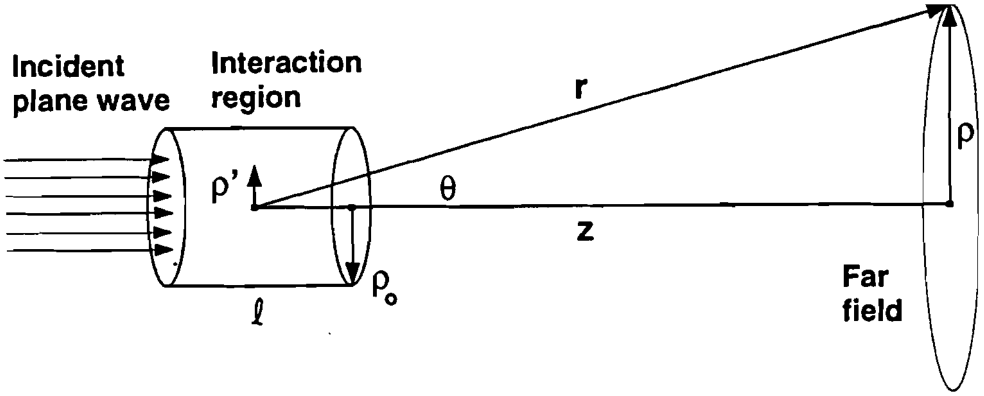
Incident plane wave
Interaction region
r
ρ'
θ
z
ρ
ρ₀
ℓ
Far field

Fig. 5.5 A schematic of a plane wave laser field incident on a cylindrical harmonic generation medium.

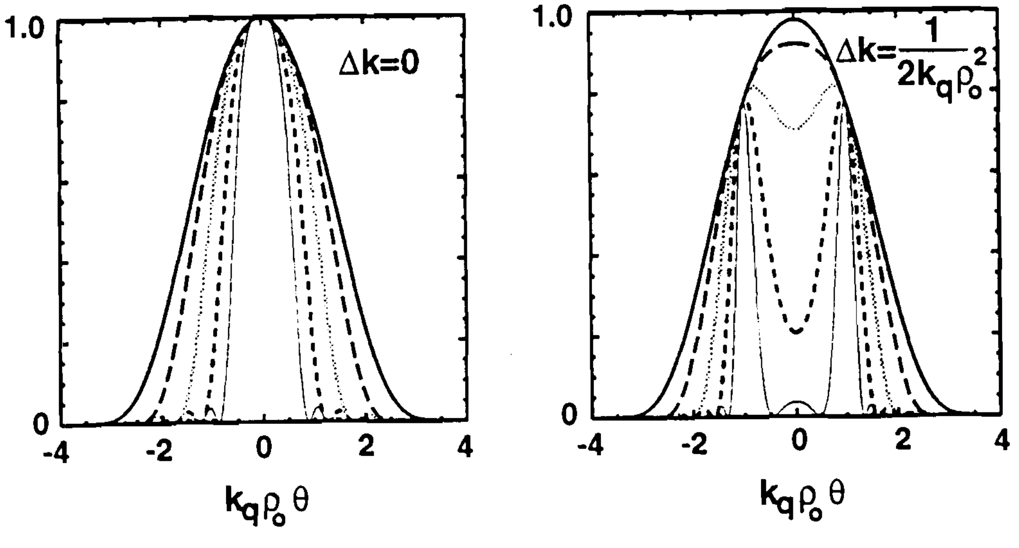

Fig. 5.6 The far-field patterns for harmonic generation by a plane wave in a uniform cylindrical medium. The thickness of the medium ℓ is 1/4 (thick solid), 1/2 (dashed), 1 (dotted), 2 (dash-dot), and 4 (thin solid) times $2k_q\rho_o^2$. The left plot shows the case Δk=0, and the right plot shows the case $\Delta k = 1/2k_q\rho_o^2$.

5.4.B Harmonic Generation by a Focused Laser in a Thin Medium

Consider harmonic emission from a single plane positioned at the laser focus. Because the laser intensity varies radially, the harmonic emission also varies radially. The radial profile of the laser field in the focus, as seen from Eq. (5.3.3), is

$$E(\rho') = E_o \exp\left\{-\rho'^2/w_o^2\right\}. \tag{5.4.3}$$

For simplicity, assume that the strength of emission for the qth harmonic is proportional to the laser field raised to a power p. For perturbation theory, this assumption is exactly correct if we take p=q. In the range of the harmonic plateau, where high harmonic emission depends more gradually on the laser field, the emission is approximately modeled with p<<q. Under this assumption, the radial profile for a given harmonic in the laser focus is

$$E_q(\rho') \propto E_o^p \exp\left\{-p\rho'^2/w_o^2\right\} \tag{5.4.4}$$

This profile creates a gaussian beam with waist $w_{oq} = w_o/\sqrt{p}$. Note that this model implies that the phase of the harmonic is the same throughout the focal plane. The Rayleigh range of the harmonic beam is $z_{oq} = q\,z_o/p$. As the beam propagates, its radius is given by $w_q(z) = w_{oq}\sqrt{1 + z^2/z_{oq}^2}$. In the far field, the radius becomes

$$w_q(z) = w_{oq}z/z_{oq} = \left(\sqrt{p}/q\right)\left(w_o z/z_o\right). \tag{5.4.5}$$

This shows that the width of the harmonic far-field profile is $q/\sqrt{p}$ times narrower than the laser field. For example, if q=19 and p=4, the harmonic profile is approximately 10 times narrower than the laser beam.

The very narrow far-field patterns predicted by this model are inconsistent with the broad wings observed in the data. Appendix B extends this analysis to 3 dimensions to include the effect of a finite interaction region thickness. When the interaction region is thick relative to the laser confocal parameter, this model can produce broad structures in the harmonic far-field patterns. However, it is clearly shown for this model under our conditions, that the harmonic far-field profiles are approximately the same as if generated in a single plane.

As pointed out near the end of Section 5.3, a phase mismatch due to ionized free electrons is not very severe for our operating pressures. However, when a portion of the interaction region ionizes, diffraction of the harmonics can result from the lack of emission in the ionized portion. Because the size of the ionized portion varies in time, the diffraction can in principle create broad structures in the far field profile. Appendix C investigates this issue, using as a basis the harmonic emission model described in Appendix B. The ionization rate is assumed to follow a simple power law. The results of the calculation show that under our conditions, the effects of ionization cannot explain the broad wings observed in the experiments.

The term $\tan^{-1}z'/z_0$, contained in $\alpha(\rho',z')$ of Eq. (5.3.3), has a strong effect on the phases of harmonic light emitted in different regions of the laser focus. Because the term is independent of radius, it does not effect the angular profile of the harmonic emission, but only the overall amplitude. If the assumption is made that once a harmonic is created it propagates as a gaussian beam having the same Rayleigh range as the fundamental beam (true for $p=q$ in the model above), then the phase mismatch between harmonic light emitted from points z_1 and z_2 is

$$(q-1)\left[\tan^{-1}(z_2/z_o)-\tan^{-1}(z_1/z_o)\right] \qquad (5.4.3)$$

If z_1 and z_2 are respectively $-z_o$ and $+z_o$, the phase error is $q\pi/2$. If z_1 and z_2 are $-z_o/10$ and $+z_o/10$ respectively, the phase error is $q\pi/32$.

The distance in the interaction region over which the harmonics get out of phase by a factor π is called the coherence length. Harmonic production is limited by this length because, when the interaction region is longer, the harmonic emission from different locations begins to interfere destructively. As seen above, the coherence length for the production of the 31st harmonic in a laser focus is approximately b/10, where $b=2z_o$ is the confocal parameter. For most of the data presented in this thesis, the interaction region was about the same thickness as the coherence length. This is in contrast with most other high-harmonic generation experiments in which the interaction region was many times longer than the coherence length.

5.5 EXPLANATION OF THE FAR-FIELD WINGS

The preceding section showed that propagation effects in the interaction region are insufficient to explain the broad wings observed in the experiments reported in this thesis. To explain the wings, we found it necessary to postulate that the phase of the atomic dipole depends on the laser intensity. Thus, since the laser intensity has a radial dependence, the harmonic emission from different radial positions of the interaction region can strongly interfere in the far field, creating the broad patterns seen.

As a simple test of this idea, a harmonic far-field profile was calculated wherein the emitted harmonic field was multiplied by a minus sign whenever the laser intensity was above 90% of its peak value. (In Eq. (5.3.8), ν_q was changed from 0 to π.) Other than the sign change, the emission was assumed to follow the perturbative power law. The calculation included the integration over the temporal evolution of the pulse [see Appendix C, Eq. (C.7)]. Ionization effects were not included in this calculation.

Fig. 5.7 (a) shows the emission pattern when the sign change is not included. Fig. 5.7 (b) shows the emission pattern when this single sign change is included. The strong wings caused by the phase shift are evident. Possible explanations of why harmonic emission from real atoms might exhibit a strongly intensity-dependent phase are addressed in Chapter 6.

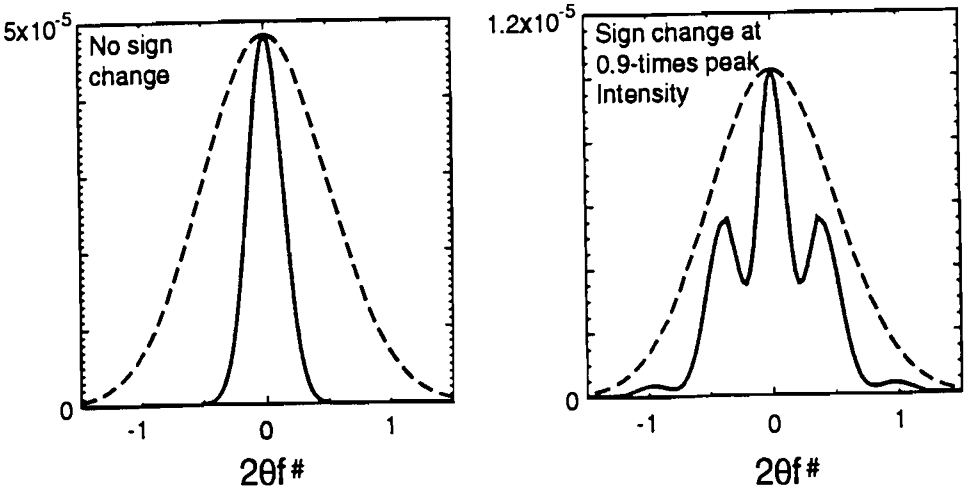

Fig. 5.7 The far-field pattern for q=13, and p=13, where (a) the phase of the harmonic emission does not change with laser intensity, and (b) the phase changed by π when the laser intensity goes above 90% of its peak value. The far-field pattern shows the cumulative energy over time. No ionization is included in this calculation.

REFERENCES

1. J. D. Jackson, *Classical Electrodynamics*, 2nd ed.(Wiley, New York, 1975), p. 395.
2. See I. S. Gradshteyn and I. M. Ryzhik, *Table of Integrals, Series, and Products*, corrected and enlarged edition, prepared by Alan Jeffrey (Academic Press, San Diego, 1980), formulas: 3.715.18, 6.682.1, and 6.682.6.
3. J. D. Jackson, *Classical Electrodynamics*, 2nd ed.(Wiley, New York, 1975), p. 784.
4. A. L'Huillier, K. J. Schafer, and K. C. Kulander, "Theoretical Aspects of Intense Field Harmonic Generation," J. Phys. B **24**, 3315-3341 (1991).
5. A. L'Huillier, X. F. Li, and L. A. Lompre, "Propagation Effects in High-Order Harmonic Generation in Rare Gases, "J. Opt. Soc. Am. B **7**, 527-536 (1990).
6. A. L'Huillier, Ph. Balcou, S. Candel, K. J. Schafer, and K. C. Kulander, "Calculations of High-Order Harmonic-Generation Processes in Xenon at 1064 nm," Phys. Rev. A **46**, 2778-2790 (1992).
7. P. W. Milonni and J. H. Eberly, *Lasers* (Wiley, New York, 1988), p. 490.
8. J. W. Goodman, *Introduction to Fourier Optics* (McGraw-Hill, New York, 1968), p. 61.
9. C. T. Rettner, E. E. Marinero, R. N. Zare, and A. H. Kung, "Pulsed Free Jets: Novel Nonlinear Media for Generation of Vacuum Ultraviolet and Extreme Ultraviolet Radiation," J. Phys. Chem. **88**, 4459-4465 (1984).
10. A. Lago, G. Hilber, and R. Wallenstein, "Optical-Frequency Conversion in Gaseous Media," Phys. Rev. A **36**, 3827-3836 (1987).

CHAPTER 6

INTENSITY DEPENDENCE OF THE DIPOLE PHASE: A CAUSE OF BROAD WINGS IN THE FAR-FIELD PROFILE

Many of the proposed mechanisms leading to high-harmonic emission by a strongly driven atom show variations in the phase as a function of laser intensity. Thus, our postulate in Section 5.5, that the dipole oscillation phase depends on the laser intensity, is consistent with the behavior one might expect from a strongly driven atom. As an illustration, this chapter shows calculations of harmonic far-field patterns generated from a strongly-driven anharmonic oscillator. The anharmonic oscillator is one of the simplest models consistent with high-harmonic emission. It includes such features as the formation of a harmonic plateau, and it exhibits a strong intensity dependence in the oscillation phase.

6.1 HARMONIC EMISSION FROM A CLASSICAL ANHARMONIC OSCILLATOR

A driven classical anharmonic oscillator has been successful in modeling harmonic generation in the perturbative regime and has often been discussed in texts on nonlinear optics.[1-3] Anharmonic oscillators are known to generate high harmonics when driven strongly.[4] While an anharmonic oscillator is not expected to model a real atom very closely, it does show qualitative agreement. The reason for examining harmonic emission from such a model and comparing it with experimental results is that it provides a useful illustration. In this sense, a simple anharmonic oscillator model is thought of as a generic representation of atomic behavior.

6.1.A Parameterization of an Anharmonic Oscillator Model

The equation of motion for a particularly simple type of classical anharmonic oscillator can be written as

$$\ddot{x} + \omega_o^2 x = F\cos\omega_L t - \beta x^3 \tag{6.1.1}$$

where β parameterizes the quartic anharmonicity, $F = eE_o/m_e$ is a measure of the strength of the driving field, and ω_o is the natural frequency of the oscillator when the anharmonicity is neglected. The motion of the oscillator can be expressed as

$$x = \sum_q x_q \cos\left(q\omega_L t + v_q\right), \tag{6.1.2}$$

where x_q is the amplitude of the qth harmonic component of the motion. As outlined in Appendix D, an approximate solution can be obtained by expanding the motion in terms of harmonic components and retaining only the most important terms. The oscillator is parameterized as a function of F by the values of ω_o and β. It is appropriate to choose values for these parameters which are plausible for an atom. We chose $\hbar\omega_o$ to be the binding potential of the atom we wished to model, and we chose β to fit the third harmonic emission, as follows.

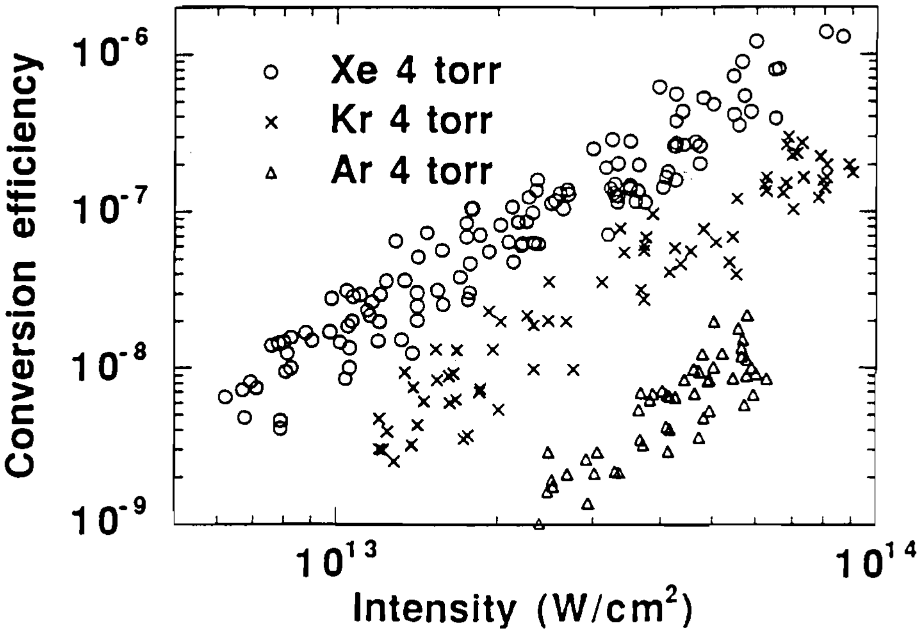

Fig. 6.1 The conversion efficiency of the laser into the third harmonic for Ar, Kr, and Xe as a function of laser intensity. The gas target thickness is 1mm and the 1.3-times diffraction limited beam is focused with f/70 optics.

Fig. 6.1 shows the measured conversion efficiency of the laser into the third harmonic for Ar, Kr, and Xe as a function of laser intensity. This data was taken by imaging the third harmonic into a CCD camera (Sony model XC-77). The response of the camera was calibrated for 532nm, and the response at 351nm (3rd harmonic) was extrapolated using a response curve provided in the camera documentation. To increase the signal, the gas distribution for all three gases was held at 4 Torr, unusually high for the gas target. The results were checked against a similar scan in Xe at 1 Torr, and the signal scaled by a factor of 16. Thus, the target seems to function reasonably well even at 4 Torr, and the measurements at this pressure are justified. The curves follow the perturbative power law of $I_3 \propto I_L^3$ which gives a slope of 2 on the log-log plot showing the conversion efficiency. The measurement shows that the 3rd harmonic follows this perturbative power law even in the intensity range where the higher harmonics experience the plateau.

The magnitude of the 3rd harmonic oscillation amplitude x_3 can be determined by calculating the total energy in the harmonic pulse. [Eq. (B.7) of Appendix B is used with p=q=3.] The total energy is

$$(\text{Energy})_3 = \pi c \varepsilon_0 r^2 \int dt \int_0^{\pi/2} |E_3(\theta,t)|^2 \theta d\theta. \tag{6.1.3}$$

The measured conversion efficiency at a given intensity is set equal to the ratio between $(\text{Energy})_3$ as calculated from Eq. (6.1.3) and the laser pulse energy. Thus, the only unknown parameter x_3, is determined. The experimental conversion efficiency must be divided by the amount that the focal spot area is larger than the diffraction limit (in our case, 1.7). This is to account for the fact that the interaction area is larger than the area implied by the diffraction-limited calculations. At a laser intensity of 1×10^{13} W/cm^2, the values for x_3 are 5×10^{-4} Å in Ar, 2×10^{-3} Å in Kr, and 4×10^{-3} Å in Xe. Based on experimental uncertainties, we estimate the error in determining these values to be a factor of 2. The parameter β is determined in the perturbative limit by setting the value of x_3 as calculated in Appendix D [Eqs. (D.3), (D.8), and (D.22) with F corresponding to 1×10^{13} W/cm^2] equal to the values of x_3 as determined above. The value for β was calculated to be 2×10^{35} (Å s)$^{-2}$ in Ar, 2×10^{35} (Å s)$^{-2}$ in Kr, and 1×10^{35} (Å s)$^{-2}$ in Xe. In each case, $\hbar\omega_0$ was chosen to be the binding potential of the atom.

With the parameters of the oscillator model fixed, the formulation of Appendix D can be used to determine x_q as a function of laser intensity. Fig. 6.2 shows the strength (absolute value) of the harmonic emission (proportional to the oscillator acceleration) calculated by the anharmonic oscillator model for Xe. The intensity range of the harmonic plateau coincides with the intensity range observed experimentally. The phase of the emission slips by a factor of π around each resonance peak, giving a strong intensity dependence to the phase of the harmonic emission [see Fig. D.1 (b) in Appendix D]. This strong phase variation as a function of laser intensity is similar to that seen in many models which describe high-harmonic emission.[5-10] It should be pointed out that the slope of 3rd harmonic as calculated by the oscillator model for intensities in the range of the plateau, is distinctly less than the perturbative-like slope which was observed experimentally.

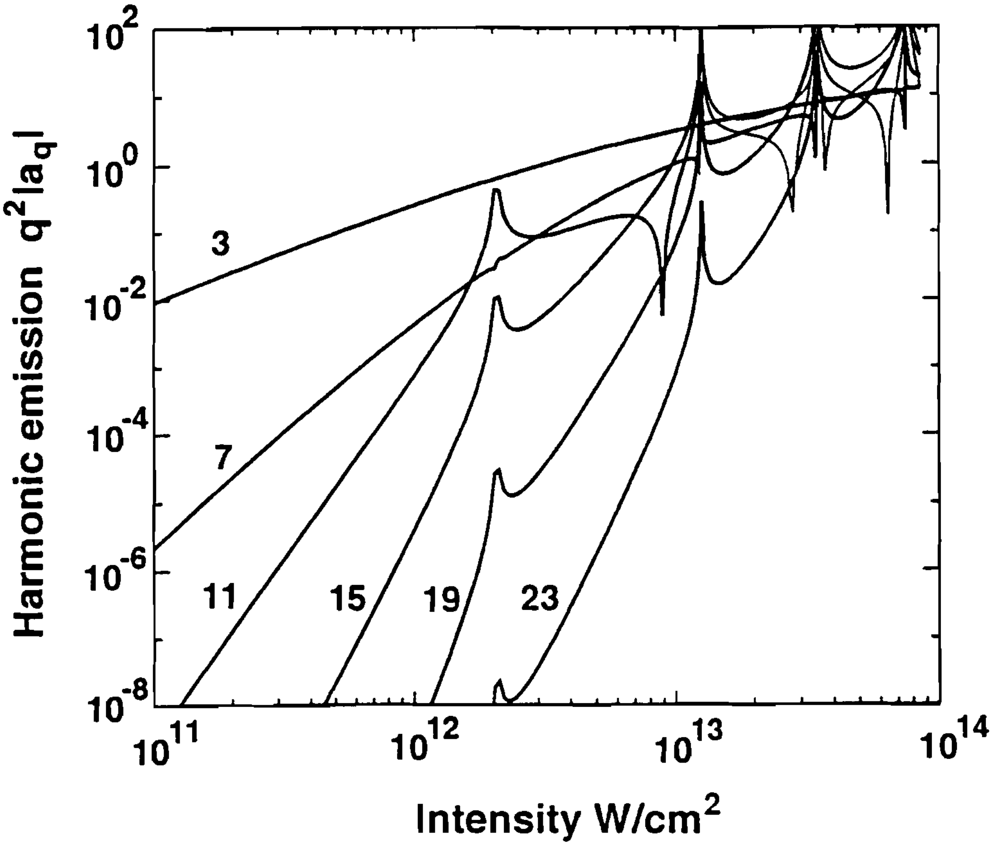

Fig. 6.2 The harmonic emission curves for different harmonic orders given by an anharmonic oscillator model parameterized to Xe.

6.1.B Far Field Patterns

The purpose for showing calculations involving an anharmonic oscillator is to illustrate the kind of behavior observed in the experiments. In particular, the phase of the dipole has a strong intensity dependence in the region of the harmonic plateau. This phase variation is sufficient to cause the broad wings observed in the far-field pattern. Fig 6.3 shows the far-field angular profiles of the harmonics as predicted by the anharmonic oscillator for Xe. The far-field pattern is calculated using Eq. (5.3.8). These calculations include the temporal integration of the pulse as described by Eq. (C.8) in Appendix C. The peak intensity was chosen to be 8.6×10^{13} W/cm^2, the value predicted by classical barrier suppression where ionization begins to occur.[11,12] It was assumed that no atoms ionize below this intensity, so the effects of ionization were not included in this calculation. The phase-matching parameters in the calculation were chosen to match experimental conditions. Broad wings which appear around a central peak contain about two to three times the energy of the peak. This is similar to what was observed experimentally.

To clearly make the point that the broad wings seen in Fig. 6.3 are caused primarily by the intensity-dependent phase, the far-field profiles were calculated again using the absolute value of the dipole response (no phase included). Fig. 6.4 shows the result of this calculation. As can be seen, the wings are significantly reduced when the intensity-dependent phase of the oscillator is ignored. The small amount of structure which remains in the wings is caused by the strong amplitude variation associated with the sharp peaks seen in Fig. 6.2. The analysis of Appendix B shows that narrow harmonic far-field patterns are expected when the strength of the emission varies smoothly with the laser intensity in the absence of phase variation. Fig. 6.4

shows that even if the emission does not vary smoothly with laser intensity, the resulting far-field structure is similarly quite narrow in the absence of phase variation.

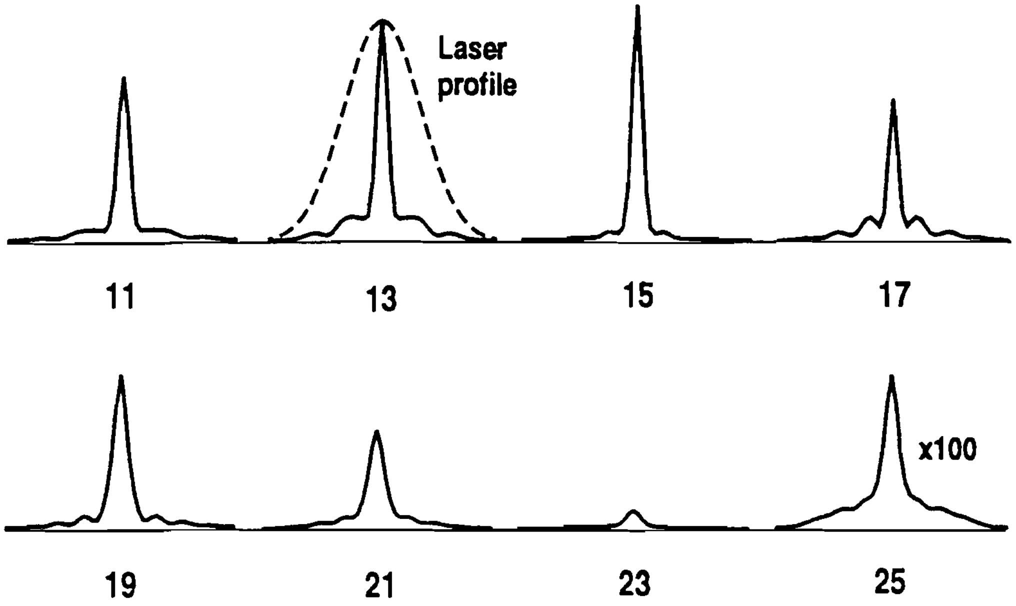

Fig. 6.3 The far-field harmonic angular profiles calculated with an anharmonic oscillator model for Xe. The phase-matching parameters are those used in experiments.

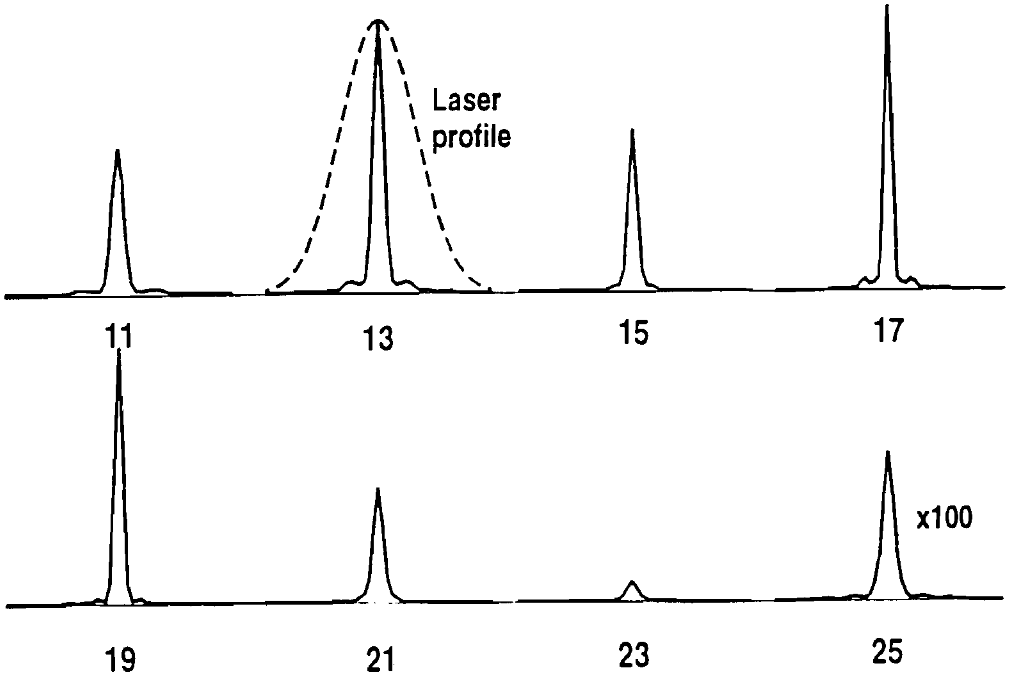

Fig. 6.4 The far-field harmonic angular profiles calculated for the identical conditions as Fig. 6.3 except that the phase of the emitted harmonics is held constant.

6.2 POSSIBLE ORIGINS OF THE INTENSITY-DEPENDENT PHASE

One possible origin of the intensity-dependent phase is the effect of AC-Stark shifted resonances. The effect of resonances on the susceptibility of low order harmonics is well known.[13] The sign can change as the frequency is tuned across a resonance. Under strong-field conditions, the atomic energy levels can be shifted into resonance by the AC-Stark effect. The effect of Stark-shifted resonances is apparent in above-threshold-ionization electron spectra (for a recent review see Ref. 14), though the effect of resonances has not been observed in ionization rates of noble gases with 1μm, 1ps laser pulses.[11,12,15] Crane et al. have observed resonant enhancements of harmonic generation in Kr.[16] Balcou et al.[17] recently invoked a π phase slip around a resonance to qualitatively explain the intensity dependence of the 7th harmonic emission in Xe. Resonances with atomic states might be expected to effect a few of the harmonics primarily, but because all of high harmonics can have intermediate resonances, this effect might show up similarly on many of the harmonics.[18]

It has been suggested that the harmonic plateau comes about when the higher-order pathways for the generation of any individual harmonic become comparable to the lowest order ones.[19] By lowest-order pathways, it is meant the processes in which each harmonic depends only on harmonics of lesser order. Higher-order pathways are the processes in which harmonics are influenced by harmonics of higher order. Such processes might be described in the following way:

$$\text{Lower order: } \hbar\omega_{q-2} + 2\hbar\omega_1 \rightarrow \hbar\omega_q, \quad \text{Higher order: } \hbar\omega_{q+2} \rightarrow 2\hbar\omega_1 + \hbar\omega_q. \qquad (6.2.1)$$

Because each pathway is independent, they need not have identical phases. In this scenario, with the onset of the plateau, brought about when higher-order processes become important, the phases of the individual harmonics should exhibit a strong intensity dependence of the driving field. All of the harmonics in the plateau could show this effect, but the effect need not be identical for each harmonic due to the different pathways. The effect of the higher-order pathways has been observed in calculations of harmonic emission from the two-level atom.[5] This is similar to the effect seen in the anharmonic oscillator model of the previous section.

Recent studies of high-order harmonic generation have suggested a quasi-classical description of harmonic generation.[6,7] The description is only applicable to harmonics close to the end of the plateau with energies well in excess of the atomic binding potential. In this scenario, after an atom is ionized, the electron follows a classical trajectory in the laser field and may collide again with the atom, releasing an energetic photon. The highest observable harmonic is approximately equal in energy to the ionization potential plus the maximum energy the electron can have when it returns to the nucleus (3 times the ponderomotive potential $e^2E^2/4m\omega^2$).[6,7] Recently, a calculation based on the same idea in which the electron trajectory is treated quantum mechanically has shown a similar cutoff.[8] The authors have pointed out that different possible electron trajectories can have different phases. Since the electron trajectories strongly depend on the laser intensity, this leads to an intensity-dependent phase of the harmonic emission. This has also been observed in the simulations based on the classical trajectories.[18]

REFERENCES

1. R. W. Boyd, *Nonlinear Optics* (Academic Press, San Diego, 1992).
2. P. W. Milonni and J. H. Eberly, *Lasers* (Wiley, New York, 1988).
3. N. Bloembergen, *Nonlinear Optics*, 2nd ed. (Benjamin, Reading, Massachusetts, 1977).
4. A. L'Huillier, L. A. Lompre, G. Mainfray and C. Manus, "Multiple Harmonic Conversion in Rare Gases in Strong Laser Fields," in *Proceedings of the 5th International Conference on Multiphoton Processes*, edited by G. Mainfray and P. Agostini, (CEA, Paris, 1990), pp. 45-55.
5. L. Plaja and L. Roso-Franco, "Adiabatic Theory for High-Order Harmonic Generation in a Two-Level Atom," J. Opt. Soc. Am. B **9**, 2210-2213 (1992).
6. P. Dietrich, N. H. Burnett, M. Ivanov, and P. B. Corkum, "High Harmonic Generation and Two Electron Ionization with Elliptically Polarized Light," Phys. Rev. Lett., submitted, (1993).
7. K. C. Kulander, K. J. Schafer, and J. L. Krause, "Dynamics of Short-Pulse Excitation, Ionization and Harmonic Conversion," to be published in the proceedings of the 3rd Conference on Super Intense Laser-atom physics, (NATO, Han-sur-Lesse, Belgium, 1993).
8. M. Lewenstein, P. Salieres, Ph. Balcou, A. L'Huillier, M.Yu. Ivanov, J. Larsson, and C.G. Wahlstrom, "Where is the Harmonic Generation Cutoff?," Phys. Rev. Lett., submitted, (1993).
9. W. Becker, S. Long, and J. K. McIver, "Higher-Harmonic Production in a Model Atom with Short-Range Potential," Phys. Rev. A **41**, 4112-4115 (1990).

10. J. J. Macklin, J. D. Kmetec, and C. L. Gordon III, "High-Order Harmonic Generation Using Intense Femtosecond Pulses," Phys. Rev. Lett. **70**, 766-769 (1993).
11. S. Augst, D. D. Meyerhofer, D. Strickland, and S. L. Chin, "Laser ionization of noble gases by Coulomb-Barrier suppression," J. Opt. Soc. Am. B **8**, 858-867 (1991).
12. S. Augst and D. D. Meyerhofer, "Ionization of Atoms with Intense Linearly and Circularly Polarized Laser Pulses," J. Phys. B, submitted, (1993).
13. N. B. Delone, V. P. Krainov, *Fundamentals of Nonlinear Optics of Atomic Gases*, (Wiley, New York, 1988)
14. R. R. Freeman and P. H. Bucksbaum, "Investigations of Above Threshold Ionization using Subpicosecond Laser Pulses," J. Phys. B **24**, 325-347 (1991).
15. T. Auguste, P. Monot, L.A. Lompre, G. Mainfray, and C. Manus, "Multiply charged ions produced in noble gases by a 1 ps laser pulse at λ=1053 nm," J. Phys. B **25**, 4181-4194 (1992).
16. J. K. Crane, S. W. Allendorf, K. S. Budil, and M. D. Perry, "Resonantly Enhanced Harmonic Generation and Above-Threshold Ionization in Krypton," in *Short Wavelength Coherent Radiation: Generation and Applications*, edited by P. H. Bucksbaum and N. M. Ceglio, (OSA, Monterey, CA, 1991), Vol. 11, pp. 28-32.
17. Ph. Balcou and A. L'Huillier, "Phase-Matching Effects in Strong-Field Harmonic Generation," Phys. Rev. A **47**, 1447-1459 (1993).
18. K. Kulander, Private Communication (1993).
19. P.L. Knight, Private Communication (1993).

CHAPTER 7

CONCLUSION

The experiments presented in this thesis are the first observations of high-order harmonics in a regime where propagation effects are unimportant. Under our conditions, the laser focusing depth and ionized free electrons cannot significantly affect the harmonic far-field emission patterns. The thin and low-density gas distribution employed in these experiments allows the harmonics to be thought of as emerging from atoms lying in a single plane in the interaction region. As discussed in Chapter 5, a narrow far-field pattern is expected under our conditions for assumptions appropriate to the harmonic plateau if the phase of the dipole emission is independent of the laser intensity. Even under conditions of strong ionization, the far-field pattern is expected to be narrow. The most important finding of this work is the occurrence broad wings which appear in the far-field pattern of nearly every high harmonic. Because other possible origins for these wings can be discounted for our conditions, we conclude that the phase of the dipole response has a strong laser-intensity dependence. Since the laser intensity varies radially in the interaction region, this intensity dependence implies a radial variation for phase of the dipole emission. Such phase variations can cause the harmonic light to interfere in the far-field, leading to broad wings in the angular profile. A strong intensity-dependent phase of the atomic dipole response is a feature common to many high-harmonic generation models.

APPENDIX A

GAS TARGET COMPUTER PROGRAM

```fortran
c Fortran Program: target.f
c
c This program tracks particles in a specific type of gas target using a
c Monte Carlo averaging technique.  The program assumes molecular flow
c with the usual boundary condition that the particles bounce of the walls
c with a cosine distribution to the surface normal.  To explore
c the limits of this model, two effects are approximated: collisions and
c non-diffuse bouncing.  The non-diffuse bouncing is modeled by having
c a given fraction of the bounces occur with a specular or mirror-like
c reflection.  This fraction is specified by the program user.  The
c collisions are modeled by a midflight redirection of the particle
c distributed randomly over two half spheres: one directed toward the
c exit and one directed away from the exit.  The program user specifies
c the probability between scattering into one or the other hemisphere.
c The mean free path is assumed to be uniform between the plates
c and uniform inside the hole.  The program user specifies
c the mean free path of the particle in the two regions.
c Once out of the hole, no collisions are modeled.  If the
c user does not want collions, they should simply enter a very long mfp.
c The collisional modeling is very crude and should only be used to
c get a very rough idea of what happens as the density increases.
c   The program assumes a gas target with cylindical symmetry, the origin
c being at the exact center of a two-sided exit hole.  Gas flows between
c two identical thin plates separated by a small distance.  The hole goes
c through both plates and is where the gas exits the system.  Particles are
c tracked from a specified distance back from the hole center between
c the plates.  Each particle is tracked until it either exits the hole
c or else goes back between the plates past where it started.  The
c program reports the ratio of the number of hole exits to the number
c of trials.  This allows the flow rate of the target to be calculated.
c It is assumed that the density of gas is known at the position where
c the particles appear.  The files which are created show the density
c of the gas throughout the target as a fraction of the initial density.
c One file shows the density as a function of radius, from the hole
c center to the the initial position between the plates.  The other file
c shows the density in the hole as a function of z.  This is done for
c 5 radii within the hole.  The radii are equally spaced from the
c center to the hole edge.  A third file is made which specifies all
c of the parameters for the given program run.  Another file is created
c which gives the average value of the density as a function of z.
c The files are respectively: rfile, zfile, nfile, afile.
c
      IMPLICIT NONE
      REAL x,y,z,xo,yo,zo,mx,my,mxo,myo,bx,by,phi,alpha,beta,ta,
     +  a,c,d,r,L,lambdap,lambdah,spec,e,f,g,h,tasb,sp,cp,cb,rper,
     +  zper,zmin,zmax,zmaxo,zplus,zminus,zclose,zc,zf,rc,rf,len,
     +  leno,den1(1:5,1:150),den2(1:500),zdir,zdiro,u,p,zt,norm,
     +  ran,acos,asin,d1,d2,d3,d4,d5,probp,probh
      INTEGER cyl,exit,i,io,j,iL,num,k,kmin,kmax,q,qmin,qmax,zdim
      DOUBLE PRECISION count
      DATA zdim /150/, den1 /750*0./, den2 /500*0./
      j=-1
      WRITE (*,*) 'Enter plate thickness (c).'
      READ (*,*) c
      WRITE (*,*) 'Enter plate separation (a > c/25).'
```

```
        READ (*,*) a
        zper = (c + a/2.)/(zdim/6.)
        WRITE (*,*) 'Enter hole diameter (d).'
        READ (*,*) d
        r = d / 2.
        rper = r/5.
        WRITE (*,*) 'Enter length from center where density is known (L).'
        WRITE (*,*) 'It will be truncated to the nearest 10th of hole diameter.'
        READ (*,*) L
        iL = L/rper
        L = iL * rper
        WRITE (*,*) 'Enter mean free path of particle (between plates only).'
        READ (*,*) lambdap
        WRITE (*,*) 'Enter the ratio of probabilities between scattering'
        WRITE (*,*) 'uniformly over a hemisphere directed toward the exit'
        WRITE (*,*) 'and away from the exit (between plates only).'
        READ (*,*) probp
        probp = probp/(1. + probp)
        WRITE (*,*) 'Enter mean free path of particle (inside of hole only).'
        READ (*,*) lambdah
        WRITE (*,*) 'Enter the ratio of probabilities between scattering'
        WRITE (*,*) 'uniformly over a hemisphere directed toward the exit'
        WRITE (*,*) 'and away from the exit (inside of hole only).'
        READ (*,*) probh
        probh = probh/(1. + probh)
        WRITE (*,*) 'Enter the probability that a reflection will be specular.'
        READ (*,*) spec
        WRITE (*,*) 'Enter required number of successful particles.'
        READ (*,*) num
c
        i = 0
        count = 0.d0
c
c       Main program loop begins here.  The loop will continue until
c       the specified number of particles successfully leaves the hole.
        DO WHILE (i .lt. num)
c
          count = count + 1.d0
c
c         Initial condition for a new particle.
          z = RAN(j) * a/2
          phi = 2 * 3.14159 *RAN(j)
          x = L * COS(phi)
          y = L * SIN(phi)
100       alpha = ACOS(RAN(j))
          beta = 2 * 3.14159 * RAN(j)
          ta = TAN(alpha)
          tasb = ta*SIN(beta)
c         Protection against division by zero.
          IF (ABS(tasb) .lt. .001) GOTO 100
          cb = COS(beta)
          sp = SIN(phi)
          cp = COS(phi)
          mx = (sp * ta * cb - cp) / tasb
          my = -(cp * ta * cb + sp) / tasb
c
c         zdir indicates whether the particle path is in the direction of
c         increasing or decreasing z.
          IF (beta .lt. 3.14159) THEN
            zdir = 1
          ELSE
            zdir = -1
          END IF
```

```
c        cyl=0 means that the particle is not yet in the cylindrical hole.
         cyl = 0
c
c        Propagation of a particle through the nozzle until it exits.
         exit = 0
         DO WHILE (exit .eq. 0)
c
c  *****   Begining of the single step propogation of the particle.  *****
c
c          Set the z-intercepts and slopes to what was figured
c          the last time through the loop.
           bx = x - mx * z
           by = y - my * z
           zo = z
           mxo = mx
           myo = my
           zdiro = zdir
c          e and h are computed for later use.  They're used to
c          calculate an intersection of the line with the
c          cylindrical hole's wall.
           e = mx**2 + my**2
           IF (e .lt. .0001) THEN
c            Protect against division by zero later.
             e=.0001
           ENDIF
           f = mx * bx + my * by
           g = bx**2 + by**2 - r**2
           h = ABS(f**2 - e * g)
c
c
c          Propagation of a single straight-line step of the particle
c          and calculation of new slope for next step.
c
           IF (cyl .eq. 1) THEN
c            Path beginning inside cylinder if cyl=1.
c            Calculate the intersection of the line with the hole wall.
             z = (-f + zdiro*SQRT(h)) / e
c
             IF (z .lt. 0.) THEN
c              Makes a mirror reflection off of plane z=0.  Because of
c              symmetry with the z-plane, the particles need only
c              propagate in 1/2 of the nozzle to give the result.
c              Give the new position and slopes.
               z = 0.
               mx = -mxo
               my = -myo
c              The particle is headed upward.
               zdir = 1.
             ELSE
c              Hits on inside wall of cylindrical hole.
               x = mxo * z + bx
               y = myo * z + by
c              Protect against division by zero.
               IF (ABS(x) .lt. r/10000.) THEN
                 x = r/10000.
               END IF
c              Calculate azimuthal position.
               phi = ATAN(y / x)
               IF (x .lt. 0.) THEN
                 phi = phi + 3.14159
               END IF
```

```
c
                IF (RAN(j) .gt. spec) THEN
c                 Makes a diffusive reflection.
c                 Calculate new slopes and z-direction of particle.
101               alpha = ASIN(RAN(j))
                  beta = 2. * 3.14159 * RAN(j)
                  ta = TAN(alpha)
                  tasb = ta*SIN(beta)
                  IF (ABS(tasb) .lt. .001) GOTO 101
                  cb = COS(beta)
                  sp = SIN(phi)
                  cp = COS(phi)
                  mx = (sp * ta * cb - cp) / tasb
                  my = -(cp * ta * cb + sp) / tasb
                  IF (beta .lt. 3.14159) THEN
                    zdir = 1.
                  ELSE
                    zdir = -1.
                  END IF
                ELSE
c                 Makes a specular reflection.
c                 Calculate new slopes.  z-direction stays the same.
                  mx = (2*(SIN(phi))**2 - 1)*mxo - SIN(2*phi)*myo
                  my = -(2*(SIN(phi))**2 - 1)*myo - SIN(2*phi)*mxo
                END IF
              END IF
c
c             Figure out if a collision has taken place before the
c             particle hit the wall.
102           u = RAN(j)
c             Protect against division by zero.
              IF (u .lt. .0001) GOTO 102
              u = lambdah*LOG(1/u)
              p = mxo**2 + myo**2 + 1.
              IF (z .gt. a/2. + c) THEN
c               Don't consider positions outside of the hole.
                zt = a/2. + c
              ELSE
                zt = z
              END IF
              IF (p * (zt - zo)**2 .gt. u**2) THEN
c               Collision has occured inside hole before reaching new point.
c               Find the new slopes and positions at the point of collision.
                z = zo + zdiro*u/SQRT(p)
                alpha = ACOS(RAN(j))
                beta = 2 * 3.14159 * RAN(j)
                ta = TAN(alpha)
                mx = ta * COS(beta)
                my = ta * SIN(beta)
                IF (RAN(j) .lt. probh) THEN
c                 This comparison decides whether the particle should
c                 be distributed in the hemisphere pointed toward the
c                 exit hole or away from it.
                  zdir = 1.
                ELSE
                  zdir = -1.
                END IF
              ELSE IF ((z .gt. 0.) .and. (z .lt. a/2.)) THEN
c               Goes back between plates so set cyl=0.
                cyl = 0
c               Continues with original slopes.
                zdir = zdiro
                mx = mxo
                my = myo
              END IF
c
c
```

```
              ELSE
c               Path begins between plates if cyl=0.
c
                IF (zdiro .gt. 0.) THEN
c                 The particle is traveling upward so it hits the plate.
                  z = a / 2.
c                 Next it will be traveling downward.
                  zdir = -1.
                  IF (RAN(j) .gt. spec) THEN
c                   The particle makes a diffusive reflection.
c                   Find the new slopes.
                    alpha = ASIN(RAN(j))
                    beta = 2. * 3.14159 * RAN(j)
                    ta = TAN(alpha)
                    mx = ta * COS(beta)
                    my = ta * SIN(beta)
                  ELSE
c                   The particle makes a specular reflection.
c                   Find the new slopes.
                    mx = -mxo
                    my = -myo
                  END IF
                ELSE
c                 Makes a mirror reflection off of plane z=0.  Because of
c                 symmetry with the z-plane, the particles need only
c                 propagate in 1/2 of the nozzle to give the result.
c                 Find the new slopes and position.
                  z = 0.
                  mx = -mxo
                  my = -myo
c                 Now the particle will be going upward.
                  zdir = 1.
                END IF
c
103             u = RAN(j)
c               Protect against division by zero.
                IF (u .lt. .0001) GOTO 103
                u = lambdap*LOG(1/u)
                p = mxo**2 + myo**2 + 1.
                IF (p * (z - zo)**2 .gt. u**2) THEN
c                 Collision has occured before reaching new point.
c                 Find the new slopes and positions at the point of collision.
                  z = zo + zdiro*u/SQRT(p)
104               alpha = ACOS(RAN(j))
                  beta = 2 * 3.14159 * RAN(j)
                  ta = TAN(alpha)
                  tasb = ta*SIN(beta)
c                 Protection against division by zero.
                  IF (ABS(tasb) .lt. .001) GOTO 104
                  cb = COS(beta)
                  sp = SIN(phi)
                  cp = COS(phi)
                  mx = (sp * ta * cb - cp) / tasb
                  my = -(cp * ta * cb + sp) / tasb
c                 Decide which is the new direction in z for the particle
c                 to move.
                  IF (beta .lt. 3.14159) THEN
                    zdir = 1
                  ELSE
                    zdir = -1
                  END IF
c                 Particle is directed toward the exit hole.
```

```
               IF (RAN(j) .gt. probp) THEN
c                This comparison decides whether the particle should
c                be distributed in the hemisphere pointed toward the
c                exit hole or away from it.
                 zdir = -zdir
c                Particle is directed away from the exit hole.
               END IF
             END IF
c
             IF ((mxo*z+bx)**2 + (myo*z+by)**2 .lt. r**2) THEN
c              Goes into cylinder. Continues with original slopes.
               z = (-f - zdiro* SQRT(h)) / e
c              cyl=1 meanes that the particle has gone into the hole.
               cyl = 1
               zdir = zdiro
               mx = mxo
               my = myo
             END IF
c
           END IF
c
c   *****  End of the single step propogation of the particle.  *****
c
c
c          Exit conditions for particle.
           IF (z .gt. c + a / 2.) THEN
c            Particle has left out the top of the hole.
             IF (z .gt. zdim * zper) THEN
c              It went too far out hole, stop it before its position is out
c              of range for the array den.
               z = zdim * zper
             END IF
c            Exit to get onto tracking the next particle.
             exit = 1
c            Keep track of how many particles go out the hole.
             i = i + 1
           ELSE IF ((mxo*z+bx)**2 + (myo*z+by)**2 .gt. L**2) THEN
c            Particle has gone radially farther from the center than where
c            it started.  Stop it at the starting position x^2+y^2=L^2.
             g = bx**2 + by**2 - L**2
             h = ABS(f**2 - e * g)
             z = (-f + zdiro*SQRT(h))/e
c            Exit to get onto tracking the next particle.
             exit = 1
           END IF
c
           xo=x
           yo=y
c          Figure the curent position of the particle.
           x = mxo*z + bx
           y = myo*z + by
c
c
c
c          From here to the end of the program loop, the path of the
c          particle is appropriately entered into the density array.
c
c          Calculate the path range over z.
c          Consider the entire trajectory.
           IF (zo .lt. z) THEN
c            Trajectory increases in z.
c            Calculate the z-elements for the array den wherein
c            the particle path lies.
```

```
              kmin = zo/zper
              kmax = z/zper
              IF (kmax .lt. z/zper) THEN
                kmax = kmax + 1
              END IF
              zmin=zo
              zmaxo=z
            ELSE
c             Trajectory decreases in z.
c             Calculate the z-elements for the array den wherein
c             the particle path lies.
              kmin = z/zper
              kmax = zo/zper
              IF (kmax .lt. zo/zper) THEN
                kmax = kmax + 1
              END IF
              zmin=z
              zmaxo=zo
            END IF
c
            IF (((x**2 + y**2)/r**2 .gt. 1.01) .or.
     +      ((xo**2 + yo**2)/r**2 .gt. 1.01)) THEN
c             The particle is between the plates.
              IF (zmin .lt. zper) THEN
c               Only be conserned with the part of the trajectory
c               with z<zper.
                IF (zmaxo .gt. zper) THEN
                  zmaxo=zper
                  kmax=1
                END IF
              ELSE
c               Skip down to the end of particle loop since the
c               trajectory does not intersect the density array.
                GOTO 275
              END IF
            END IF
c
c
c           Find the value of z where the line is closest to the z-axis.
            zclose=-f/e
            DO 250, k = kmin+1,kmax
c             zmax and zmin stand for the extreme values of z within
c             the given element k of array den.
              IF (k .eq. kmax) THEN
c               zmaxo<>zper*k since it may be in the middle of an element
c               of array den1.
                zmax=zmaxo
              ELSE
                zmax=zper*k
              END IF
c
c             Calculate the path range over r.
c             Find positions within element k of den which are closest and
c             farthest from z-axis.
              IF (zclose .gt. zmax) THEN
c               The closest point to the z-axis on the line is above zmax
c               so zmax is the closest point to the z-axis within element k
c               of array den.  zmin is the furthest.
                zc = zmax
                zf = zmin
              ELSE IF (zclose .lt. zmin) THEN
c               The closest point to the z-axis on the line is below zmin
c               so zmin is the closest point to the z-axis within element k
c               of array den.  zmax is the furthest.
```

```
                zc = zmin
                zf = zmax
              ELSE
c               The closest point to the z-axis on the line falls within
c               within element k of array den.
                zc = zclose
                IF (zmax-zc .gt. zc-zmin) THEN
                  zf = zmax
                ELSE
                  zf = zmin
                END IF
              END IF
c
c             Calculate the furthest and closest radii contained within
c             the z-element k of array den.
              rf = SQRT((mxo*zf + bx)**2 + (myo*zf + by)**2)
              rc = SQRT((mxo*zc + bx)**2 + (myo*zc + by)**2)
c             Figure the maximum and minimum r-elements q wherein the
c             line passes.
              qmax = rf/rper
              IF (qmax .lt. rf/rper) THEN
                qmax = qmax + 1
              END IF
              qmin = rc/rper
c
c             Increment the density according to where the particle passed.
              leno = 0.
              DO 200, q = qmin + 1, qmax
c               Calculate difference of lengths inside 2 consecutive radii.
                g = bx**2 +by**2 - (rper*q)**2
                h = ABS(f**2 - e*g)
c               zplus and zminus are the two intersections of the line
c               with the radius rper*q.
                zplus = (-f + SQRT(h))/e
                IF (zplus .gt. zmax) THEN
c                 Chop off anything outside of z-element k of den.
                  zplus = zmax
                END IF
                zminus = (-f - SQRT(h))/e
                IF (zminus .lt. zmin) THEN
c                 Chop off anything outside of z-element k of den.
                  zminus = zmin
                END IF
                len = SQRT((mxo**2 + myo**2 + 1)*(zplus-zminus)**2)
c               Here the element of array den is incremented by the length
c               of the line segment passing through it.
                IF (q .le. 5) THEN
                  den1(q,k) = den1(q,k) + len - leno
                ELSE
                  den2(q) = den2(q) + len - leno
                ENDIF
                leno=len
200           CONTINUE
c             Prepare to increment the element which has the next value of z.
              zmin = zmax
250         CONTINUE
c
c
275       ENDDO
c         End of the loop for a single particle.
c
```

```
c         Progress report to screen and file every time 100 particles leave.
          IF ((i/1000 .eq. i/1000. .or. i .eq. num) .and. i .ne. io) THEN
            io=i
            WRITE (*,*) i
c
c           Write to the files what has been acomplished so far.
c
c           Normalize the density matrix and divide by the radius.
c           We divide by the radius (actually the difference between
c           the squares of 2 consecutive radii) since there has
c           been no distinction made of the azimuthal angle when
c           elements of array den are incremented.
c
            norm = den2(iL)/(2*iL - 1)
c
c           Write all of the data to files.
            OPEN (20, FILE='zfile', STATUS='unknown')
            OPEN (25, FILE='afile', STATUS='unknown')
            DO 400, k=1,zdim
c             Divide by the normal and the radius.
              d1 = den1(1,k)/norm
              d2 = den1(2,k)/(norm*3)
              d3 = den1(3,k)/(norm*5)
              d4 = den1(4,k)/(norm*7)
              d5 = den1(5,k)/(norm*9)
              z = k*zper
              WRITE (20,300) z, d1, d2, d3, d4, d5
300           FORMAT (6(f8.6,xx))
              WRITE (25,*) z, (d1 + d2 + d3 + d4 + d5)/5.
400         CONTINUE
            CLOSE (20)
            CLOSE (25)
            OPEN (30, FILE='rfile', STATUS='unknown')
            DO 500, q=1,5
              WRITE (30,*) q*rper,den1(q,1)/(norm*(2*q - 1))
500         CONTINUE
            DO 600, q=6,iL
c             Divide by the normal and the radius.
              WRITE (30,*) q*rper,den2(q)/(norm*(2*q - 1))
600         CONTINUE
            CLOSE (30)
            OPEN (50, FILE='nfile', STATUS='unknown')
            WRITE (50,*) 'Plate Thickness (c) = ',c
            WRITE (50,*) 'Plate Spacing (a) = ',a
            WRITE (50,*) 'Hole Diameter (d) = ',d
            WRITE (50,*) 'Distance from Center to Known Density (L) = ',L
            WRITE (50,*) 'MFP (Between Plates) = ',lambdap
            WRITE (50,*) 'Skew Ratio (Between Plates) =',probp/(1.-probp)
            WRITE (50,*) 'MFP (Inside Hole) = ',lambdah
            WRITE (50,*) 'Skew Ratio (Inside Hole) =',probh/(1.-probh)
            WRITE (50,*) 'Probability of Specular Reflection = ',spec
            WRITE (50,*) 'Number of Exiting Particles = ', i
            WRITE (50,*) 'Throughput probability = ', i/count
            WRITE (50,*) 'Enterance Area (2*pi*L*a) = ', 2*3.14159*L*a
            WRITE (50,*)
            WRITE (50,*) 'The time it takes for the backing pressure to'
            WRITE (50,*) 'drop by a factor of 2 is given by,'
            WRITE (50,*)
            WRITE (50,*) '4ln2(Backing Volume)/[(Enterance Area)(mfv)'
            WRITE (50,*) '(Throughput probability)]'
            CLOSE (50)
          ENDIF
```

```
c
c
        ENDDO
c       End of program loop.
c
        STOP
        END
c
        REAL FUNCTION RAN(idum)
c This subroutine is taken from Numerical Recipes sec. 7.1.
c Returns a uniform random deviate between 0.0 and 1.0.  Set
c idum to any negative value to initialize or reinitialize the
c sequence.
        REAL rm
        INTEGER m, ia,ic, j, iff, iy, ir(97)
        PARAMETER (m=714025,ia=1366,ic=150889,rm=1./m)
        DATA iff /0/
        IF (idum.lt.0.or.iff.eq.0) THEN
          iff=1
          idum=MOD(ic-idum,m)
          DO 14, j=1,97
            idum=mod(ia*idum+ic,m)
            ir(j)=idum
14        CONTINUE
          idum=mod(ia*idum+ic,m)
          iy=idum
        ENDIF
        j=1+(97*iy)/m
        IF (j.gt.97.or.j.lt.1) PAUSE
        iy=ir(j)
        ran=iy*rm
        idum=mod(ia*idum+ic,m)
        ir(j)=idum
        RETURN
        END
```

APPENDIX B

HARMONIC EMISSION FROM A FOCUSED LASER CALCULATED FROM A SIMPLE POWER LAW

For low field intensities, the production of the q$^{\underline{th}}$ harmonic depends on the q$^{\underline{th}}$ power of the laser field intensity. As the laser field increases and we enter the plateau regime, the q$^{\underline{th}}$ harmonic is created with an effective dependence on the laser field which is of much lower order. This section investigates the properties of the far-field emission pattern under this scenario. To simplify the problem, the emission of the q$^{\underline{th}}$ harmonic is assumed to follow a power law of order p where p<q. This will provide a general idea of how the emission dependence in the plateau region effects the harmonic far-field profiles. L'Huillier, et al., did calculations based on this model to study the harmonic field strengths inside the interaction region.[1,2] However, they did not calculate the far-field harmonic profiles, which is calculated here.

If the dipole emission for the q$^{\underline{th}}$ harmonic is proportional to the laser field strength to the p$^{\underline{th}}$ power, then Eq. (5.3.8) becomes

$$E_q(\bar{r},t) = \frac{eq^2\omega^2}{4\varepsilon_o c^2 r} e^{ik_q r - iq\omega t} \int \rho' d\rho' dz' N_o(z') x_q\left[E_o^p(t - r/c)\right] f^p(\rho',z') J_o\left(\frac{k_q \rho\rho'}{z}\right)$$
$$\times \exp\left\{-i\Delta k z' + ik_q \rho^2 z'/2z^2 + iq\alpha(\rho',z')\right\} + \mathrm{C.C.} \qquad \text{(B.1)}$$

The atomic distribution $N_o(z')$ is assumed to be independent of radius. The possibility of ionization is not considered, so the integration is free of any temporal dependence. Note that the phase of the dipole for this model is independent of the laser field strength. Substitution of Eq. (5.3.3) into Eq. (B.1) gives the more explicit form

$$E_q(\vec{r},t)=\frac{eq^2\omega^2}{4\varepsilon_o c^2 r}x_q\left[E_o^p(t-r/c)\right]e^{ik_q r-iq\omega t}\int_{z_1}^{z_2}dz'\frac{N_o(z')w_o^p}{w^p(z')}e^{-i\left\{\Delta kz'+q\tan^{-1}\left(\frac{z'}{z_o}\right)-\frac{k_q\rho^2 z'}{2z^2}\right\}}$$
$$\times\int_0^\infty \rho' d\rho' \exp\left\{-\left(\frac{p}{w^2(z')}-iq\frac{k_1 w_o^2}{2z_o^2 w^2(z')}\right)\rho'^2\right\}J_o\left(\frac{k_q\rho\rho'}{z}\right)+\text{C.C.} \qquad \text{(B.2)}$$

The radial integration of Eq. (B.2) can be performed analytically with the formula[1]

$$\int_0^\infty \rho' d\rho' e^{-\alpha\rho'^2}J_o(\beta\rho')=\frac{e^{-\beta^2/4\alpha}}{2\alpha} \qquad (\text{Re}\,\alpha>0). \qquad \text{(B.3)}$$

The result of the integration gives for the second line of Eq. (B.2) the following:

$$\frac{z_o\sqrt{1+z'^2/z_o^2}}{k_1 p}\eta\exp\left\{-\frac{k_q^2 z_o\rho^2\eta^2}{2p^2 k_1 z^2}\left(p+iq\frac{z'}{z_o}\right)+i\tan^{-1}(qz'/pz_o)\right\} \qquad \text{(B.4)}$$

$$\text{where}\quad \eta=\sqrt{\frac{1+(z'/z_o)^2}{1+(qz'/pz_o)^2}}. \qquad \text{(B.5)}$$

Eq. (B.3) is now reduced to a 1-dimensional integral. Before inserting Eqs. (B.4) and (B.5) into Eq. (B.3), it is convenient to make a variable change as defined by

$$u(z')=\tan^{-1}\left(\frac{z'}{z_o}\right) \;\Rightarrow\; du=\frac{w_o^2 dz'}{w^2(z')z_o}. \qquad \text{(B.6)}$$

Then Eq. (B.3) becomes

$$E_q(\theta,t)=\frac{eq^2\omega^2 z_o^2 x_q\left[E_o^p(t-r/c)\right]}{8k_1\varepsilon_o c^2 r}e^{ik_q r-iq\omega t}\int_{u_1}^{u_2}\frac{du}{p}N_o(u)(\cos u)^{p-3}e^{-i\Delta k z_o\tan u-iqu+i\tan^{-1}\left(\frac{q\tan u}{p}\right)}$$

$$\times\eta e^{-\left(q^2/p\right)\eta^2\left(2\theta f^{\#}\right)^2}e^{iq\left(2\theta f^{\#}\right)^2\left[1-q^2\eta^2/p^2\right]\tan u}+\text{C.C.} \qquad \text{(B.7)}$$

where $\eta=1\Big/\sqrt{\cos^2 u+\left(q^2/p^2\right)\sin^2 u}\,.$ (B.8)

The integration of Eq. (B.7) must be performed numerically. The reason for the change from z' to u is that it improves the computational efficiency by making each numeric segment of the integration (change in u) of approximately equal importance to the final answer. ρ/z has been replaced by $\sin\theta\cong\theta$. The values of u_1 and u_2 are respectively $\tan^{-1}(z_1/z_o)$ and $\tan^{-1}(z_2/z_o)$. In the case of p=q (lowest order perturbation), $\eta = 1$ and all terms involving θ in Eq. (B.7) are able to be brought out in front of the integral. The angular dependence of the harmonic has the form $\exp\{-q(2\theta f^{\#})^2\}$. From Eqs. (5.3.1) and (5.3.3), the far-field angular profile of the laser beam has the form $\exp\{-(2\theta f^{\#})^2\}$. Thus, for perturbation theory the $q^{\underline{th}}$ harmonic angular profile is a gaussian which is $\sqrt{q}$ times narrower than the emerging gaussian laser field. A remarkable feature of the perturbative case is that the far-field harmonic profile is independent of the thickness of the gas distribution. The atomic distribution only effects the strength of the harmonic emission, but not the far-field angular distribution.

Of particular interest is the case where p<q since this is the situation for the harmonic plateau. For this general case where p does not necessarily equal q, the far-field angular profile can be understood analytically for a very thin gas target ($\ell=z_2-z_1<<b$) in two limits: the target positioned at the focus (u=0), and the target positioned

far outside the Rayleigh range ($u \sim \pi/2$). In the two limits, η can be approximated as 1 or p/q respectively. In either case, the gaussian term containing θ can be brought out in front of the integral. Its width is $q/\sqrt{p}$ times narrower than the laser profile for the case where the target is positioned at the focus and $\sqrt{p}$ times narrower than the laser profile for the case where the target is positioned far outside the Rayleigh range. For target positions ranging between the two limits, the thin target approximation yields gaussian profiles with widths that lie somewhere between the two limits.

Fig. B.1 shows the square modulus of the integral of Eq. (B.7) for the 25th harmonic generated in a thin target (ℓ=b/10) as a function of target position relative to the focus. b is the confocal parameter which is equal to $2z_0$, and p is taken to be 5. The terms in front of the integral are ignored. The target thickness ℓ=b/10 is approximately the thickness used in the experiments of this thesis. The dashed line is the laser profile ($1/e^2$ radius at $2\theta f^{\#}=1$), the dot-dashed line is a distribution which is $\sqrt{p}$ times narrower than the laser, and the dotted line is a distribution which is $q/\sqrt{p}$ times narrower than the laser. Subsequent graphs will also show these reference lines. As the target position moves away from the focus, the width of the far-field profile varies between the two limits discussed above. The fact that the far-field profiles are very nearly gaussian shows that a target thickness of b/10 is thin enough that the harmonics can be thought of as being generated in a single plane.

The thin gas target approximation holds near the focus (z=0) as long as $\eta \sim 1$, or in other words as long as $(q\ell/pb)^2 << 1$. For the parameters of Fig. B.1 (q=25, p=5, ℓ=b/10), $q\ell/pb$ is equal to 0.5 which marginally satisfies the condition. As either q or ℓ increases, the condition fails and the far-field angular profile is no longer a gaussian. Fig. B.2 shows the far-field patterns for different harmonic orders for a thin target (ℓ=b/10) positioned at the laser focus. p is chosen to be 5. The thin target approximation breaks down as q gets very large. In accordance with the previous estimate, the thin target approximation holds for q=15 but begins to deviate for q=31. The cases for q=63 and q=125 are repeated in Fig. B.2 with a magnified scale so that the non-gaussian structure can be clearly seen. It is important to note that for higher values of q, as the structure becomes more complex, it does not significantly broaden. In other words, a broad far-field pattern does not come about simply because q is very large, but may come about when the harmonics are created in a region away from the focus as seen in Fig. B.1. As the thin target approximation breaks down, the far-field angular profile, though it may become complicated, still obeys the simple rule illustrated in Fig. B.1. That is, when the harmonics are created away form the laser focus, either because the target is thick or positioned off center, the angular profile, whether gaussian or more complicated, is bounded by a gaussian curve that is $\sqrt{p}$ times narrower than the laser profile.

Fig. B.3 shows what happens as a gas target positioned at the laser focus becomes thicker. A broader and more complicated far-field profile is the result . Even so, in the most extreme case the curve is no wider than a gaussian which is $\sqrt{p}$ times narrower than the laser profile. While the complexity of the far-field pattern can be influenced by several parameters, it is again apparent that the overall width is determined almost exclusively by the width (or position) of the gas target relative to the confocal parameter.

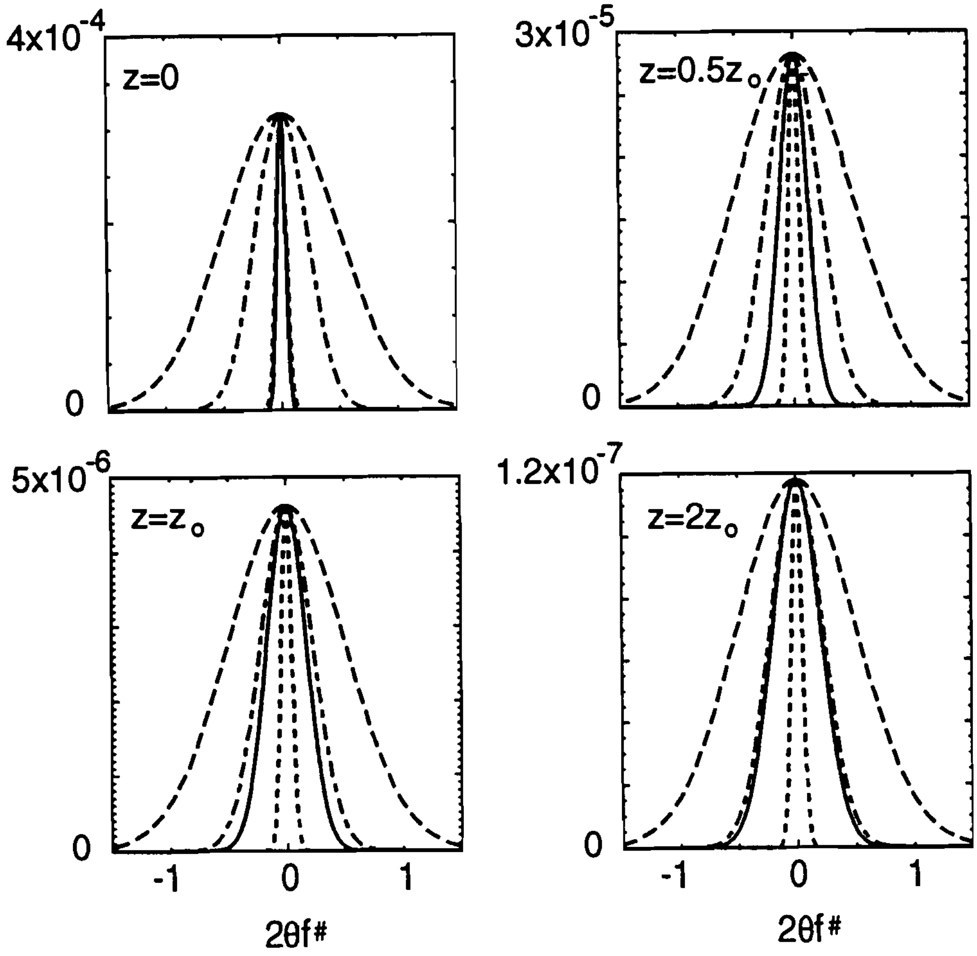

Fig. B.1 The far-field profile (square modulus of the integral in Eq. (B.7)) for a thin target, ℓ=b/10, for several target positions (solid line). The dashed line is the laser profile, the dotted line is the laser profile to the pth power, and the dot-dashed line is the laser profile to the p^2/q power. For all figures, q=25, p=5, and Δk=0.

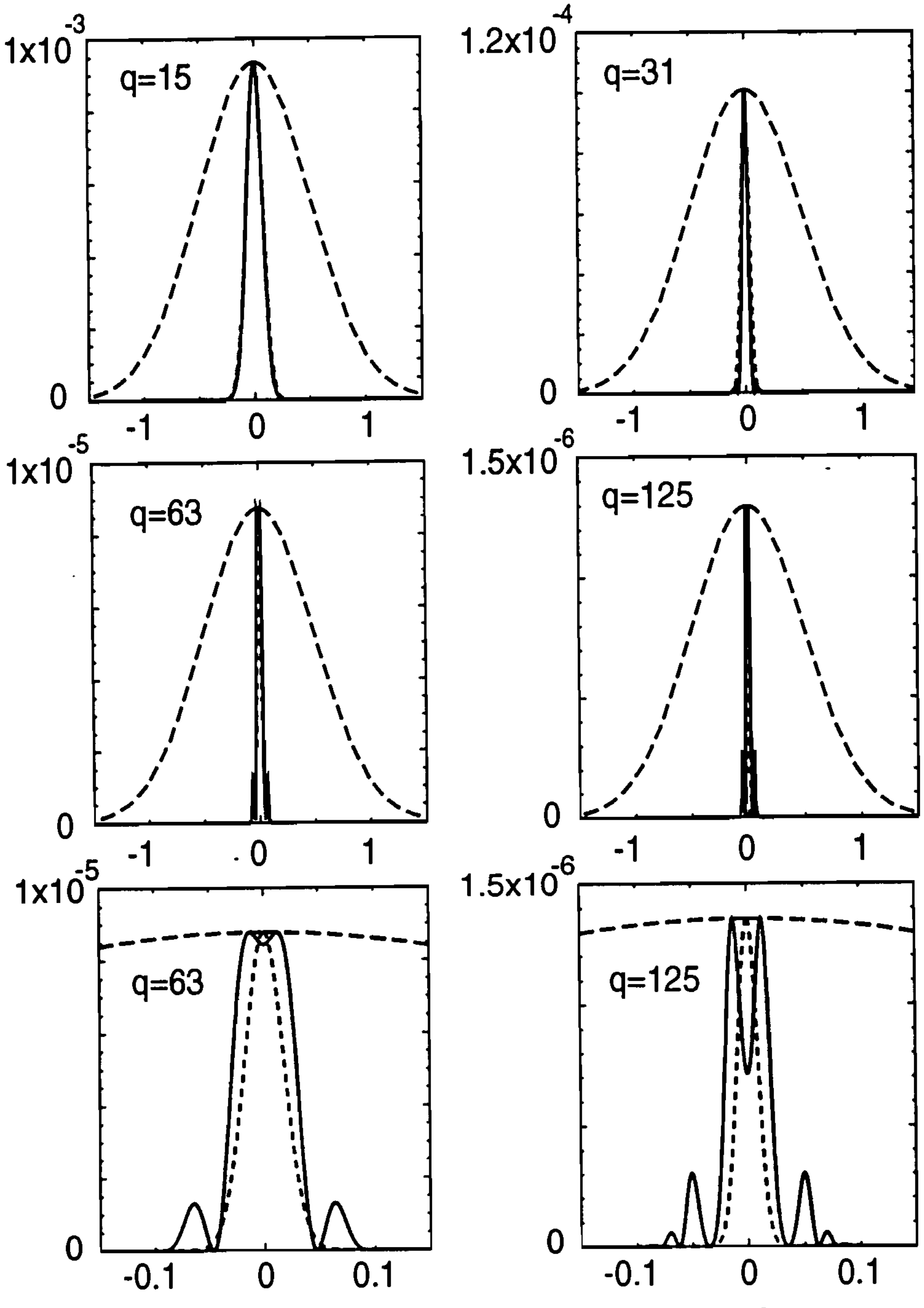

Fig. B.2 The far-field profile (square modulus of the integral in Eq. (B.7)) for a thin target, ℓ=b/10, for several values of q (solid line). The dashed line is the laser profile, the dotted line is the laser profile to the p^2/q power. For all figures p=5 and Δk=0, and the target is positioned at the origin z=0. The cases for q=63 and q=125 are shown twice using different scales so that the structure is more apparent.

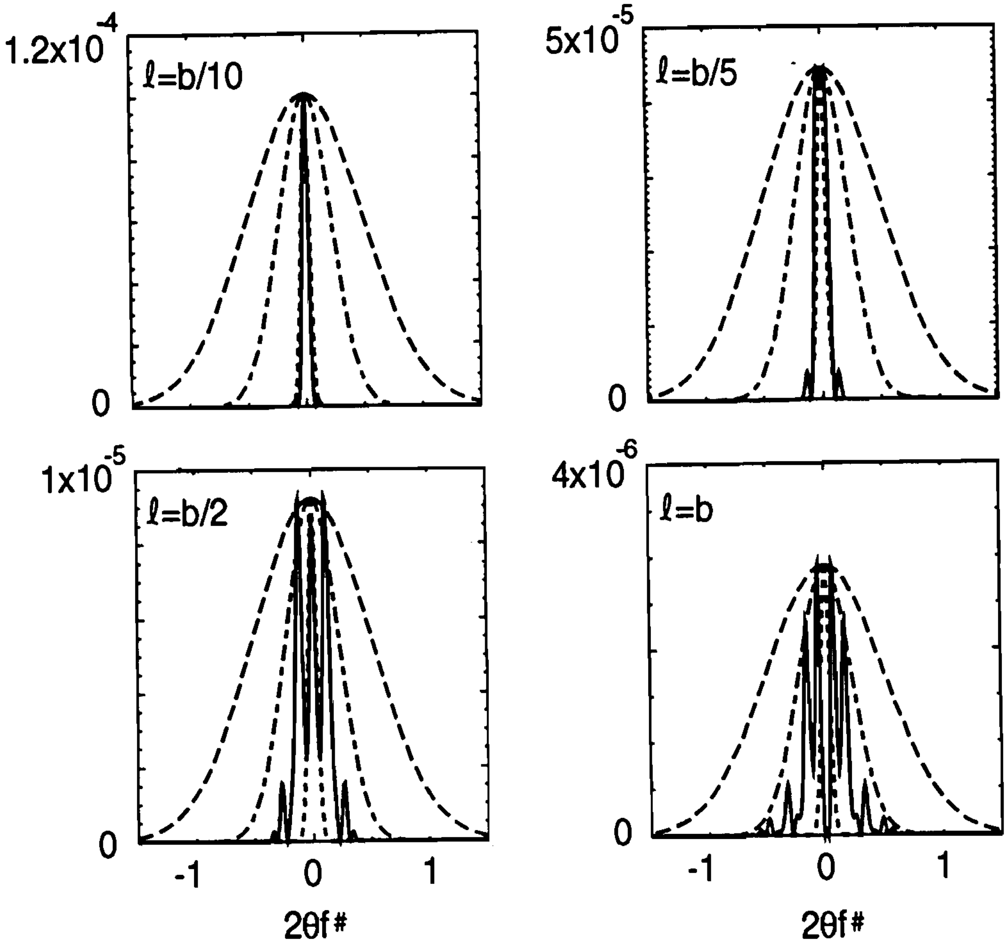

Fig. B.3 The far-field profile (square modulus of the integral in Eq. (B.7)), for several target thicknesses (solid line). The dashed line is the laser profile, the dotted line is the laser profile to the pth power, and the dot-dashed line is the laser profile to the p^2/q power. For all figures q=31, p=5 and $\Delta k=0$, and the target is positioned at the origin z=0.

L'Huillier and co-workers[1,2] were the first to investigate the phase-matching effect of harmonic production by the simple power law studied in this appendix (q^th^ harmonic generated as the p^th^ power of the laser). Their calculations investigated the harmonic fields in the region of the laser focus. They did not investigate the far-field profiles. They demonstrated how rather complicated and broad structures can be induced by this model inside the interaction region. Fig. B.4 shows their calculations of the electric field distribution within the interaction region for various values of q and p [Ref. 2, Fig. 12]. The broad structure in the focus does not necessarily translate into a broad structure in the far-field pattern. In fact, if the gas target is thin relative to the confocal parameter, the converse is true. However, the experimental setup used by L'Huillier et al. employed a relatively thick gas target, ℓ=b/2. The pictures in Fig. B.4 were generated for this target thickness. Complicated and somewhat broad far-field patterns can result in this case. Fig. B.5 shows the far-field angular profiles calculated for these conditions. Even in this case the structure is narrower than the laser profile.

Fig. B.6 shows the far-field angular profiles calculated for these same parameters except the target thickness is ℓ=b/10, the thickness used for the experiments presented in this thesis. In all cases, the far-field profiles are almost identical to the laser profile raised to the p^2/q power as expected from a thin target. As is evident, the far-field pattern has very narrow structure relative to the laser beam. Thus, this model cannot explain the broad wings observed in the experiments presented in this thesis. The conclusion of this investigation is that the broad wings must come from some other mechanism besides the geometry of this power law.

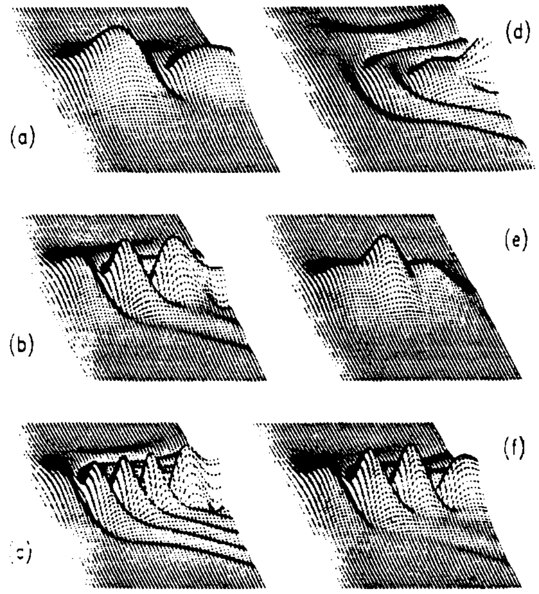

Fig. B.4 The modulus of the harmonic electric field distribution in the laser focus for various values of q and p: (a) q=7, p=5, (b) q=13, p=5, (c) q=21, p=5, (d) q=13, p=2, (e) q=13, p=8, (f) q=13, p=5, $\Delta kz_0 \cong 2$. The dipole medium is centered at the laser focus and has a thickness $\ell \cong b/2$. [reproduced from Ref. 3, Fig. 12]

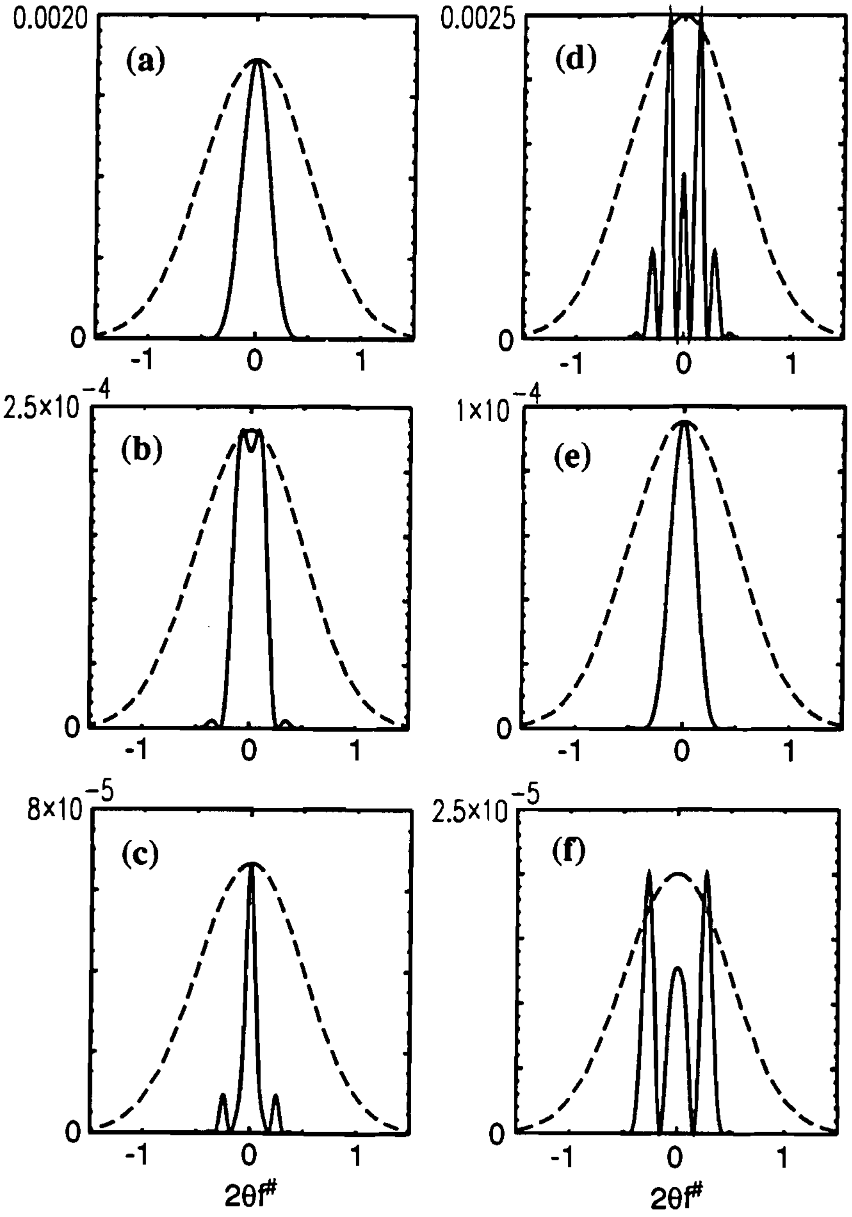

Fig. B.5 The far-field profile (square modulus of the integral in Eq. (B.7)) for the same conditions as used to generate Fig. B.4 (ℓ=b/2). The dashed line is the laser profile.

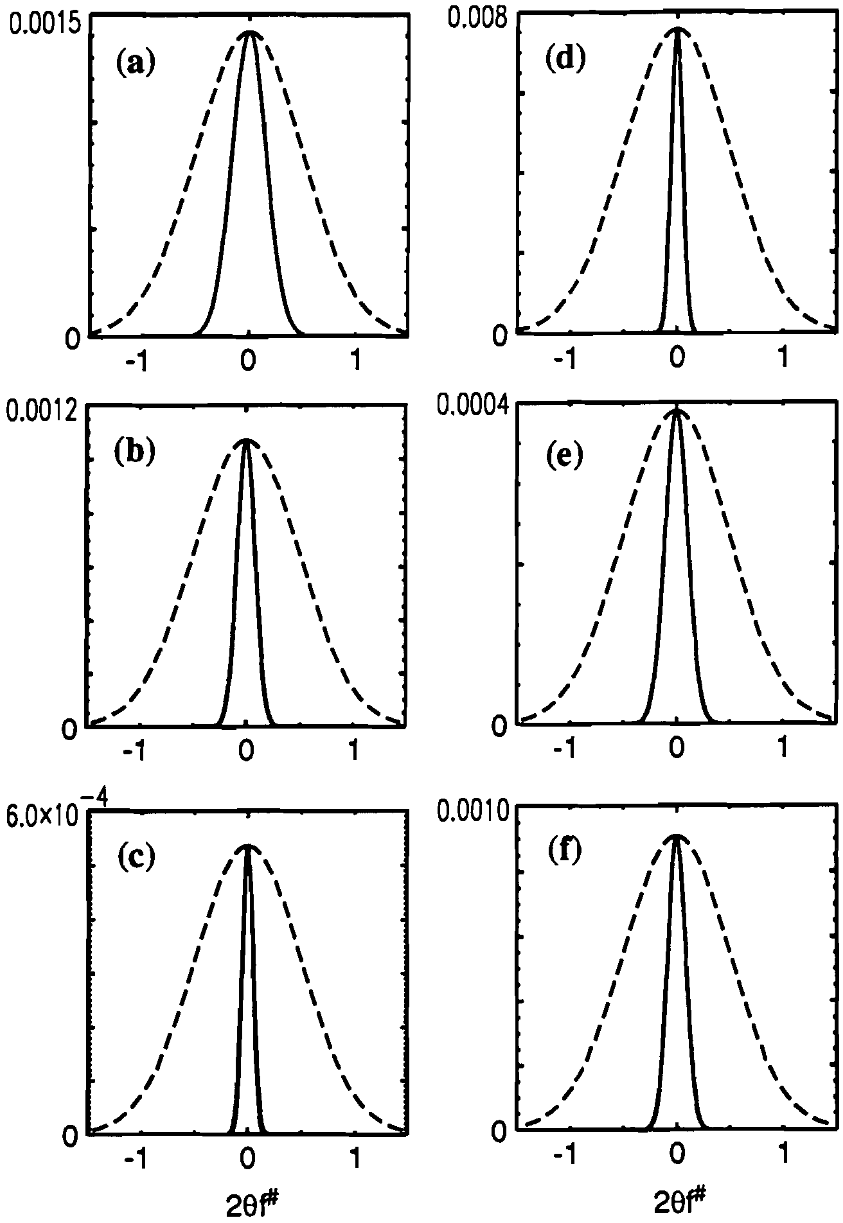

Fig. B.6 The far-field profile (square modulus of the integral in Eq. (B.7)) for the same conditions as were used to generate Fig. B.4 except that the gas distribution is taken as ℓ=b/10, the thickness used for the experiments in this thesis. The dashed line is the laser profile.

REFERENCES

1. A. L'Huillier, Ph. Balcou, and L. A. Lompre, "Coherence and Resonance Effects in High-Order Harmonic Generation," Phys. Rev. Lett. **68**, 166-169 (1992).
2. A. L'Huillier, Ph. Balcou, S. Candel, K. J. Schafer, and K. C. Kulander, "Calculations of High-Order Harmonic-Generation Processes in Xenon at 1064 nm," Phys. Rev. A **46**, 2778-2790 (1992).
3. See I. S. Gradshteyn and I. M. Ryzhik, *Table of Integrals, Series, and Products*, corrected and enlarged edition, prepared by Alan Jeffrey (Academic Press, San Diego, 1980), formula 6.631.4.

APPENDIX C

THE EFFECT OF IONIZATION ON THE HARMONIC FAR-FIELD ANGULAR PATTERN

This appendix shows the details of a model used to explore the effects of ionization on the harmonic far-field profiles. As expected, the results show that for the experimental conditions of this thesis, ionization does not strongly influence the far-field profiles. Calculations based on the formulas derived in this appendix conclusively eliminated the possibility that ionization causes the broad wings observed.

The ionization rate is assumed to follow a simple intensity power law of order n. The probability that at a given time an atom has ionized is

$$P(t) = 1 - \exp\left\{ -\int_{-\infty}^{t} \left(E(t')/E_s\right)^{2n} \frac{dt'}{\tau_s} \right\}, \tag{C.1}$$

where τ_S is chosen to give physical significance to E_S. τ_S is chosen so that

$$\int_{-\infty}^{\infty} \left(E(t')/E_s\right)^{2n} \frac{dt'}{\tau_s} = \left(E_o/E_s\right)^{2n} \tag{C.2}$$

where E_0 is understood to be the peak value of the field in the focus. Thus, E_S is the saturation field strength. That is, when the peak value of the field E_0 equals E_S, the term in the exponent of Eq.(C.1) becomes -1 after the pulse is ended. This marks the point where the exponent can no longer be represented by its two leading expansion terms. When E_0 is below E_S, the exponent can be reasonably represented by its first two expansion terms. When E_0 is less than E_S, then at the end of the pulse $P(\infty) \cong \left(E_o/E_s\right)^{2\beta}$. When E_0 is greater than E_S, then at the end of the pulse $P(\infty) \cong 1$.

Thus, E_S is a field strength value which marks the onset of strong ionization. It is known as the saturation field. E_S depends on the temporal shape and duration of the pulse.

The laser pulse temporal envelope is assumed to be a gaussian, which can be written as

$$E_o(t - r/c) = E_o e^{-\left\{\frac{t-r/c}{\tau}\right\}^2} . \tag{C.3}$$

Recall that $r = \sqrt{z^2 + \rho^2}$. For the gaussian laser pulse defined by Eqs. (5.3.1) and (5.3.3), the probability of ionization at a temporal and spatial point within the beam is

$$P(\rho, z, t) = 1 - \exp\left\{ -\left(\frac{E_o}{E_s}\right)^{2n} \left[\frac{w_o}{w(z)}\right]^{2n} e^{-2n\rho^2/w^2(z)} \frac{1}{\tau}\sqrt{\frac{2n}{\pi}} \int_{-\infty}^{t} e^{-2n\left(\frac{t'-r/c}{\tau}\right)^2} dt' \right\}. \tag{C.4}$$

τ_S has been entered explicitly as $\tau\sqrt{\pi/2n}$. If the transformation defined by Eq. (C.6) is used along with the transformation defined by

$$s(\rho') = \exp\left\{-\frac{\rho'^2}{w^2(z')}\right\} \Rightarrow ds = -\frac{2\rho' d\rho'}{w^2(z')} \exp\left\{-\frac{\rho'^2}{w^2(z')}\right\}, \tag{C.5}$$

then Eq. (C.4) can be written as

$$P(u, s, t) = 1 - \exp\left\{ -\left[\frac{E_o}{E_s}\cos(u)s\right]^{2n} \frac{1}{\sqrt{\pi}} \int_{-\infty}^{\frac{\sqrt{2n}}{\tau}\left(t - \frac{z_o \tan u}{c}\right)} e^{-\xi^2} d\xi \right\} \tag{C.6}$$

Using the transformations defined in Eqs. (C.6) and (C.5) and the model outlined in Appendix B, and assuming the ionization rate described in Eq. (C.6), the phase-matching integral defined by Eqs. (5.3.8) and (5.3.9) becomes

$$\begin{aligned} E_q(\theta,t) = {} & \frac{eq^2\omega^2 z_o^2 x_q\left[E_o^p(t-r/c)\right]}{8k_1\varepsilon_o c^2 r} e^{ik_q r - iq\omega t} \int_{u_1}^{u_2} \frac{du}{p} N_o(u)(\cos u)^{p-4} e^{-iqu+iq(2f^{\#}\theta)^2 \tan u} \\ & \times \int_0^1 ds\, s^{p-1}\, e^{iq\ln(1/s)\tan u} \left[1-P(u,s,t)\right] \exp\left\{-iz_o \int_{u_1}^{u} \frac{du'\Delta k\left[N_o(u')\right]}{\cos^2 u'} P(u',s,t)\right\} \\ & \times J_o\left[\frac{2q(2f^{\#}\theta)}{\cos u}\sqrt{\ln\left(\frac{1}{s}\right)}\right] + \text{C.C.} \end{aligned} \tag{C.7}$$

The integration of Eq. (C.7) must be performed numerically. The reason for the change from (ρ',z') to (u,s) is that it improves the computational efficiency by making each numeric segment of the integration of approximately equal importance to the final answer. An additional reason for this choice of variables lies in the fact that for fixed s, a change in u follows a path which is perpendicular to the laser wavefront. The integral in the exponent on the second line of (C.7) describes the dephasing of a point on the laser wavefront due to its having passed through free electrons. With fixed s rather than fixed ρ', the integration follows the contour of the laser beam.

As the atoms ionize, the number of dipole radiators decreases. The term 1-P on the second line of Eq. (C.7) accounts for this effect. The many other terms in integral of Eq. (C.7) are the various phase-matching components that arise from the interplay between the gaussian laser focus and the model chosen. If terms describing ionization were not present, the integral over s could be performed analytically and Eq. (C.7) would be obtained.

Eq. (C.7) was computed numerically to see how the inclusion of ionization affects the harmonic far-field pattern. Since there is a temporal dependence inside the integral, the far-field pattern will evolve in time. In the experiments, we observe the total energy deposited during the entire pulse as a function of angle. Thus, the profile of interest is that of the time-integrated energy,

$$\mathrm{Energy}(\theta) = \pi c \varepsilon_0 r^2 \int dt \left| E_q(\theta, t) \right|^2 . \tag{C.8}$$

Fig. C.1 shows far-field patterns calculated by (C.8) together with (C.7) for peak fields below and above the saturation field E_S (indicated in terms I_S, the intensity which corresponds to E_S). All of the constants in front of the integrals have been left off. The electron-induced phase mismatch is calculated for the typical experimental pressure of 1 Torr. For the pictures involving the higher intensities, the atoms at the center of the focus are strongly depleted during the pulse pulse. As this occurs, the far-field pattern narrows somewhat, and small wings appear. This effect is due primarily to the diffraction caused from the absence of harmonic generation in the center of the interaction region and not to the phase-mismatch induced by the free electrons.

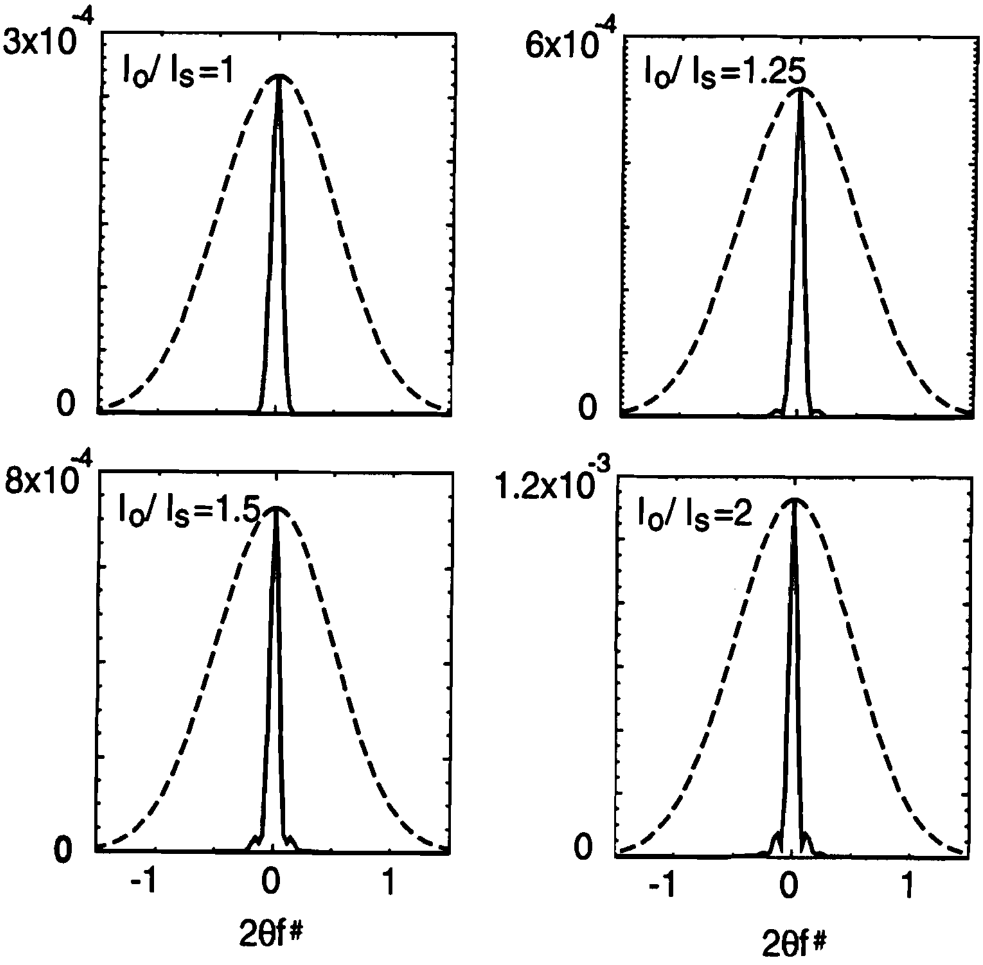

Fig. C.1 The far-field pattern calculated by Eqs. (C.7) and (C.8) for peak laser intensities below and above the ionization saturation intensity I_S. For this calculation, q=25, p=5 and ℓ=b/10. The gas density was taken at 1 Torr. The far-field pattern shows the cumulative energy over time which includes the effects of the evolution of the ionization.

APPENDIX D

ANALYSIS OF AN ANHARMONIC OSCILLATOR

This appendix develops an analytical approximation for the motion a strongly driven anharmonic oscillator. The analysis shows the underlying behavior responsible for the creation of a high-harmonic plateau. The equation which we are interested in solving is the following:

$$\ddot{x} + \Gamma\dot{x} + \omega_o^2 x = F\cos\omega_L t - \beta x^3. \tag{D.1}$$

With some manipulation, Eq. (D.1) can be recast into the form,

$$\frac{\ddot{x}'}{\omega_L^2} + \frac{\Gamma}{\omega_L^2}\dot{x}' + \frac{\omega_o^2}{\omega_L^2}x' = f\left(e^{i\omega_L t} + e^{-i\omega_L t}\right) - \frac{x'^3}{3} \tag{D.2}$$

where

$$x' = \frac{\sqrt{3\beta}}{\omega_L}x \quad \text{and} \quad f = \frac{\sqrt{3\beta}}{2\omega_L^3}F \tag{D.3}$$

A harmonic expansion can be introduced under the assumption that only harmonics of the driving frequency are important to the oscillator motion.

$$x' = \sum_{-\infty}^{\infty} a_q e^{iq\omega_L t} \tag{D.4}$$

This expansion can be inserted into Eq. (D.3) to give

$$\sum_{-\infty}^{\infty} a_q e^{iq\omega_L t}\left(\frac{\omega_o^2}{\omega_L^2} + iq\frac{\Gamma}{\omega_L} - q^2\right) = f\left(e^{i\omega_L t} + e^{-i\omega_L t}\right) \pm \frac{1}{3}\left[\sum_{-\infty}^{\infty} a_q e^{iq\omega_L t}\right]^3. \qquad \text{(D.5)}$$

The complex conjugate of Eq. (D.5) yields precisely the same equation in $a*_{-q}$. Therefore,

$$a_{-q} = a*_q \qquad \text{(D.6)}$$

Eq. (D.4), when combined with with Eq. (D.6), reveals that x' can be written as

$$x' = \sum_{q=0}^{\infty} 2\left|a_q\right| \cos\left(q\omega_L t + \nu_q\right). \qquad \text{(D.7)}$$

When Eq. (D.7) is combined with Eq. (D.3), the oscillator motion is seen to be

$$x = \sum_q x_q \cos\left(q\omega_L t + \nu_q\right), \text{ where } x_q = 2\frac{\sqrt{3\beta}}{\omega_L}\left|a_q\right|. \qquad \text{(D.8)}$$

The difficulty in solving Eq. (D.5) lies in the last term. If it were missing, the equation would reduce to the simple harmonic oscillator which could be trivially solved. Some progress can be made by rearranging the last term of Eq. (D.5) in the following manner.

$$\left[\sum_{-\infty}^{\infty} a_q e^{iq\omega_L t}\right]^3 = \sum_{r=-\infty}^{\infty} \sum_{p=r}^{\infty} \sum_{s=p}^{\infty} a_r a_p a_s \left[6 - 3\left(\delta_{r,p} + \delta_{p,s} + \delta_{r,s}\right) + 4\delta_{r,p,s}\right] e^{i(r+p+s)\omega_L t}$$

(D.9)

Eq. (D.9) shows that frequencies of orders r,p,s mix together to create a new frequency of order r+p+s. If r,p,s are all odd numbers, then their sum is also odd. Since the fundamental frequency is referenced by the odd integer 1, it is seen that all harmonics will be of odd order for this model.

Further manipulation to Eq. (D.9) can be made by setting s=q-r-p and then summing over q. This allows Eq. (D.9) to be put into the form

$$\left[\sum_{-\infty}^{\infty} a_q e^{iq\omega_L t}\right]^3 = \sum_{q=-\infty}^{\infty} c_q e^{iq\omega_L t} \tag{D.10}$$

where

$$c_q = \lim_{q_m \to \infty} \sum_{r=-q_m}^{\frac{q}{3}} \sum_{p=\mathrm{Max}\{r,q-r-q_m\}}^{\frac{q-r}{2}} a_r a_p a_{q-r-p}\left[6 - 3\left(\delta_{r,p} + \delta_{2p,q-r} + \delta_{2r,q-p}\right) + 4\delta_{r,p,q-r-p}\right]. \tag{D.11}$$

A substitution of Eq. (D.10) into Eq. (D.5) yields

$$a_1\left(\frac{\omega_o^2}{\omega_L^2} + i\frac{\Gamma}{\omega_L} - 1\right) = f \pm \frac{c_1}{3}, \quad a_q\left(\frac{\omega_o^2}{\omega_L^2} + iq\frac{\Gamma}{\omega_L} - q^2\right) = \pm\frac{c_q}{3} \quad \left(|q| \neq 1\right). \tag{D.12}$$

The complicated mixture of all a_q's in the c_q terms makes Eq. (D.12) impossible to solve. To proceed further it is necessary to make approximations.

Significant progress can be made under the assumption that the fundamental frequency term a_1 is much larger than any other. That is, the most important contributions to each harmonic term c_q involve the strongest available mixings with a_1. This is a kind of perturbative assumption similar to treatments given in many nonlinear optics texts.[1-3] However, this treatment is more general because it allows higher harmonics to influence lower-order ones. As will be seen, this leads to the creation of a harmonic plateau. The c_q of Eq. (D.11) under our assumption simplify to

$$c_1 = 3a_1|a_1|^2 + 3a_3 a^*{}_1^2 \ , \quad c_3 = a_1^3 + 6a_3|a_1|^2 + 3a_5 a^*{}_1^2 \ ,$$
$$c_{q>3} = 3a_{q-2}a_1^2 + 6a_q|a_1|^2 + 3a_{q+2}a^*{}_1^2. \tag{D.13}$$

Eq. (D.6) was employed to arrive at Eq. (D.13). With the approximations of Eq. (D.13), Eq. (D.12) in the cases of q=1 and q=3 can be written as

$$a_1 = \frac{f - \kappa a_1^2 a_3}{\omega_o^2/\omega_L^2 + |a_1|^2 - 1 + i\Gamma/\omega_L} \quad \text{and} \quad a_3 = -a_1^2 \frac{a_1/3 + \kappa a_5}{\omega_o^2/\omega_L^2 + 2|a_1|^2 - 3^2 + i3\Gamma/\omega_L}, \tag{D.14}$$

where $\kappa = a^*{}_1^2/a_1^2$. For q>3 the relationship is

$$a_q = -L_q\left(a_{q-2} + \kappa a_{q+2}\right) \tag{D.15}$$

where

$$L_q = \frac{a_1^2}{\omega_o^2/\omega_L^2 + 2|a_1|^2 - q^2 + iq\Gamma/\omega_L}. \tag{D.16}$$

If for some high q, a_q tends to zero, then Eq. (D.15) yields the relationship

$$a_q = -S_q a_{q-2} \tag{D.17}$$

where S_q is obtained from the recursion formula

$$S_{q-2} = \frac{L_{q-2}}{1 - \kappa L_{q-2} S_q}. \tag{D.18}$$

Eq. (D.18) is initialized with $S_{q\to\infty} = 0$. In the case of a resonance at q-2 ($L_{q-2} = \infty$), Eq. (D.18) shows that $S_{q-2} = -1/S_q$.

To find the solution to Eqs. (D.14)-(D.18), a_1 must first be found. For a given f, this is difficult to do. A much better approach is to choose a_1 and then find what f corresponds to it. Thus, it is convenient to rewrite the relationship for a_1 in Eq. (D.14) to read

$$f = a_1\left(\omega_o^2/\omega_L^2 + |a_1|^2 - 1 + i\Gamma/\omega_L\right) + \kappa a_1^2 a_3 \tag{D.19}$$

where the phase of a_1 is chosen to make f real and positive.

In general Eq. (D.19) gives a complex value for f except for specific choices of a_1. However, we are interested in solutions where f is real and positive. This does not present a problem because symmetry requires that the relative phase between f and a_1 be fixed for a given field strength. Thus, after solving Eqs. (D.14)-(D.19) for a given a_1 with arbitrary phase, the equations can be solved a second time for a_1 multiplied by $|f|/f$, and the solution where f is real is obtained. Solving the equations the second time is unnecessary because the new solution is related to the old one in the following simple matter:

$$a_q \to a_q\left(|f|/f\right)^q. \tag{D.20}$$

This can be seen from Eqs. (D.14)-(D.16). For example, from the first relationship in Eq. (D.14), a shift in the phase of a_1 and f requires 3 times the shift in the phase of a_3.

In summary, the solution procedure is the following: First a_1 is chosen, and Eqs. (D.16) and (D.18) are used to find all S_q from some very high q where $S_q \cong 0$ down to and including S_3. Then $a_3=S_3a_1/3$, and all $a_{q>3}$ are found from Eq. (D.17). Eq. (D.19) is used to find f, and all a_q are adjusted using Eq. (D.20). f is then replaced by $|f|$. Fig. D.1 (a) shows $|a_q|$ plotted for several q as a function of f. For this plot, $\omega_o/\omega_L=10$, and $\Gamma/\omega_L=0.01$. As the field strength increases, the development of a plateau is evident. Fig. D.1 (b) shows $\mathrm{Re}(a_q)$ plotted over the same range on a linear scale. In the range of the plateau, the harmonic oscillation phases vary strongly with the driving field strength. It should be pointed out that when $\Gamma=0$, a_q is real and the phase variation manifests itself as a sign change.

In the low-intensity limit, the coupled set of equations (D.14)-(D.17) reduces to lowest-order perturbation theory. If the conditions $a_1>>a_3$ and $a_{q-4}>>a_q$ $(q\geq5)$ are met, then the set of equations can be written as

$$a_1=\frac{f}{\omega_o^2/\omega_L^2-1+i\Gamma/\omega_L},\ a_3=\frac{-a_1^3/3}{\omega_o^2/\omega_L^2-3^2+i3\Gamma/\omega_L},\ a_{q>3}=\frac{-a_1^2a_{q-2}}{\omega_o^2/\omega_L^2-q^2+iq\Gamma/\omega_L} \tag{D.21}$$

The equations can be successively solved beginning with the first. As an example, a_3 from Eq. (D.21) is found to be

$$a_3=-\frac{f^3}{3\left(\omega_o^2/\omega_L^2-1+i\Gamma/\omega_L\right)^3\left(\omega_o^2/\omega_L^2-3^2+i3\Gamma/\omega_L\right)}. \tag{D.22}$$

It is readily seen that $a_q \propto f^q$ which is the familiar perturbative power law. This behavior can be seen at low field strengths in Fig. D.1 (a).

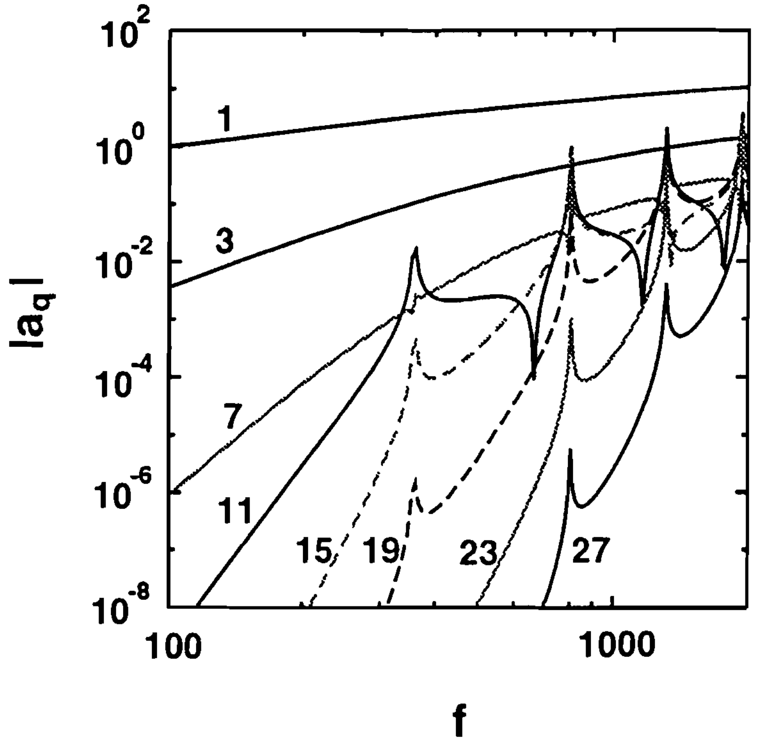

Fig. D.1 (a) The absolute value of the harmonic components of motion for an anharmonic oscillator as a function of the driving field [see Eqs. (D.1), (D.3), and (D.8)]. For this log-log plot, $\omega_0/\omega_L=10$, and $\Gamma/\omega_L=0.01$.

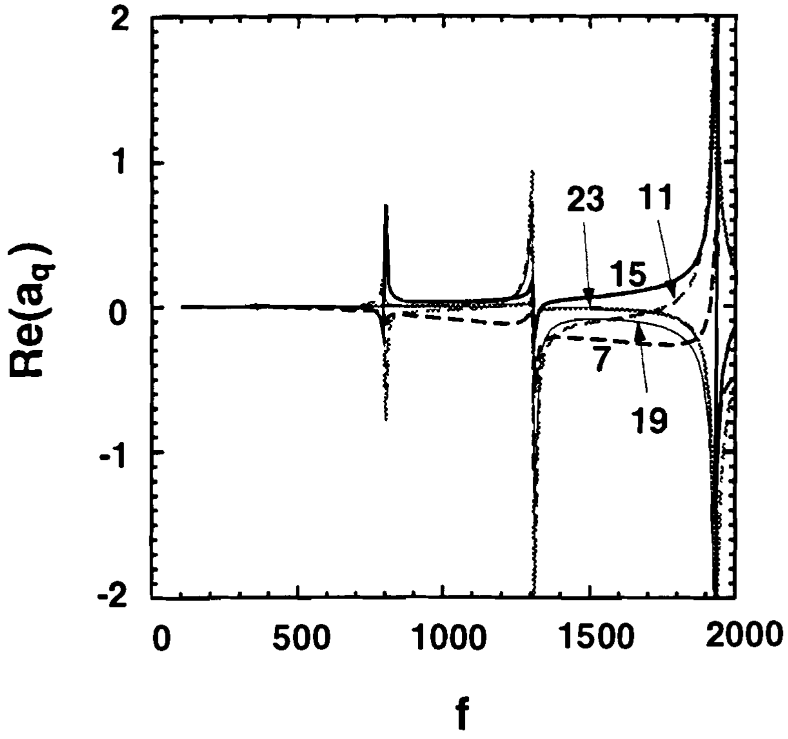

Fig. D.1 (b) The real part of the harmonic component plotted on a linear scale (same conditions as in Fig. D.1 (a)).

REFERENCES

1. R. W. Boyd, *Nonlinear Optics* (Academic Press., San Diego, 1992).
2. P. W. Milonni and J. H. Eberly, *Lasers* (Wiley, New York, 1988).
3. N. Bloembergen, *Nonlinear Optics*, 2nd ed. (Benjamin, Reading, Massachusetts, 1977).
4. L. Plaja and L. Roso-Franco, "Adiabatic Theory for High-Order Harmonic Generation in a Two-Level Atom," J. Opt. Soc. Am. B **9**, 2210-2213 (1992).